Advanced direct detection systems for data center communications

Xueyang Li

Department of Electrical & Computer Engineering

McGill University

Montréal, Canada

August 2021

A thesis submitted to McGill University in partial fulfillment of

the requirements of the degree of Doctor of Philosophy

Abstract

There has been a massive IP traffic growth in the data center network in recent years driven by applications such as artificial intelligence and high-definition video streaming. To accommodate the increasing bandwidth demand, the data rates of pluggable optical modules evolve accordingly while meeting the cost and power constraints because of the use of compact form factors such as QSFP-DD. The available detection schemes for such pluggable modules are divided into two kinds, i.e. direct detection (DD) and coherent detection (COHD). The application boundary between these two detection schemes depends on the link distance that needs to be fulfilled. At the 400G throughput node, COHD systems are dominant for longer-reach connections between centralized data centers over metro distances from 40 km to 120 km which requires high-capacity optical interfaces. Note that the greater throughput-distance product of COHD systems comes at the cost of more complex system hardware and higher power consumption compared to DD systems. Thus for shorter-reach connections such as the intra-data center communications below 10 km, DD systems are dominantly deployed because of the cost-effectiveness and low power consumption.

To date, there is an ongoing effort in developing simplified COHD systems with lower power consumption to substitute DD systems at shorter connection distances below 40 km. From another perspective, it is also viable to design advanced DD systems having a greater throughput-distance product by means of combining the performance advantages found in COHD systems with the cost-effectiveness of DD systems to cover an extended communication reach up to 40 km and beyond. This objective is accomplished in the thesis by designing novel digital signal processing techniques and subsystem architectures. More specifically, we show that probabilistic shaping (PS), often used in long-haul COHD systems, is an effective technique to improve the throughput of DD systems below 10 km where the fiber channel impairments are marginal. We propose

suitable distribution matching schemes to implement PS in short-reach DD systems and optimize the input distribution of PS constellations in practical DD systems by means of a neural network-based performance model. Furthermore, in order to achieve a greater throughput-distance product at an extended transmission reach up to 40 km and beyond as required by the data center interconnects, we propose a set of subsystem structures and relevant DSP algorithms to realize phase-diverse DD systems that approach the throughput of COHD systems given the same receiver electrical bandwidth. The advanced DD systems proposed in the thesis bridge the performance gap between DD systems and COHD systems, and hold promises for realizing high-speed optical links applied in the data center network.

Résumé

Il y a eu une rapide augmentation du trafic IP dans le réseau des centres de données, qui est entraînée par des applications émergentes telles que l'intelligence artificielle et la réalité virtuelle. Pour répondre à la demande croissante de bande passante, le débit de données des modules optiques enfichables doit évoluer en conséquence tout en respectant les contraintes de coût et de puissance à cause du facteur de forme compact utilisé. Les schémas de détection disponibles pour de tels modules enfichables sont divisés en deux catégories, i.e. la détection directe (DD) et la détection cohérente (DCOH). Les cas d'utilisation des deux schémas de détection dépend de la distance qui doit être atteinte par ces modules optiques. Les systèmes DCOH sont dominants pour la connexion entre les centres de données centralisés sur des distances métropolitaines de 80 km à 120 km nécessitant une interface optique à haut débit. Cependant, les performances supérieures des systèmes DCOH se font au prix d'une structure de système plus complexe et d'une consommation d'énergie plus élevée que les systèmes DD. Ainsi, les systèmes DD sont dominants pour les connexions à des distances beaucoup plus courtes au sein des centres de données en raison de leur rentabilité et de leur efficacité énergétique.

À ce jour, il y a un effort continu pour simplifier les systèmes DCOH afin de construire des systèmes DCOH légers pour remplacer les systèmes DD à des distances de connexion plus courtes en dessous de 40 km. D'un autre point de vue, il est également viable de concevoir des systèmes DD renforcés qui combinent les avantages de performance trouvés dans les systèmes DCOH avec la rentabilité des systèmes DD afin d'obtenir un plus grand produit de distance-débit, permettant ainsi une connectivité plus large jusqu'à40 km. Cet objectif est atteint dans la thèse en concevant de nouvelles techniques de traitement du signal numérique et des architectures de sous-systèmes. Plus précisément, nous montrons que la mise en forme probabiliste (PS), souvent utilisée dans les systèmes DCOH de longue distance, est une technique efficace pour améliorer le débit des systèmes DD en dessous de 10 km où les dégradations du canal fibre sont marginales. Nous proposons des approches appropriées pour mettre en œuvre le PS dans des systèmes DD à courte portée et optimiser la distribution des constellations PS dans des systèmes DD pratiques. De plus, afin d'obtenir un produit débit-distance plus élevé à une portée de transmission étendue jusqu'à 40 km et au-delà, comme l'exigent les interconnexions du centre de données, nous proposons plusieurs structures de sous-systèmes et les algorithmes DSP correspondants pour réaliser des systèmes DD à phases diverses qui approchent le débit des systèmes DCOH sur la même bande passante électrique du récepteur. Les systèmes DD avancés proposés dans la thèse comblent l'écart de performance entre les systèmes DD et les systèmes DCOH, et sont prometteurs pour la réalisation de liaisons optiques à haut débit appliquées dans le réseau du centre de données.

Acknowledgments

First and foremost, I want to express my sincere gratitude to my supervisor Prof. David Plant for all the help and support he gave me during my Ph.D. study. It is a great privilege to join such an amazing group led by David and get exposed to top-notch photonic research and cutting-edge experimental infrastructure that David has built over the years. I am also deeply grateful for his encouragement and his trust from the start which stimulates the confidence in me to overcome various difficulties in research. His vision of the research roadmap, his leadership in motivating fruitful discussions, and his remarkable humility as an outstanding expert are qualities that I admire and wish to learn. I look forward to joining an in-person meeting again with David after this difficult time.

My thank also goes to Mohamed Osman for taking the time to teach me the experimental skills in the lab which is important as I had no experience in photonic experiments before joining the group. I am also grateful for his patience in clarifying many of my questions both in research and career. I also want to thank Zhenping for the fruitful discussions I had with him at McGill. I am always impressed by his sharp views on a variety of photonic topics during lunchtime. I would also like to thank Md Samiul Alam for his warm-hearted help in the lab which made my experiments much easier. He is down-to-earth and always eager to keep up with the latest advances in research. I wish him success and good luck in his research. I would also like to thank Yun Wang, Meng Xiang, Thang Hoang, Maxime Jacques, Eslam El-Fiky, and many other members of our group for their help and support in this journey.

I also want to acknowledge our Ciena collaborators Maurice O'Sullivan, Mohammad Pasandi, and Qunbi Zhuge. I learn a great deal from their unique views on our research through the lens of industry such as the complexity of transforming ideas demonstrated in the lab into profitable products in the market. I am also very grateful for the valuable suggestions received from Maurice for most of the research conducted at McGill. His meticulousness towards technical details, exceptional intuitions in physics, and skillfulness in performing engineering calculations whenever possible are exemplary and impressive as an industry leader in high-speed modem development.

At last, I want to thank my parents Mei Yin and Xingyi Li. None of the work in the thesis would be possible without their unconditional support at every stage of my study. They gave me the impetus to keeping moving forward and words are pale to express my affection and gratitude.

Xueyang Li

July 2021

Associated publications

The original contributions of the research work in this thesis are recognized by the community through the following 8 papers [1-10] (6 journal and 2 conference papers out of which 1 journal is invited). The contribution of the co-authors is stated for each paper below. In addition, I also published 12 co-authored journal and conference papers [11-22] through collaborations with other professors, researchers, and students, leading to significant contributions to the field of optical communication as well.

Journal Articles Related to the Thesis

1. **Xueyang Li**, Zhenping. Xing, M. E. Mousa Pasandi, Maurice O'Sullivan and David Plant, "Asymmetric self-coherent detection based on Mach-Zehnder interferometers," *submitted* to Journal of Lightwave Technology, (2021).

   I conceived the idea, performed the simulation and experiment, and wrote the paper. The other authors contributed in discussing the idea and editing the manuscript.

2. **Xueyang Li**, Zhenping. Xing, Md Samiul Alam, M. E. Mousa Pasandi, Maurice O'Sullivan and David Plant, " Asymmetric self-coherent detection," accepted by Optics Express, (2021).

   I conceived the idea, performed the simulation and experiment, and wrote the paper. The other authors contributed in discussing the idea and editing the manuscript.

3. **Xueyang Li**, Zhenping. Xing, Md Samiul Alam, Pingchiek Koh, and David Plant, "Cost-minimizing distribution matching supporting net 800 Gbit/s PS-PAM transmission over 2 km using a 4-λ EML TOSA," in Optics Letters, doi: 10.1364/OL.395631 (2020).

   I conceived the idea, performed the simulation and experiment, and wrote the paper. The other authors contributed in discussing the idea and editing the manuscript..

4. **Xueyang Li**, Zhenping. Xing, Md Samiul Alam, M. E. Mousa Pasandi, Maurice O'Sullivan and David Plant, "Demonstration of C-Band Amplifier-Free 100 Gb/s/ Direct-

Detection Links Beyond 40-km SMF Using a High-Power SSB Transmitter," in Journal of Lightwave Technology, doi: 10.1109/JLT.2020.3009142 (2020).

I conceived the idea, performed the simulation and experiment, and wrote the paper. The other authors contributed in discussing the idea and editing the manuscript.

5. **Xueyang Li**, Maurice O'Sullivan, Zhenping Xing, Md Samiul Alam, Thang Hoang, Meng Xiang, Mingyue Zhu, Jinsong Zhang, Eslam Elfiky, David Plant, "Asymmetric direct detection of orthogonal offset carriers assisted polarization multiplexed single-sideband signals", Optics Express 28, 3226-3236 (2020).

   I conceived the idea, performed the simulation and experiment, and wrote the paper. The other authors contributed in discussing the idea and editing the manuscript.

6. **Xueyang Li**, Mingyue Zhu, Zhenping, Xing, Maurice O'Sullivan, David Plant, " Asymmetric direct detection of twin-SSB signals", Optics letters 45, 844-847 (2020).

   I conceived the idea, performed the simulation and experiment, and wrote the paper. The other authors contributed in discussing the idea and editing the manuscript..

Conference Articles Related to the Thesis

7. Md Samiul Alam, **Xueyang Li**, et al, "C-band 4×200 Gbit/s transmission over 40 km of SSMF with an RF delay-assisted WDM-SSB transmitter", in Optical Fiber Communication Conference (OFC) 2021, accepted. (**Corresponding author**).

   I conceived the idea and performed the simulation. The first author and I did the experiment and wrote the paper. The other authors contributed in discussing the idea and editing the manuscript.

8. **Xueyang Li**, Zhenping Xing, Md Samiul Alam, Maxime Jacques, Stephane Lessard, David V. Plant, "NN-based PCS distribution optimization for practical channels", Proc. ECOC 2020, paper We1D-5.

   I conceived the idea, performed the simulation and experiment, and wrote the paper. The other authors contributed in discussing the idea and editing the manuscript.

Journal Articles Not Directly Related to the Thesis

9. Md Samiul Alam, **Xueyang Li**, et al, "Net 220 Gbps/λ IM/DD Transmission in O-band and C-band with silicon photonic Traveling-Wave MZM," in Journal of Lightwave Technology, doi: 10.1109/JLT.2021.3074096. (2021). **(Co-first and Corresponding author) (Invited)**

10. Zhenping Xing, Meng Xiang, Eslam El-Fiky, **Xueyang Li**, Md. Ghulam Saber, Luhua Xu, Ping-Chiek Koh, and David V. Plant, "Experimental Demonstration of 600 Gb/s Net Rate PAM4 Transmissions Over 2 km and 10 km With a 4-λ CWDM TOSA," in Journal of Lightwave Technology 38, 2968-2975 (2020).

11. Zhenping Xing, Meng Xiang, **Xueyang Li**, Eslam El-Fiky, Md Ghulam Saber, Luhua Xu, Ping-Chiek Koh, David Plant, "Wavelength-Interleaved 4D-PAM4-TCM in a 4-λ × 100 Gb/s CWDM System," in IEEE Photonics Technology Letters 32, 755-758 (2020).

12. Maxime Jacques, Zhenping Xing, Alireza Samani, Eslam El-Fiky, **Xueyang Li**, Meng Xiang, Stéphane Lessard, David V Plant, "240 Gbit/s Silicon Photonic Mach-Zehnder Modulator Enabled by Two 2.3-Vpp Drivers," in Journal of Lightwave Technology 38, 2877-2885 (2020).

13. Ahmad Abdo, **Xueyang Li**, Md Samiul Alam, Mahdi Parvizi, Naim Ben-Hamida, Claude D'Amours, David Plant, "Partial Pre-Emphasis for Pluggable 400 G Short-Reach Coherent Systems,". Future Internet 11, 256 (2019).

14. Meng Xiang, Zhenping Xing, **Xueyang Li**, Eslam El-Fiky, Mohamed Morsy-Osman, Qunbi Zhuge, and David V. Plant, "Experimental study of performance enhanced IM/DD transmissions combining 4D Trellis coded modulation with precoding," Optics Express 26, 32522-32531 (2018).

Conference Articles Not Directly Related to the Thesis

15. **Xueyang Li**, Zhenping Xing, Md Samiul Alam, Maxime Jacques, David Plant, "102 Gbaud PAM-4 transmission over 2 km using a pulse shaping filter with asymmetric ISI

and Thomlinson-Harashima Precoding", in Optical Fiber Communication Conference (OFC) 2020, OSA Technical Digest (Optical Society of America, 2020), paper T3I.1.

16. Zhenping Xing, **Xueyang Li**, Mohammad E. Mousa-Pasandi, Maurice O'Sullivan, David V. Plant, "Filter Response Aware Iterative KK Algorithm for VSB Systems", Proc. ECOC 2020, paper Th2D-8.
17. Zhenping Xing, **Xueyang Li**, David Plant, Mohamed Pasandi, Maurice O'Sullivan, "On Computational Complexities of KK Algorithms with Frequency-domain Digital Resampling", in Signal Processing in Photonic Communications 2020, paper SpTu1I.6.
18. Md Samiul Alam, Ahmad Abdo, **Xueyang Li**, Sadok Aouini, Mahdi Parvizi, Naim Ben-Hamida, and David Plant, "Performance and Complexity Analysis of Blind Timing Phase Error Detectors in Pluggable Coherent Receivers" in Signal Processing in Photonic Communications 2020, paper SpTu1I.2.
19. Naim Ben-Hamida, Ahmad Abdo, **Xueyang Li**, Md Samiul Alam, Mahdi Parvizi, Claude D'Amours, David V Plant, "Study on the Compensation of Silicon Photonics-Based Modulators in DCI Applications," 2020 Design, Automation & Test in Europe Conference & Exhibition (DATE), Grenoble, France, 2020, pp. 1157-1162, doi: 10.23919.
20. Maxime Jacques, Zhenping Xing, Alireza Samani, **Xueyang Li**, Eslam El-Fiky, Samiul Alam, Olivier Carpentier, Ping-Chiek Koh, David V Plant, "Net 212.5 Gbit/s Transmission in O-band With a SiP MZM, One Driver and Linear Equalization," in Optical Fiber Communication Conference Postdeadline Papers 2020, (Optical Society of America, 2020), paper Th4A.3.
21. Zhenping Xing, Meng Xiang, Eslam El-Fiky, **Xueyang Li**, Md Ghulam Saber, Luhua Xu, "600G PAM4 transmission using 4-lambda CWDM TOSA based on controlled-ISI pulse shaping and Tomlinson-Harashima precoding", Proc. ECOC 2019, paper Tu3D.1.
22. Maxime Jacques, Zhenping Xing, Alireza Samani, Eslam El-Fiky, **Xueyang Li**, Stephane Lessard, David Plant, "200 Gbit/s net rate transmission over 2km with a silicon photonic segmented MZM", Proc. ECOC 2019, PDP.1.6.

Contents

List of Figures

List of Tables

List of Acronyms

ADC	Analog-to-digital converter
ASCDD	Asymmetric self-coherent direct detection
ASE	Amplified spontaneous emission
ASIC	Application specific integrated circuit
AWG	Arbitrary waveform generator
AWGN	Additive white Gaussian noise
BER	Bit error rate
BRF	Band rejection filter
B2B	Back-to-back
CCDM	Constant composition distribution matching
CD	Chromatic dispersion
CMOS	Complementary metal-oxide semiconductor
CW	Continuous-wave
CWDM	Coarse wavelength division multiplexing
CSPR	Carrier-to-signal power ratio
DAC	Digital-to-analog converter
DCO	Digital coherent
DCI	Data center interconnect
DD	Direct detection
DDMZM	Dual-drive Mach-Zehnder modulator
DFB	Distributed feedback
DP	Dual-polarization
DSB	Double sideband
DSP	Digital signal processing
DWDM	Dense wavelength division multiplexing
EAM	Electro-absorption modulator
ECL	External-cavity laser
EDFA	Erbium doped fiber amplifier
EML	Electro-absorption modulated laser
ESE	Electrical spectral efficiency
ENOB	Effective number of bit
FEC	Forward error correction
FFE	Feedforward equalizer
FFT	Fast Fourier transform
FO	Frequency offset
FPGA	Field-programmable gate array
IFFT	Inverse fast Fourier transform
IM	Intensity modulation

IMDD	Intensity modulation and direction detection
IR	Information rate
ISI	Inter-symbol interference
KK	Kramers-Kronig
LO	Local oscillator
LUT	Look-up table
MIMO	Multiple-input and multiple-output
ML	Maximum-likelihood
MSA	Multi-source agreement
MSE	Mean square error
MZI	Mach-Zehnder interferometer
MZM	Mach-Zehnder modulator
NRZ	Non-return-to-zero
OIF	Optical internetworking forum
OOK	On-off keying
OSA	Optical spectrum analyzer
OSNR	Optical signal-to-noise ratio
PAS	Probabilistic amplitude shaping
PAM	Pulse amplitude modulation
PAPR	Peak-to-average power ratio
PBS	Polarization beam splitter
PC	Polarization controller
PD	Photodetector
PDL	Polarization dependent loss
PDM	Polarization-division multiplexing
PLL	Phase-locked loop
PMD	Polarization mode dispersion
PS	Probabilistic shaping
PSD	Power spectral density
QAM	Quadrature amplitude modulation
QPSK	Quadrature phase shift keying
RF	Radio frequency
RC	Raised cosine
RRC	Root raised cosine
RTO	Real-time oscilloscope
Rx	Receiver
SC	Self-coherent
SE	Spectral efficiency
SFO	Sampling frequency offset
SiP	Silicon photonic
SISO	Single-input and single-output
SMF	Single mode fiber

SNR	Signal-to-noise ratio
SOP	State of polarization
SP	Single polarization
SSB	Single sideband
SSBI	Signal-signal beating interference
SSMF	Standard single mode fiber
SW	Optical switch
TIA	Trans-impedance amplifier
Tx	Transmitter
VOA	Variable optical attenuator
VODL	Variable optical delay line
VSB	Vestigial sideband
WDM	Wavelength-division multiplexing

1 Introduction

1.1. Background

The invention of lasers as coherent optical sources in the 1960s is a milestone on the path to modern optical communications. Expanded from the concept of masers in the field of microwave communications, lasers are equivalents at optical frequencies that produce coherent continuous-wave light beams. The potential of lasers for line-of-sight communications was quickly seen and experimentally validated soon after its invention. However, it was soon realized that LOS communications through the atmosphere are unstable in bad weather and much effort was invested in the search for a suitable guiding medium at optical frequencies for long reach communications. In 1966, Kuen Kao at Standard Telephones and Cables predicted that the loss of clad single-mode fiber (SMF) based on ultrapure glasses can be reduced to as low as 20 dB/km for high capacity and long-reach communications [1]. Kuen's claim was visionary but also daring at his time as the best fiber had around 1000 dB/km of loss. However, it took only four years before Corning engineered a fiber with 17 dB/km loss. The fiber loss has kept decreasing ever since and reached ~0.2 dB/nm by the end of the 1980s, which is very close to the loss of SMF to date.

Before the late 2000s, intensity modulation direct detection (IMDD) systems were the dominant lightwave systems both in research and product development. These IMDD systems consist of a distributed feedback laser at the transmitter that is directly modulated with a non-return-to-zero (NRZ) signal. The receiver uses a single-ended photodiode to detect the modulated amplitude of the optical signal that traverses a certain length of single-mode fiber connecting the transmitter and the receiver. Before the introduction of EDFAs, signal amplification is realized by electrical regeneration every 40 km of span in order to compensate for the accumulated loss in the fiber. The regeneration is costly due to the optical-to-electrical-to-optical conversion. In 1987, the invention of EDFAs allows optical amplification for the first time and extends the regeneration span to a few hundred kilometers [2]. The high gain, low noise, and compatibility with the IMDD system lead to the wide adoption of EDFAs in long-reach optical communications. The employment of wavelength-division multiplexing (WDM) [3] along with EDFAs, and dispersion-shifted fiber in the 90s enables multi-gigabit IMDD systems over transoceanic distances [4, 5].

As a competing detection scheme of IMDD, coherent detection experienced twists and turns in its development. Coherent detection enjoyed a great deal of interest in the 70s and 80s due to much higher receiver sensitivity compared to IMDD systems, which can translate into an extended regeneration span and thus cost reduction. However, the invention of EDFA and its employment in IMDD systems provide a more cost-effective and simpler approach in extending the regeneration span such that most of the work on coherent detection was abandoned and the focus shifted back to optically amplified WDM-IMDD systems. In addition, the lack of simple approaches to tracking the phase and polarization of the incoming signal also induced a major challenge in developing cost-effective coherent detection systems. The turning point occurred when digital signal processing (DSP) circuits were introduced in coherent detection systems in the latter half of the 2000s following the trend in other fields of communications, i.e. wireless communications and subscriber line systems operating at much lower data rates [6]. Notably, a phase-diverse receiver together with DSP circuits forms a powerful combination, i.e. digital coherent (DCO) detection, which has several major advantages: digital compensation of link impairments, polarization demultiplexing, compatibility with high-order modulation format as well as a high receiver sensitivity [7]. The optical and electrical components for phase and polarization tracking in the analog domain are also eliminated due to DSP algorithms. It is also believed that the revival of coherent detection was attributed to the telecom crash in 2001, which results in an optical data rate stagnating at 10 Gb/s for almost a decade. As the processing speed of DSP circuits gradually caught up with the optical line rate, digital coherent systems became feasible [8]. The line rate of coherent detection per wavelength has evolved from 40 Gb/s ever since towards 2 Tb/s demonstrations in the lab today [9-14].

Given that tremendous investment was spent on laying fiber before the telecom crash, there is a strong incentive to reuse the embedded fiber, especially for long communication distances since the cost of laying new fiber is massive. In order to efficiently utilize the existing fiber infrastructure, i.e. maximizing the capacity per fiber, DCO systems are deployed to substitute IMDD systems in long-haul and submarine optical communications due to higher spectral efficiency and higher capacity without a need for optical dispersion compensation. As the bandwidth demand keeps growing, DCO transceivers are also entertained for shorter-reach use cases such as the metro network [15]. For 100G intra- and inter-data center communications, IMDD systems are dominant due to their cost-effectiveness and low power consumption. To keep pace with the rapid growth of the global data center IP traffic as shown in Fig. 1.1 below [16], the throughput of IMDD systems needs to scale to 400G and beyond to meet the bandwidth demand. Recently, single-wavelength 550 Gb/s throughput has been demonstrated in the lab using 100 GHz bandwidth RF and optical components [17].

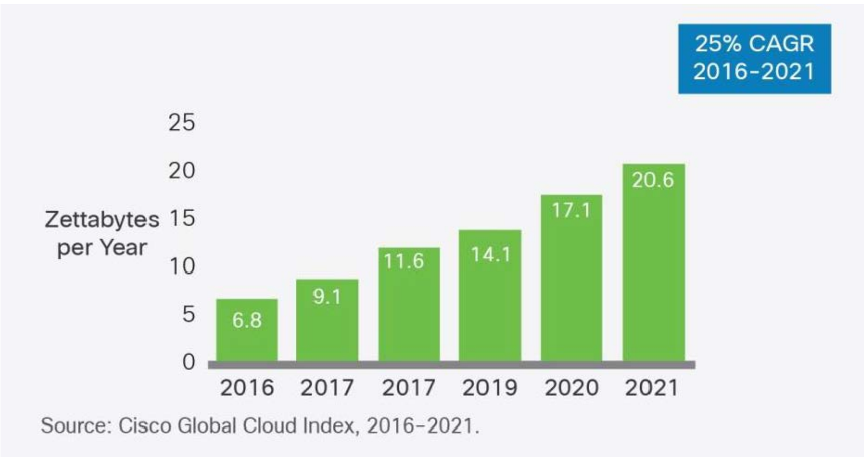

Fig. 1.1. Global data center IP traffic growth [16].

As the system will operate at a higher baud in the future, the performance degradation due to CD will be more severe without using expensive optical dispersion compensation.

The lack of phase diversity of IMDD systems constrains the achievable throughput whether implemented in the C-band or the O-band. By contrast, DCO systems can digitally compensate for CD in the receiver DSP based on the reconstructed signal field and thus are insensitive to the fiber impairments that aggravate with increasing baud. As a result, DCO systems are considered for 400G data center communications at relatively longer distances compared to IMDD systems, e.g. data center interconnects (DCI) at 80 km. In addition, a higher throughput allowed by DCO transceivers reduces the number of optical wavelengths needed to achieve a target throughput [9]. Fewer wavelengths in an optical module reduce the laser count to at least a quarter of that required by IMDD systems given the fiber CD, thereby relaxing the yield requirement of integrated lasers. Nevertheless, DCO systems are still costly and dissipate too much heat for shorter-reach data center communications. These optical modules require compact form factors such as QSFP-DD and OSFP for dense deployment on switch racks, which also poses a tight power budget due to a cooling limit and requires the DCO systems to eliminate unnecessary functions. Thus, there is an ongoing effort in designing simplified DCO systems having lower cost and power consumption, e.g. symbol rate signal processing and low power forward error correction (FEC) [18].

The use of IMDD systems and DCO systems for different reaches of 400G data center communications can be seen from Table 1.1, which lists the latest standards or agreements for these two types of detection schemes in different colors. There are myriads of 400G IMDD specifications either from IEEE standards and or multi-source agreements (MSA) for data center communications up to 40 km. These IMDD modules are specified to adopt a small form factor such as QSFP-DD for a high port density and backward compatibility. In April 2020, Optical Internetworking Forum (OIF) published an implementation agreement termed 400ZR to facilitate an interoperable single-carrier 400G DCO system for up to 120 km DCI applications with optical amplification. The implementation agreement also specifies an unamplified use case for ~40 km connection depending on the laser power and receiver sensitivity.

TABLE 1.1. Latest standards or agreements for 400G optical modules

		400G standards
500m PSM		400GBASE-DR4(IEEE)
2km SMF		400G-FR4(MSA) *400GBASE-FR4(IEEE) 400GBASE-FR8(IEEE)
10km SMF		400G-LR4-10(MSA) 400GBASE-LR8(IEEE)
40km SMF		400GBASE-ER8(IEEE) 400ZR(OIF)
80-120km SMF		400ZR(OIF) *400GBASE-ZR(IEEE)

Direct detection   Coherent detection   *in standardization

Thus, for the current 400G throughput node, IMDD systems and DCO systems are used for data center communications at different transmission distances with the partition shown in Fig. 1.2. It is seen from the figure that DCO systems start to substitute IMDD systems for data center communications at relatively longer transmission reach, i.e. DCI from 40 km to 120 km due to a higher throughput-distance product. By comparison, IMDD systems are dominant for the intra-data center connections below 10 km and 40 km of DCI due to lower cost and power consumption. The gray area around 40 km indicates the transitional region where both systems could be potential solutions. As the throughput node scale to 800G and 1.6T, the boundary is predicted to move further to the left due to a higher throughput per lane enabled by DCO systems having a phase-diverse receiver that is insensitive to fiber CD.

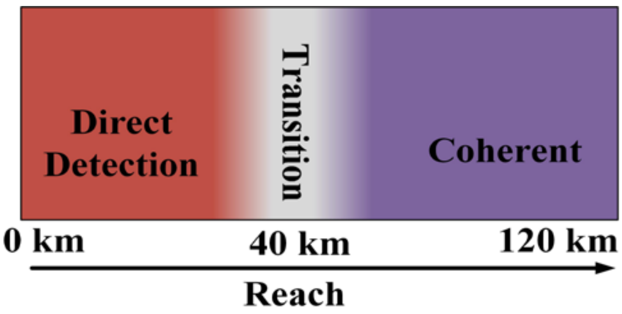

Fig. 1.2. Status of direct detection and coherent detection for 400G data center communications.

1.2. Thesis motivation

As discussed earlier, coherent detection systems are substituting DD systems from long-haul optical communications to shorter-reach use cases such as metro and data center communications. Note that there are varying concerns for different communication use cases. For longer reach data center communications such as DCI greater than 80 km, the cost of laying new fiber is significantly more expensive compared to the cost of transceivers such that it is desirable to improve the capacity of the embedded fiber by deploying DCO systems having higher throughput and spectral efficiency compared to IMDD systems in the dense-wavelength-division multiplexing (DWDM) configuration. By contrast, shorter-reach use cases such as the intra-data center networks are rich in fiber and have abundant spectrum resources such that the cost and power consumption of transceivers become important concerns and IMDD systems outperform DCO systems on this aspect. The stringent power dissipation limit is a consequence of the adoption of compact form factors used such as QSFP-DD for the advantages of backward compatibility and a high port density. As the system scales to higher throughput, the power consumption of optical modules will further increase such that more complex cooling solutions and alternative switch architectures have been discussed.

Thus, IMDD systems and DCO systems are both adopted for 400G data center communications. Compared to IMDD systems, DCO systems have a higher throughput-distance product due to a phase-diverse receiver and 4-dimension modulation, i.e. dual-quadrature and dual-polarization. Nevertheless, DCO systems consume more power and are more complex in terms of the system hardware compared to IMDD systems and thus are considered for longer connection distances, i.e. DCI beyond 40 km. More specifically, a LO is required at the receiver and a thermo-electric wavelength stabilizer is enlisted to align the Tx and Rx wavelength for coherent detection, which constitutes a major source of the entire system power consumption. By contrast, IMDD systems can enable uncooled lasers in coarse wavelength division multiplexing (CWDM) configurations, having a much-relaxed requirement for wavelength management. The DSP chip of DCO systems also needs to carry out extra functions such as polarization tracking, phase recovery, and frequency offset compensation that incurs higher power consumption and more challenges to the DSP ASIC design. By comparison, IMDD systems are simpler in DSP as well as in system hardware and consume less power. However, IMDD systems deliver a lower throughput due to one-dimension modulation such that wavelength-division multiplexing (WDM) is needed to reach an aggregate throughput close to single-wavelength DCO systems. Assuming the same throughput per dimension, IMDD systems need to quadruple the number of lasers compared to DCO systems at a given aggregate throughput, thereby resulting in a yield issue because more lasers are integrated on a photonic chip. Furthermore, due to lack of phase retrieval, the linear channel impairments such as CD cannot be digitally compensated in IMDD systems, which constraints the throughput scaling in the future since the performance degradation due to CD will aggravate at a higher symbol rate.

Recently, there arises the demand for data center connections up to 40 km which do not require expensive DCO transceivers with such a high throughput-distance product. The interconnects between centralized data centers over long distances beyond 100 km can be realized using DCO transceivers, whereas the connections between centralized data centers to tens or hundreds of small edge data centers close to the end-users require cost-effective and low-power transceivers operating at relatively lower throughput and shorter distances below 40 km. Thus, there is the motivation to design advanced DD systems that preserve the simplicity and cost-effectiveness of DD systems while combining the performance advantages exclusively found in DCO systems such as phase-diverse detection, multi-dimension modulation, and flexible spectral efficiency. The advanced DD systems envisioned will narrow the performance gap between DD systems and DCO systems, thereby allowing a greater throughput-distance product and an extended application distance up to 40 km. This objective is accomplished in the thesis by designing novel DSP algorithms and optical subsystems. More specifically, for connection distance below 10 km, the transmission performance is mainly constrained by the transceiver bandwidth and frequency-dependent SNR instead of the fiber impairments such as CD and nonlinearity. In order to best exploit the available link margin, probabilistic shaping, a technique widely used in long-haul DCO systems can be adapted in short-reach DD systems to achieve the optimal trade-off between system ISI and system SNR such that 200 Gb/s throughputs can be enabled using lower bandwidth 100G optics. Moreover, by replacing amplitude modulated signal at the transmitter with self-coherent single-sideband (SSB) signals, the IMDD systems can be transformed into a phase-diverse self-coherent (SC) DD system that allows the signal field reconstruction via direct detection, thereby extending the transmission reach through digital CD compensation in the receiver DSP. We discuss different transmitter subsystems to generate wide-band SC-SSB signals and a potential method to extend the SCDD system to a dual-polarization configuration. Following this, we discuss several approaches to increases the number of modulation dimensions of SCDD systems such that the number of wavelengths is reduced to achieve the same throughput at a given receiver electrical bandwidth.

1.3. Thesis organization

The remainder of the thesis is organized as follows:

Chapter 2 provides the fundamentals on which more advanced concepts and methodologies discussed in the subsequent chapters are established. This chapter starts with the conventional IMDD systems with a description of the basic system components and an analysis of different impairment sources. Next, we cover the classical DSP algorithms used to achieve reliable information transmission for IMDD systems. We show how IMDD systems can be converted into advanced DD systems such as SCDD systems by replacing the amplitude modulated signal with a self-coherent single-sideband signal using the same DD receiver having a single-ended PD. We also discuss the different sources of performance degradation in SCDD systems compared to those in IMDD systems.

In addition, we introduce several widely discussed SCDD schemes and describe in detail the DSP algorithms required to reconstruct the signal field.

Chapter 3 discusses enabling techniques to improve the throughput of IMDD systems for intra-data center connections below 10 km. Our discussion in this chapter focuses on the design of probabilistic shaping schemes that are suitable for short-reach IMDD systems. Compared to conventional modulation formats with discrete information rates (IR) as a power of 2, PS allows flexible IR which is tunable at a fine granularity. As will be shown in this chapter, sending PS signals at an optimized symbol rate in IMDD systems can significantly increase the throughput in bandlimited IMDD systems compared to sending standard PAM formats since an optimal trade-off can be reached between the system ISI and SNR. This chapter experimentally validates the advantage of PS-enhanced IMDD systems by use of a proposed PS scheme termed cost-minimizing distribution matching (CMDM) which allows bits-to-symbol mapping at a much shorter block length compared to the commonly used constant composition distribution matching. Moreover, the chapter discusses a neural network-based scheme proposed for the optimization of the input distribution of PS symbols in realistic IMDD systems.

Chapter 4 introduces advanced DD systems, i.e. SC-SSB DD systems that significantly extend the transmission reach of IMDD systems by replacing the intensity-modulated signal with an SC-SSB signal. SC-SSB-DD systems combine the cost-effectiveness comparable to IMDD systems alongside the phase retrieval capability found in DCO systems, thereby allowing a greater throughput-distance product. This chapter presents two approaches that we propose to generating wideband SC-SSB signals required for high-throughput DD systems. These two approaches both create a phase difference between the two driving RF signals coming from a single DAC channel and can eliminate the need for optical amplification enlisted in vestigial sideband (VSB) systems. In addition, to double the throughput per wavelength of SC-SSB-DD systems at the same electrical bandwidth, this chapter presents a simple scheme to realize polarization-multiplexed SC-SSB-DD systems using only two single-ended PDs and ADCs.

Chapter 5 extends our discussion in Chapter 4 to a novel class of advanced DD systems for self-coherent double-sideband signals having twice the electrical spectral efficiency compared to SC-SSB-DD systems. We refer to this type of SC-DSB-DD system as asymmetric self-coherent direct detection systems due to an asymmetric subsystem structure consisting of two DD branches that will be detailed in this chapter. We will introduce the principle of ASCDD systems, and discuss varied designs of ASCDD systems based on a band-rejection filter, a CD filter, and an MZI structure. All these schemes enable field recovery of SC-DSB signals using a cost-effective DD receiver, which allows digital compensation of channel impairments. We conclude this chapter with a short discussion of the implementation complexity of the proposed ASCDD schemes versus other coherent detection schemes.

Chapter 6 concludes the thesis with a summary of the subtopics discussed in each chapter. We also provide our perspectives on potential research extending from the work presented in this thesis.

1.4. Original contributions

We summarize our original contribution in the thesis below

IMDD systems (Chapter 3)

We validate the effectiveness of probabilistic shaping in realizing high throughput IMDD systems below 10 km for the intra-data center communications. Due to the long symbol block lengths required by the conventional constant composition distribution matching, it is challenging to design a high-throughput digital circuit based on the pipelined sequential logic [19]. We propose to integrate the cost-minimizing distribution matching (CMDM) within the probabilistic amplitude shaping scheme for the generation of PS signals, which can significantly reduce the symbol block length. In addition, we propose two suitable approaches to implement CMDM in IMDD systems. By sending PS signals at the optimized information rate and symbol rate based on the CMDM scheme, we show experimentally that an optimal trade-off can be achieved between the system ISI and system SNR. Based on this approach, we report a first demonstration of net 800 Gb/s 4-lane CWDM system over 2 km of SMF in the O-band using a packaged EML TOSA. Due to the device nonlinearity in IMDD systems, the commonly used Maxwell-Boltzmann distribution is not optimal. We further propose a neural network-based scheme that is experimentally shown to effectively optimize the input distribution of PS constellations for practical IMDD systems. This scheme concatenates a 3-layer neural network with a genetic algorithm to find the optimal symbol distribution based on a trained neural network model. We achieve 23.5% higher throughput at the same spectral efficiency in a 200 Gb/s O-band IMDD system with a silicon photonic modulator.

SC-SSB-DD systems (Chapter 4)

SC-SSB-DD systems attract interest in recent years by enabling the field reconstruction in DD systems for short-reach data center interconnects. As an advanced DD system, SC-SSB-DD systems can significantly increase the throughput-distance product by digital CD compensation in the receiver DSP while maintaining the cost-effectiveness of DD systems. A major problem of SC-SSB-DD systems is the generation of SC-SSB signals having a negligible image band in a cost-effective way for the throughput scaling. Compared to the conventional approaches requiring either two high-speed DAC channels [20] or sharp optical filters [21, 22], we propose two novel transmitter subsystems based on either a quadrature hybrid or a pair of time-misaligned signals combined with a shifted Mux, which require only one DAC channel. These two schemes enable the generation of wide-band SC-SSB signals which could be detected after traveling down 40 km of SSMF without optical amplification given reasonable loss from the multiplexer and demutiplexer. In addition, we develop suitable digital and analog approaches to mitigate the performance degradations resulting from the transmitter subsystems. With optimized system parameters, we demonstrate the first single-carrier net 176 Gb/s amplifier-free transmission over 40-km of reach using the quadrature-hybrid-based scheme, and net 800 Gb/s SSB DWDM systems over 40-km of reach in the C-band using the scheme based on time-misaligned RF signals and a shifted Mux. Furthermore, we extend the SC-SSB-DD system to a dual-polarization configuration where the polarization-division multiplexed (PDM) SC-SSB signals can be detected by a novel DD receiver having two PDs and two ADCs. We report 400 Gb/s interface rate per wavelength over 80 km of SMF in the C-band using this PDM-SC-SSB-DD scheme.

SC-DSB-DD systems (Chapter 5)

Though SC-SSB-DD systems can extend the transmission reach of DD systems, an inherent limit constrains the throughput of SC-SSB-DD systems: the image band is unused and SC-SSB signals have the same electrical spectral efficiency (ESE) as intensity-modulated signals. In order to improve the ESE, we propose a class of DD schemes for the field reconstruction of SC-DSB signals that we refer to as asymmetric self-coherent direct detection (ASCDD). The ASCDD schemes can approach the ESE of homodyne coherent detection systems, thus doubling the ESE of SC-SSB-DD systems using a cost-effective DD receiver having two reception paths. Compared to the previously proposed SC-DSB-DD schemes, the ASCDD scheme has a simplified system structure requiring only two PDs and two ADCs at the receiver instead of 5 PDs and 3 ADCs in [23], which leads to lower optical power required for the detection. We evaluate the theoretical performance of various types of ASCDD schemes having either a band-rejection filter, a chromatic dispersion filter, or an MZI in a DD receiver. We experimentally validate the principle of the ASCDD scheme and demonstrate 200 G DD systems over 40 km of SSMF based on the ASCDD scheme.

2 Fundamentals of direct detection systems

2.1. Overview

In this chapter, we present the fundamentals of direct detection systems that our discussions in the following chapters rely on. We start by describing classic IMDD systems and proceed to discuss the recently emerged advanced DD systems such as SC-SSB-DD systems which attracts a great deal of interest in recent years. We will discuss the constituent parts of these DD systems as well as various impairments from the system or the fiber channel. Finally, we review classic DSP blocks used in the transmitter and receiver to realize high-speed DD systems.

2.2. Intensity modulation direct detection systems

2.2.1. System structure

In typical IMDD systems, the information is modulated onto the signal intensity or amplitude and extracted from the photocurrent produced as the incident optical signal impinges upon a reversely biased photodiode, creating electron-hole pairs in the depletion region. The photocurrent is proportional to the power of the incoming optical signal with an associated coefficient referred to as the responsivity, which indicates the opto-electro conversion efficiency. This detection process is also commonly referred to as the square-law detection since the photocurrent is proportional to the square of the field amplitude and the phase information is completely removed. Compared to coherent detection, though the need to track the carrier phase is eliminated when the information is downconverted from the optical domain to the electrical domain, a limited modulation dimension is imposed, i.e. only the field amplitude.

We need to mention that it is important to amplify the photocurrent in order to improve the power sensitivity of an IMDD system. As such, the photodiode can also be engineered to amplify the photocurrent through the avalanche effects. This type of photodiodes is called avalanche photodiodes (APD). APDs multiply the number of electron-hole pairs by accelerating the photon-generated carriers under a high electric field in the depletion region such that a valence band electron is knocked to the conduction band, creating more electron-hole pairs as it moves. Another approach to improve the receiver sensitivity is to concatenate a trans-impedance amplifier with the PD. Amplification of the photocurrent is necessary due to the presence of the electrical noise including the thermal noise, flicker noise, and the generation-recombination noise.

The intensity modulation can be realized using different transmitter subsystems. A common approach is to use a CW laser together with a Mach-Zehnder modulator in a serial-push-pull configuration so that information is encoded onto the carrier intensity without incurring any chirp. For this type of transmitter, we note that an increasing interest in recent years on the silicon-on-insulator platform [24-27]. This is even more so in the intra-data center use case where the cost mostly resides in the transceiver themselves instead of laying fiber. Thus, Si-based chips are desirable due to their high yield and cost-effectiveness. Alternatively, EMLs and DMLs are also cost-effective components for a short-reach below 10 km with high-speed demonstrations reported in the lab in recent years [28-31].

2.2.2. System impairments

A. Chromatic dispersion and chirp

The performance of IMDD systems in the C-band or at a wavelength far from 1310 nm in the O-band is degraded by the CD-induced power fading, i.e. sharp spectral dips distributed in the frequency domain following the expression $\cos\left(2\pi^2 f^2 \beta_2 L\right)$, where f is the frequency, L is the transmission distance, and β_2 is the second-order derivative of the propagation constant β at the carrier wavelength. Denoting the input power as $P_{in}(t)$ and assume no phase modulation, i.e. no chirp, the amplitude can be expressed as $A_{in}(t)=\sqrt{P_{in}(t)}$. We decompose $A_{in}(t)=\langle A_{in}(t)\rangle + A_{in,s}(t)$, where $\langle x\rangle$ is the time average of $A_{in}(t)$, and $A_{in,s}(t)$ is the modulated signal amplitude. The square-law detection produces a photocurrent proportional to the optical power as expressed below

$$P_{out}(t)=\left|\langle A_{in}(t)\rangle + A_{in,s}(t)\otimes h_{CD}(t)\right|^2 \approx \left|\langle A_{in}(t)\rangle\right|^2 + 2\langle A_{in}(t)\rangle \mathrm{Re}\left(A_{in,s}(t)\otimes h_{CD}(t)\right) \quad (2.1)$$

where $h_{CD}(t)$ is the transfer function of the chromatic dispersion, and the modulus squared of the modulated signal amplitude is ignored. By Fourier transforming (2.1), we have the frequency-domain optical power expressed below

$$P_{out}(f)\approx \left|\langle A_{in}(t)\rangle\right|^2 + 2\langle A_{in}(t)\rangle A_{in,s}(f)\cos\left(2\pi^2 f^2 \beta_2 L\right), \quad (2.2)$$

and therefore the faded power spectrum with spectral dips distributed at

$$f_n=\sqrt{\frac{1+2n}{4\pi\beta_2 L}}, \quad (2.3)$$

where n takes non-negative integers. It follows that at a given transmission reach, we can calculate β_2 and thus the dispersion parameter of the fiber channel by measuring the spectral position of the dips. However, this becomes more complicated when the intensity modulation is accompanied with the phase modulation, i.e. chirp, and the correlation between these effects needs to be determined in order to derive the power spectrum. Based on the small-signal analysis, [32] derives the expression below for the power of the optical signal that traverses a fiber channel given that the modulated signal possesses a certain amount of chirp

$$P_{out}(f)=\left(\cos\left(2\pi^2 f^2 \beta_2 L\right) - H(f)\sin\left(2\pi^2 f^2 \beta_2 L\right)\right)P_{in}(f) \quad (2.4)$$

where $H(f)$ is a transfer function that describes the relation between intensity modulation and phase modulation. $\phi_{in}(f)$ is proportional to $P_{in}(f)H(f)$, where $\phi_{in}(f)$ is the phase modulation in the frequency domain. The exact form of $H(f)$ requires knowledge of the transmitter physics, e.g. the rate equation of lasers, which is beyond the scope of this chapter. Readers who are interested in knowing the derivation of $H(f)$ can refer to relevant papers in [32-34]

B. Intersymbol interference (ISI)

Another issue with IMDD systems is ISI. There are different ways to achieve a higher throughput per fiber, i.e. (a) increase the baud (b) increase the spectral efficiency, and (c) use more wavelengths. Option (c) is less appealing since more parallel lanes adopted within a small form factor transceiver requires proportionally more optical and electrical hardware, thus becoming more vulnerable to the yield problem. Option (a) is the most straightforward among the three options but faces the bandwidth constraint of the optical and electrical components used in the system. Without careful management of the signal pulse shape, the ISI can severely degrade the system performance. Thus, pre-equalization and post-equalization are often used in transmission systems at the transmitter and receiver, respectively, to mitigate the ISI resulting from the low-pass response of the system. According to the Nyquist condition for zero ISI, the Fourier transform of the signal pulse shape $x(t)$ needs to satisfy the following equation

$$\sum_{m=-\infty}^{\infty} X\left(f+m/T\right)=T \tag{2.5}$$

where $X(f)$ is the Fourier transform of $x(t)$, T is the symbol duration. Apart from the ISI induced by the limited electrical bandwidth of the system, ISI is also attributed to the change of the phase response, e.g. fiber CD which also destructs the Nyquist condition for zero ISI.

C. Noise sources

The noise sources in IMDD systems limit the highest achievable SNR. The spontaneous emission causes the relative intensity noise of lasers and the ASE noise of optical amplifiers. Thermal noise exists in all electrical devices in the system including the DAC, ADC, driver amplifiers, TIAs, lasers, and PDs. Due to a relatively high optical power, the impact of the shot noise is dwarfed by other noise sources. There is also quantization noise from the ADC and DAC due to a nominal N number of bits used for the analog-to-digital conversion and vice versa, respectively. The effective number of bits (ENOB) is lower than N since the noise term also includes all sorts of distortions in the calculation including signal harmonics, timing jitter, differential nonlinearity, and integral nonlinearity that comes with the converters [35].

D. Nonlinearity

In the C-band, the nonzero CD makes it hard to meet the phase-matching condition for the FWM to efficiently happen, whereas in the O-band a large channel spacing is often set in the system such that the higher-order dispersion terms contribute to the destruction of the PM condition. Thus, fiber nonlinear effects such as SPM and XPM that automatically achieve the PM condition have a more significant impact on the system performance. However, due to a relatively short transmission reach in the data center network, the fiber nonlinear effect is not a major concern compared to other channel impairments given that the launch power and the channel spacing are properly configured. On the other hand, the system is affected by nonlinearity resulting from the optical and electrical components in the system. For instance, the transfer function of an MZM is sinusoidal and the phase shifter in each MZM arm does not change linearly following the driving signal. In addition, the driver amplifier and the TIA when operated close to the compression region distort the input signal and degrade the signal quality. However, it is sometimes necessary to trade signal linearity for higher signal power in order to combat the electrical noise of the system.

E. Multipath interference

Standard organizations also set a limit for the maximum fiber connector return loss so that the system performance will not be considerably degraded by multipath interference (MPI). MPI is caused by double reflections of the optical signal at any two fiber connector interfaces across the entire system. The reflected interferences superimpose with the forward propagating optical signal, thereby deteriorate the transmission performance. The optical field incident to the PD with MPI can be expressed as follows

$$E(t) = E_S(t)e^{j\phi(t)} + \sum_{k=1}^{N} \sqrt{R_k^2} \cos\alpha_k E_S(t-\tau_k)e^{j\phi(t-\tau_k)}, \tag{2.6}$$

where $E_S(t)$ is the field of the optical signal, $\phi(t)$ is the laser phase noise, R_k^2 is the reflectance, α_k and τ_k is the relative polarization angle and the delay between the optical signal and the *k*th reflected interference.

2.2.3. Classical DSP algorithms for IMDD transceivers

A. Pre-emphasis

As discussed in 2.2, modern IMDD systems are operating at a high symbol rate in order to deliver high throughput. The baud is often higher than the 3-dB bandwidth of the system, thus resulting in severe ISI if not properly handled. Similar to digital coherent detection, equalization algorithms are also introduced in IMDD systems to counteract the ISI due to a high baud and the bandwidth limitation. Digital equalizers are applied both at the transmitter and the receiver with the former one referred to as pre-emphasis since the high-frequency components are enhanced giving rise to a response that resembles a partial inverse of the channel transfer function. Without transmitter pre-emphasis, the noise enhancement caused by the equalization at the receiver will be more pronounced and leads to more deteriorated transmission performance. Note that there are engineering trade-offs when implementing pre-emphasis at the transmitter: a) the signal PAPR increases, b) the signal power decreases, and c) the signal SNR decreases [36]. Consequently, it is more suitable to pre-compensate only part of the channel low-pass response. Due to current optical and electrical device technology, the transmitter bandwidth is often much lower than the receiver bandwidth such that a great amount of effort has been invested into optimizing pre-emphasis filters to flatten the transmitter response [37]. In this case, the pre-emphasis of the transmitter can be schematically depicted below

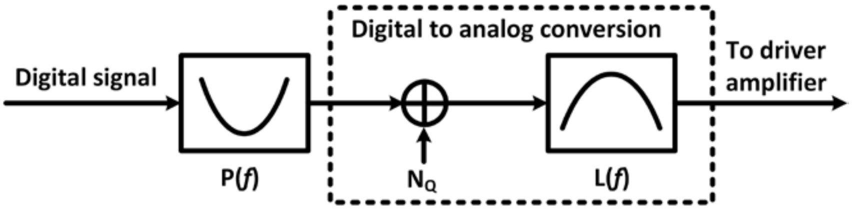

Fig. 2.1. Schematic of pre-emphasis.

where P(*f*) is the digital pre-emphasis filter, N_Q is the quantization noise and L(*f*) is the low-pass response of the DAC. It should be noted that analog pre-emphasis is also feasible based on either optical or RF devices.

B. Pulse shaping

The received signal can be formulated as

$$R(t) = \sum_{n=0}^{\infty} S_n P(t - nT) \tag{2.7}$$

where $\{S_n\}$ is the transmitted symbols, $P(t)$ is the pulse shape, and T is the symbol duration. The condition for zero ISI requires that

$$P(t) = \begin{cases} 0, & t = nT \\ 1, & t = 0 \end{cases} \tag{2.8}$$

where n is an integer. This leads to the Nyquist pulse-shaping criterion for zero ISI as discussed in section 2.2. A commonly used pulse shape with zero ISI in optical communication systems is the raised-cosine (RC) pulse shape, which has the form below

$$P_{RC} = \begin{cases} T, & 0 \le |f| < (1-\alpha)/2T \\ T/2\left\{1-\sin\left[(\pi T/\alpha)\left(|f|-1/(2T)\right)\right]\right\}, & (1-\alpha)/(2T) < |f| < (1+\alpha)/(2T) \\ 0, & |f| > (1+\alpha)/(2T) \end{cases} \tag{2.9}$$

where α is the roll-off factor of the RC pulse-shaping filter and controls the excess bandwidth beyond $1/(2T)$. In the time domain, the RC pulse shape is expressed as below

$$s(t) = \mathrm{sinc}(\pi t/T)\frac{\cos(\pi\alpha t/T)}{1-4\alpha^2 t^2/T^2} \tag{2.10}$$

We can also implement the RC pulse shaping partly at the transmitter and partly at the receiver, forming a pair of matched filters, i.e. root-raised-cosine (RRC) pulse shaping filters. The matched filter principle requires that the response of the receiver filter is the complex conjugate of the transmitter filter in order to maximize the SNR in the presence of noise. Thus, the matched filters can be readily chosen as the square root of the RC filter as expressed below

$$P_{RRC} = \begin{cases} \sqrt{T}, & 0 \le |f| < (1-\alpha)/2T \\ \sqrt{T/2\left\{1-\sin\left[(\pi T/\alpha)\left(|f|-1/(2T)\right)\right]\right\}}, & (1-\alpha)/(2T) < |f| < (1+\alpha)/(2T) \\ 0, & |f| > (1+\alpha)/(2T) \end{cases} \tag{2.11}$$

C. Modulation format

Numerous modulation formats have been demonstrated in IMDD systems. The pulse-amplitude-modulation (PAM) formats which consist of multiple levels are the most commonly used in IMDD systems due to low implementation complexity. The spectral efficiency of PAM signals can be scaled by changing the number of discrete levels per symbol. It should be noted that high order PAM signals with high SE also require high system SNR to achieve a BER above the pre-FEC BER threshold. However, IMDD systems often operate at high baud and have deteriorated SNR due to residual ISI, lower ENOB at a higher frequency due to timing jitter, and so forth. The SNR of PAM formats can be visualized using eye diagrams. A large eye-opening indicates a good SNR for the chosen modulation format.

It is known that for an AWGN memoryless channel, the channel capacity is achieved by transmitting a signal following a Gaussian distribution under a given power constraint.

Practical systems use discrete signal levels such as the pulse-amplitude modulation (PAM) for information transmission. However, there is no analytical expression for the optimal input distribution of discrete-level modulation format under an input power constraint. Probabilistically shaped signals often follow the Maxwell-Boltzmann distribution, which performs well in the reported demonstrations [38, 39] and has the highest entropy at a given signal power. Though it is still debatable whether an IMDD system can be best modeled as an average power-constrained system or a peak power-constrained system or something in between, the use of PS in IMDD systems allows fine-tuning of the SE. This functionality is important for maximizing the system throughput in bandlimited systems by optimizing the trade-off between the system bandwidth and the system SNR.

The constant composition distribution matching (CCDM) is a common technique to implement probabilistic shaping [40]. CCDM maps a fixed length of bits to a fixed length of symbols with a desired distribution based on the arithmetic coding. Note that it has an entropy loss, i.e. the gap between the actual SE and the entropy of the symbols, which asymptotically decreases to zero with the increasing length of the symbol blocks. The explanation is that for a given symbol block length, CCDM chooses symbol sequences with the same Euclidean distance in R^n, which constitutes part of the boundary of a super sphere composed of discrete constellation dots. Nevertheless, a more energy-efficient strategy to implement PS at the same SE is to make use of inner dots with shorter Euclidean distance inside the surface of the super sphere. However, at a large dimension n, the volume i.e. the total number of constellation dots within and on the boundary of the hypersphere is approximately equal to the sphere boundary, which is referred to as sphere hardening [41]. This indicates that CCDM needs a large block length in order to minimize the entropy loss, which increases the implementation complexity and power consumption of the ASIC, e.g. very long pipelining.

It is also noted that the FEC encoding can disrupt the symbol distribution when implemented after PS, whereas the other way around causes burst bit errors that the FEC decoder may not be able to correct. Thus, PS is often used within the probabilistic amplitude shaping (PAS) scheme to realize coded modulation as depicted below. The information bits are divided in to two tributaries, where β information bits are mapped to 1 half positive PAM symbol, whereas α information bits are needed to generate enough sign bits.

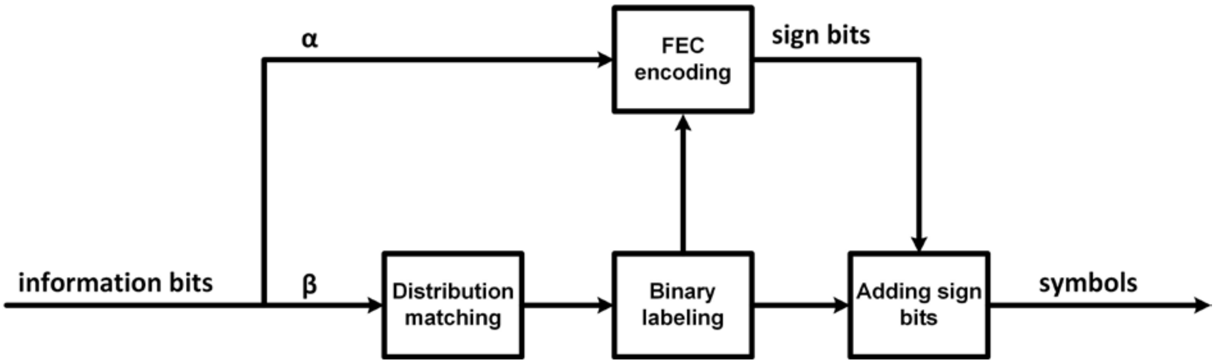

Fig. 2.2. PAS scheme.

The symbols after distribution matching are labeled based on the binary reflected Gray coding which generates the parity bits alongside the α information bits. The parity bits are utilized as sign bits to flip the half positive PAM symbols in order to produce complete PAM symbols. As for the generation of coded QAM symbols, we can either perform the PAS scheme for the in-phase and quadrature symbols separately or produce symbols in the first quadrant first and use the sign bits to select the corresponding quadrant. Given a code rate *c*, the information rate for PAM-N symbol is

$$IR = \alpha + \beta = 1 + (c-1)\log_2 N + \beta \tag{2.12}$$

D. Equalization

Distortion of the frequency response broadens the transmitted pulse and induces ISI. It is known that with the help of a whitened matched filter (WMF), the received T-spaced samples can be modeled based on the following diagram in Fig. 2.3.

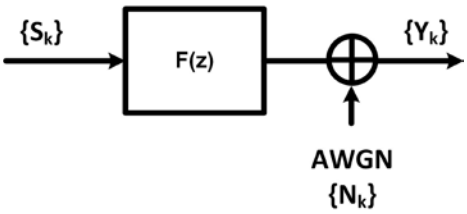

Fig. 2.3. Schematic diagram of an ISI channel with AWGN.

$\{S_k\}$ are the transmitted symbols, F(z) is the effective channel transfer function which is monic and loosely causal, N_k is AWGN samples, and $\{Y_k\}$ are the received samples. The cascade of a maximum likelihood sequence estimator (MLSE) realizes the optimum detection under the maximum likelihood criterion. However, the implementation of MLSE is computationally expensive even by means of the Viterbi algorithm. The trellis-based algorithm requires that for each received symbol with *L* post-cursor ISI symbols and an alphabet size of *M*, M^{L+1} branch metrics need to be calculated and grows exponentially with *L*. Thus, the MLSE is only feasible under a small *L* and *L* often equals 1 when actually used in IMDD systems in order to suppress the enhanced noise alongside a post-filter working as a noise whitening filter [42].

Due to the above reasons, linear transversal filters are often used in realistic systems owing to low complexity. The outputs of such filters are expressed as

$$Z_k = \sum_{j=0}^{L} c_j Y_{k-j} \tag{2.13}$$

where $\{c_k\}$ are the taps of the linear filter. A widely known linear filter is the zero-forcing filter $1/F(z)$ which simply inverts the effective channel transfer function and completely compensates for the ISI. The ISI compensation by the ZF filter is accompanied by noise enhancement due to a noise PSD expressed as $P_N(\omega) = N_0 / \left|F\left(e^{j\omega T}\right)\right|^2$. This is obviously not the optimum filter since around the null frequency of $F\left(e^{j\omega T}\right)$ the noise PSD is infinitely amplified. More commonly used is the mean square error (MSE) based linear equalizers that minimize the average Euclidean distance between each transmitted information symbol and the symbol at the output of the linear equalizer, which leads to the following noise PSD $P_N(\omega) = \left(N_0 \left|F\left(e^{j\omega T}\right)\right|^2\right) / \left(\left|\left|F\left(e^{j\omega T}\right)\right|^2 + N_0\right|^2\right)$. Due to the term N_0 in the denominator, the noise enhancement is relaxed compared to the ZF filter.

It should be noted that the T-spaced equalizer has a stringent requirement of the timing phase and has aliased spectrum for non-Nyquist pulses, e.g. RC pulses with a zero roll-off factor. Thus, fractionally spaced linear equalizers are often used in optical communication systems to enable the compensation of different linear channel impairments including CD without spectrum aliasing. In particular, the T/2-spaced equalizer is most often used which ensures no aliasing even with the highest excess bandwidth of RC pulses.

2.3. Self-coherent single-sideband direct detection systems

2.3.1. System structure

Self-coherent (SC) single-sideband (SSB) direct detection (DD) system is a different DD scheme widely pursued in recent years due to its capability of extending the transmission reach compared to IMDD systems. Both the SC-SSB-DD systems and the IMDD systems remove the need for local oscillators (LO) at the receiver compared to coherent detection systems and thus are more cost-effective for the data center connections at a shorter reach. SC-SSB-DD systems address several major problems that constrain the attainable throughput of IMDD systems at a relatively long transmission distance including the power fading due to accumulated CD. We describe a general SC-SSB-DD system using the schematic depicted in Fig. 2.4.

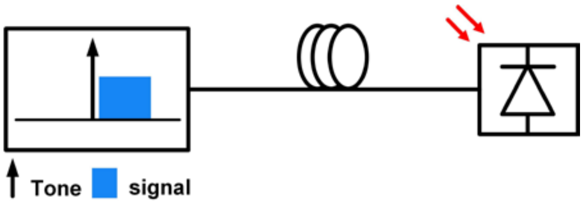

Fig. 2.4. Schematic diagram of an SC-SSB-DD system.

The transmitted optical signal is an SC-SSB signal which is comprised of an SSB signal and a co-propagating CW-tone. The SC-SSB-DD system has the same receiver front-end, i.e. a single-ended PD as the IMDD system. The difference is that in IMDD systems, the information bits are encoded onto the modulated signal intensity, whereas in SC-SSB-DD systems, the information bits are encoded onto the complex signal field. Consequently, the optical signal incident to the PD considering the CD can be expressed as

$$\begin{aligned} R(t) &= \left|C + S \otimes H_{CD}\right|^2 \\ &= \left|C + S'\right|^2 \\ &= C + 2C\,\mathrm{Re}(S') + \left|S'\right|^2 \end{aligned} \tag{2.14}$$

where C is the CW-tone, S is the signal, H_{CD} is the frequency response of the CD, and $S' = S \otimes H_{CD}$. Note that H_{CD} does not change the amplitude response of the signal and thus S' remains an SSB signal. It is known that the field of SSB signals can be recovered provided a known real or imaginary part. In (2.14), $S' = \mathrm{Re}(S') \pm j \bullet Hilbert\left(\mathrm{Re}(S')\right)$, where $Hilbert(x)$ is the Hilbert transform of x, and $\pm$ depends on whether the signal is a right sideband signal or a left sideband signal. As a result, the CD can be compensated based on the recovered S' and note that $S' = S \otimes H_{CD}$, which indicates that the power fading problem does not exist if the information bits are coded onto the SSB signal and larger throughput-distance produced can be obtained.

However, we need to also consider the additional hardware complexity involved in generating SC-SSB signals compared to IM signals. First, the generation of a CW-tone that travels down the fiber together with the signal is an issue. Fig. 2.5 depicts a typical transmitter structure for SC-SSB signals.

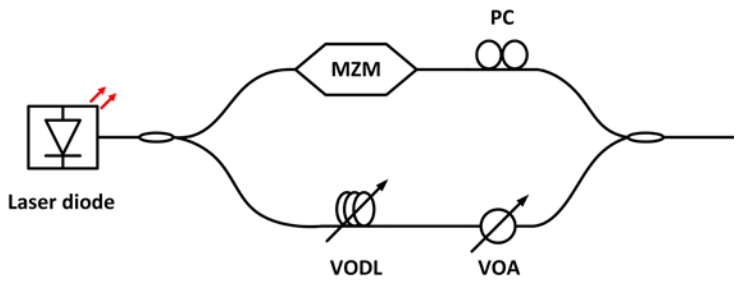

Fig. 2.5. Schematic diagram of an SC-SSB-DD transmitter.

The optical carrier from the laser diode is split into two portions that go to different optical paths. The portion in the upper path is modulated by an IQ-MZM, whereas the portion in the lower branch forms the CW-tone that recombines with the signal via a coupler. Note that a polarization controller (PC) is required to align the polarizations of the CW-tone and the signal and a variable optical delay line (VODL) is used to ensure the coherence of the split carriers. A variable optical attenuator (VOA) is used to control the carrier to signal power ratio that affects the performance of the SC-SSB-DD system.

There are also other ways to generate SC-SSB-DD signals. For instance, the lower branch can be removed by digitally generating the CW-tone which is often called 'virtual carrier' [43]. In [44], a separate laser is used to generate the tone instead of splitting an optical source in two. We will discuss other approaches to cost-effectively generating high baud SC-SSB signals in chapter 4.

2.3.2. System impairments

As discussed in the last subsection, the power fading problem is avoided in SC-SSB-DD systems because the field of the SSB signal can be reconstructed allowing the digital compensation of CD. However, the performance of SC-SSB-DD system is still affected by the ISI, noise, and device nonlinearity in a similar way as described in 2.2.2. We also need to mention that the performance of SC-SSB-DD system is impacted by the signal-signal beating interference (SSBI), which is $|S'|^2$ in (2.14). The SSBI, if not handled carefully, will overlap with the signal in the spectrum after DD, which significantly degrades the system performance under a relatively low CSPR.

2.3.3. Classical DSP algorithms for SCDD transceivers

In this subsection, we present commonly used DSP algorithms to mitigate the SSBI in SC-SSB-DD systems since other DSP blocks such as pre-emphasis, equalization, and modulation can be performed in a similar way as in IMDD systems. Before we discuss the technical details, we need to clarify the field reconstruction via DD for SC-SSB signals. Fig. 2.6 shows the baseband spectrum of the detected SC-SSB signal. Without loss of generality, we ignore the linear coefficients that should be appended to the signal in the figure. It is seen that the spectrum of the signal becomes Hermitian as specified by $\mathrm{Re}(S')$ in (2.14). The orange triangle represents the SSBI with an increasing power towards zero frequency.

Fig. 2.6. Optical to electrical conversion of SC-SSB signals.

Thus, a quickly seen approach is to keep the signal farther away from the CW-tone, i.e. to set a wider guard band, such that the impact of the SSBI is alleviated as illustrated in Fig. 2.7. This approach comes at the cost of a higher required electrical bandwidth for the PD and ADC, which becomes expensive for systems operating at a high symbol rate.

Fig. 2.7. Optical to electrical conversion of an SC-SSB signal with a wide guard band.

We can also trade complexity for higher electrical spectral efficiency. Fig. 2.8 shows an iterative scheme to estimate and subtract the SSBI. Instead of using a wide guard band, this scheme gives an SSBI estimate (c) based on a recovered SC-SSB signal (b) affected by the SSBI. (c) is removed from the original baseband signal (a) in order to improve the SNR of the recovered signal (b). This process is performed iteratively to mitigate the SSBI.

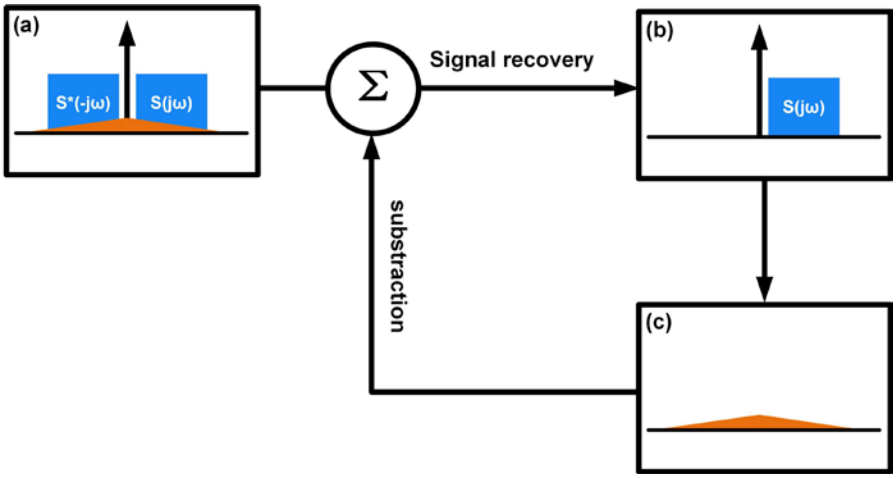

Fig. 2.8. Iterative SSBI mitigation algorithm.

It is also shown in [45] that for SC-SSB signals contained between -B and B and formulated as $P(t)=C+S(t)\exp(-jBt)$ with $|C|>|S(t)|$, the phase of the signal can be extracted in the frequency domain based on the amplitude of the optical signal following the formula $\phi(\omega)=Hilbert\left(\log\left[|P(t)|\right]\right)$. Expressed in the time domain, the phase

$$\phi(t)=\frac{1}{\pi}\lim_{R\to\infty}\int_{-R}^{R}\frac{\log\left[|h(t')|\right]}{t-t'}dt' \tag{2.15}$$

is the principal value of an improper integral. Thus, the signal $S(t)$ is reconstructed without SSBI based on the retrieved phase and the signal amplitude known via DD and a higher ESE is obtained. This approach is called Kramers-Kronig (KK) coherent detection. Despite the elimination of iteration, the KK algorithm has its downside. $\log\left[|P(t)|\right]$ is not bandlimited, thus requiring a higher sampling rate in the receiver DSP. Moreover, the Hilbert transform performed in the frequency domain requires a pair of Fourier and inverse Fourier transforms. In addition, the low pass response of the PD distorts the amplitude response of $|P(t)|$ which degrades the performance of the field reconstructed based on KK detection. All these problems of KK detection have motivated the search for effective solutions in order to improve the application potential of KK systems [46-48].

3 Intensity modulation and direct detection systems

3.1. Overview

As discussed in chapter 1, the IP traffic has been growing rapidly within the data centers. At 400G throughput node, IMDD systems are dominantly used for intra-data center communications below 10 km. After the deployment of 400G-FR4 transceivers in 2020, standard organizations including IEEE and MSA have been working on specifications for the next-generation 800G-FR transceivers [49]. It is also not uncommon to hear discussions on potential routes towards 1.6T transceivers recently [50, 51]. Though 800G and 1.6T transceivers can be realized by multiplexing 8 or 16 wavelength signals based on mature single-lane 100G systems, the component count can be significantly reduced by scaling the throughput per lane to 200 Gbit/s, which in the meantime can alleviate the yield loss of photonic chips [51]. 200 Gbit/s per lane can be achieved by either increasing the symbol rate or using higher-order PAM signals. However, transmitting 107 Gbaud PAM-4 signals assuming a 7% overhead hard-decision forward error correction (HD-FEC) code will induce a very high bandwidth requirement that is challenging for the design of electrical and optical components [52]; on the other hand, higher modulation formats such as PAM-8 imposes a stringent requirement on the signal SNR even when the state-of-art devices and test equipment are utilized. Thus, it is desirable to transmit PAM signals at intermediate spectral efficiencies (SE) which is ideally tunable such that a balance can be reached between the system SNR and bandwidth and higher throughput can be achieved.

Probabilistic shaping (PS) is widely used in DCO systems for metro and long-haul optical communications and can provide flexible control of the signal SE with fine granularity. In AWGN channels, PS signals have an ultimate shaping gain of 1.53 dB at a given signal power. Though IMDD systems cannot be strictly modeled as average power-limited AWGN channels due to device nonlinearity and no optical amplification, shaping gain can still be obtained with optimized input symbol distribution [53]. In addition, if the signal is clipped to a certain peak-to-average power-ratio (PAPR) the channel is shown to approach an AWGN channel [54]. Note that these advantages of PS come at the cost of higher implementation complexity compare to the commonly used modulation formats, e.g. the bits to symbol mapping based on CCDM requires iterative processing with a very long symbol block length in order to reduce the rate loss. Moreover, the optimization of the input distribution is often realized based on an analytical system model which is challenging to construct and can have significant errors. In this chapter, we will discuss schemes proposed to solve these issues and show experimental results that validate these schemes in 200 Gb/s per lane IMDD systems. The chapter is organized as follows: in section 3.2, we descript the use of CMDM within the PAS structure to realize shaping with an ultra-short block length; in section 3.3, we detail a scheme based on a 2-hidden layer neural network which optimizes the input distribution for practical IMDD systems. We conclude this chapter in 3.3 with a few remarks on the potential impact of the proposed techniques.

3.2. Probabilistic shaping for high-speed IMDD systems

3.2.1. Introduction

As discussed earlier, probabilistic shaping (PS) is a technique widely used in long-haul optical communications to approach the Shannon limit. In recent years the use of PS has also been reported in high-speed IMDD demonstrations. [55] reports a first demonstration of 56 Gbaud PS-PAM-8 over 135-km. Then in [56], an efficient labeling scheme was presented for asymmetric PS-PAM signals for unipolar power-constrained IMDD systems. High single-lane throughput up to 554 Gbit/s is also reported in an IMDD experiment using PS [57]. These papers all used the constant composition distribution matcher (CCDM) to generate PS-PAM signals. However, CCDM achieves the maximum rate asymptotically as the block length goes to infinity [19]. Thus, over 100 symbol block length is usually required to avoid significant entropy loss, which is challenging to implement in the DSP due to the sequential nature of arithmetic coding (AC). In these demonstrations [51-53], SD-FEC codes are often used and concatenated with CCDM within the probabilistic amplitude shaping (PAS) scheme [58] such that iterative soft decoding is needed, which results in higher power consumption, a larger circuit footprint, and a higher delay compared to hard-decision (HD) FEC codes. Hence, CCDM-based PS-PAM signaling with SD FEC codes is not necessarily viable for the intra-data center interconnect, where low-latency and low-power consumption are the priorities.

In this section, we integrate the cost-minimizing distribution matching (CMDM) into the PAS scheme assuming HD-FEC codes to enable the generation of PS-PAM signals using a short symbol block length in a 2-km IMDD system in the O-band [59]. CMDM was developed in the 90s with a variation adopted in the V.34 modem standard to achieve shaping gain with trellis codes [60]. In recent years, CMDM was also considered for low-latency wireless communications [61] and was demonstrated in an optical coherent system [62]. Herein, we assume a staircase code with a BER threshold of 5.54×10^{-3} to encode the PS-PAM symbols for error-free decoding [63]. We detail the principle of CMDM and presents two different ways of implementation either using look-up tables (LUT) or by means of index locating (IL). Next, we transmit single wavelength net 200 Gbit/s PS-PAM signals over 2 km of single-mode fiber (SMF) using CMDM and CCDM. We found that CCDM achieves nearly the same performance yet requiring a much longer symbol block length of 70 as opposed to 7 by CMDM. Furthermore, we report in this letter, to our knowledge, a first demonstration of net 800 Gbit/s IMDD system over 2 km of SMF using a packaged coarse wavelength division multiplexing (CWDM) electro-absorption modulated laser (EML) TOSA.

3.2.2. Principle of CMDM

CMDM maps fixed-length bit sequences to fixed-length symbol sequences, which allows tunable SE using a short symbol block length while not introducing significant entropy loss. Herein the entropy loss (EL) is defined as $H(x)$-IR, where $H(x)$ and IR are the entropy and information rate of the shaped symbols, respectively. In order to avoid burst errors resulting from deshaping, we concatenate an HD-FEC encoder after CMDM within the PAS structure as depicted in Fig. 3.1 (a). We present two different approaches to implement CMDM. One is by using LUTs and the other is by means of IL. Since CMDM enables shaping using a short symbol block length as will be shown later, the LUT-based implementation does not require a large memory footprint of the digital processor. Below we first detail the LUT-based CMDM using a specific example where we generate PS-PAM 6 symbols.

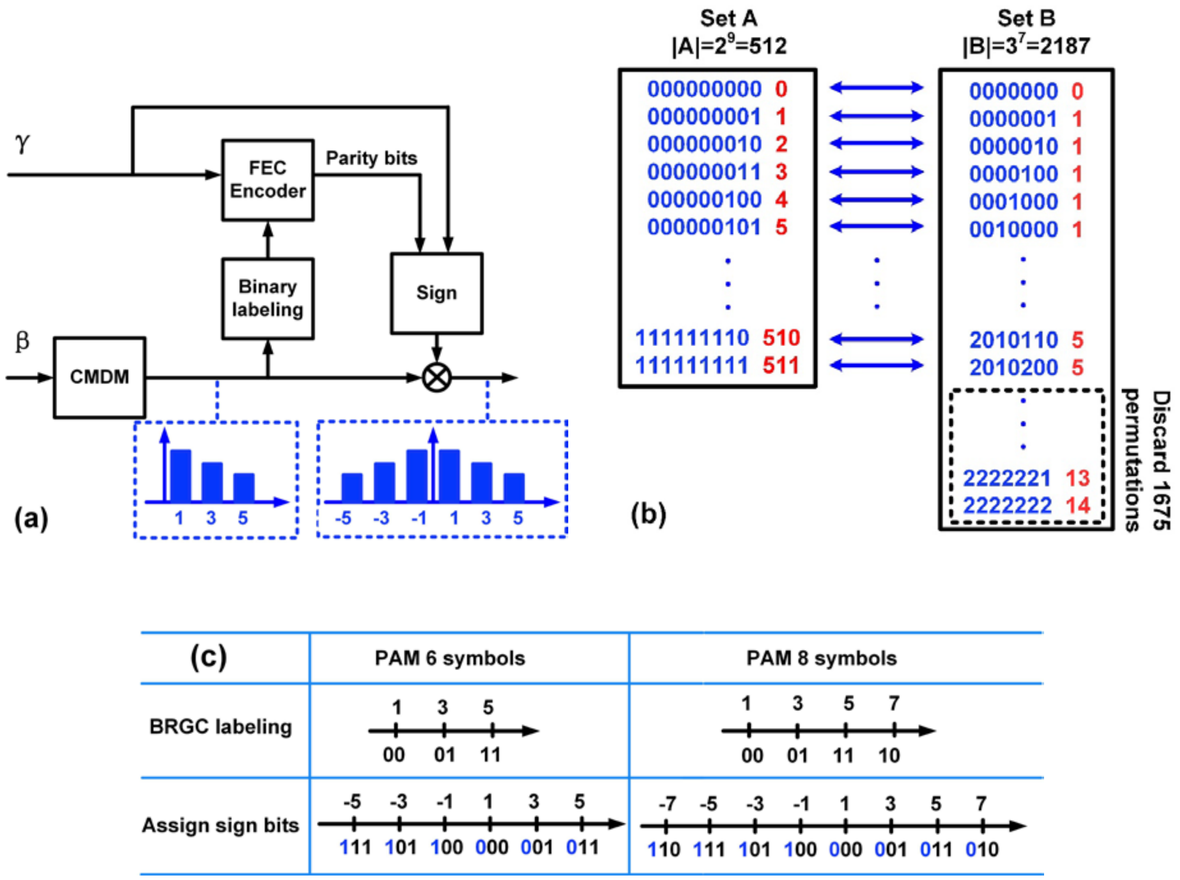

Fig. 3.1. (a) CMDM integrated within the PAS structure. (b) One-to-one mapping between the bits and symbols. (c) BRGC labeling for PAM-6 and PAM-8 symbols (sign bit marked in blue).

Figure 3.1(b) depicts the one-to-one mapping from a set A comprised of bit sequences to a set B comprised of symbol sequences. Assume for the moment that we are mapping 9-bit sequences to 7-symbol sequences, which generates positive PAM 3 symbols at an *IR* of 9/7=1.29 bits/symbol. These positive PAM 3 symbols are labeled by the binary reflected Gray code (BRGC) as illustrated in Fig. 3.1(c) and HD-encoded within the PAS structure to produce full PAM-6 symbols. Note that the cardinality of set A is chosen to be smaller than that of set B to ensure enough symbol codewords for the mapping. We also highlight that the *IR*, i.e. SE, is tunable by choosing different pairs of (k, n), where k bits are mapped to n symbols.

We construct set A and set B by first enumerating all the permutations of binary 9-bit sequences and ternary 7-trit sequences, respectively. Note that the 7-trit sequences can be easily converted to positive PAM 3 symbols. We sort the sequences in set A and set B in ascending order with respect to the sequence weight marked in red as in Fig. 3.1(b). The weight for the sequences in set A is simply the value of the 9-bit binary number, whereas the weight for the sequences in set B is the weighted sum of all trits as marked in red. The trit weights are taken as one for simplicity of explanation but are optimized to approach the optimal distribution during implementation. The symbol sequences in set B with identical weight are sorted in ascending order based on the value of the 7-trit ternary number. Since there are more sequences in set B than in set A (3^7=2187＞2^9=512), we can ensure corresponding symbol sequences for any given bit sequences. Next, we discard 1675 symbol sequences in set B possessing higher weights as boxed by the dashed rectangular so that we construct a 1-to-1 mapping between set A and B. Note that by discarding the higher weight symbol sequences, we reduce the probability of occurrence of higher energy-positive PAM-3 alphabets. This ordering-discarding operation produces symbols whose probability distribution approaches a Gaussian one, which maximizes the mutual information in AWGN channels.

Apart from resorting to the LUT-based approach, we can also generate symbol sequences online without pre-storing the 1-to-1 mapping. The idea is to index the bit sequences in set A and set B and then rely on the indexes to locate the corresponding symbol sequence or bit sequence. A natural way to index the bit sequences in set A is by converting the binary numbers to decimal numbers. To index elements in set B, we need first to know the total number of symbol sequences corresponding to a specific weight, which is expressed as

$$N(w,n,b)=\sum_{i}^{n}(-1)^{i}\binom{n}{i}\binom{w+n-1-bi}{n-1}, \tag{3.1}$$

where w is the weight, n is the number of trits in a symbol sequence, and b is the base, i.e. 3 in this case. Based on (3.1), we are aware of the numbers of symbol sequences for each weight and we can determine the corresponding weight w_0 for any given index i linked to a bit sequence. Note that the symbol sequences are sorted in increasing order at a specific weight and we can use the method in [64] to generate the symbol sequence (x_1, x_2, …, x_n) online. We detail the algorithm that generates PS-PAM-6 symbols as follows:

Step 1: We set $i=i-\sum_{w<w_0}N(w,7,3)$.

Step 2: for k = 1,

if $i > N(w_0-1, 7-k, 3)+ N(w_0, 7-k, 3)$,

set x_1 = 2, and set $i = i- N(w_0-1, 7-k, 3)- N(w_0, 7-k, 3)$;

else if $i > N(w_0, 7-k, 3)$,

set x_1 = 1, $i = i - N(w_0, 7-k, 3)$;

else set x_1 = 0.

Step 3: for k = 2, …, n,

if $i >$ $N\left(w_0-\sum_{j=1}^{k-1}x_j-1,7-k,2\right)+N\left(w_0-\sum_{j=1}^{k-1}x_j,7-k,2\right)$,

set x_k=2, and set $i=i-N\left(w_0-\sum_{j=1}^{k-1}x_j-1,7-k,2\right)-N\left(w_0-\sum_{j=1}^{k-1}x_j,7-k,2\right)$;

else if $i >$ $N\left(w_0-\sum_{j=1}^{k-1}x_j,7-k,2\right)$, set x_k=1, and set $i = i - N\left(w_0 - \sum_{j=1}^{k-1} x_j, 7-k, 2\right)$;

else set $x_k = 0$.

The demapping from symbol sequences to bit sequences at the receiver can be performed in a similar manner and is not discussed here in full detail. It is worth mentioning that the IL-based CMDM can extend to any other higher-order PS-PAM formats. Moreover, the combinatorial numbers $N(w,n,b)$ can be pre-stored in the processor memory to speed up the signal processing.

Next, we implement CMDM at various intermediate IRs beyond those available from PAM-4 and PAM-8 by selecting different pairs of (k, n). We limit the symbol block length of CMDM to no more than 10 and we measure the entropy loss versus the maximum IR as depicted in Fig. 3.2. The maximum *IR* equals *IR*+1, assuming a zero-noise channel. We also include in the figure the entropy loss at different maximum IRs for a PS-PAM-8 signal generated by CCDM at a symbol block length of 10. As shown in the figure, CMDM allows a number of intermediate maximum IRs whose EL are kept below 0.15 bits/symbol, whereas CCDM not only induces a significantly higher EL because of a much shorter symbol block length than usually required [19] but also allows much fewer intermediate maximum IRs. The inset shows the histogram of PS-PAM 8 symbols at a maximum IR of 2.625 bits/symbol.

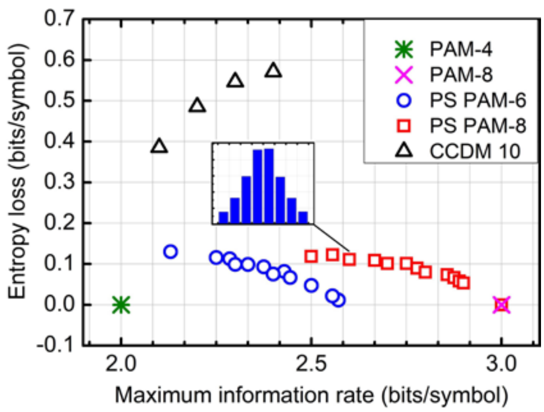

Fig. 3.2. Entropy loss versus the maximum IRs. Inset: histogram of PS-PAM 8 symbols at a maximum IR of 2.625 bits/symbol.

3.2.3. Results and discussion

Figure 3.3 depicts the schematics of the experimental setup. After generating the PS symbols, a 3-memory length symbol-pattern dependent nonlinear LUT is used to pre-distort the symbols to mitigate the system nonlinearity. Then the signal is resampled to the arbitrary waveform generator (AWG) sampling rate of 120 GSa/s for pulse shaping via a raised-cosine (RC) shaping filter. Next, a pre-emphasis filter is applied to the pulse-shaped signal to flatten the response of the transmitter RF chain. The signal is then clipped to a peak-to-average power ratio (PAPR) of 10 dB and quantized before digital-to-analog conversion. The four-channel RF signals are amplified using 4 linear amplifiers with a 3-dB bandwidth of 42 GHz and then drive a packaged four-lane InP EML TOSA that supports the QSFP-DD form factor. The optical spectrum of the 20-nm-spaced CWDM signal is captured at the TOSA output as shown in the inset of Fig. 3. After propagation over 2 km of single-mode fiber (SMF), the received CWDM signal is demultiplexed, separately detected by a 40 GHz photodiode with an integrated trans-impedance amplifier (PIN+TIA), and sampled by a 63 GHz 8-bit real-time oscilloscope (RTO) operating at 160 GSa/s. The postprocessing at the receiver is presented in the Rx DSP block in detail

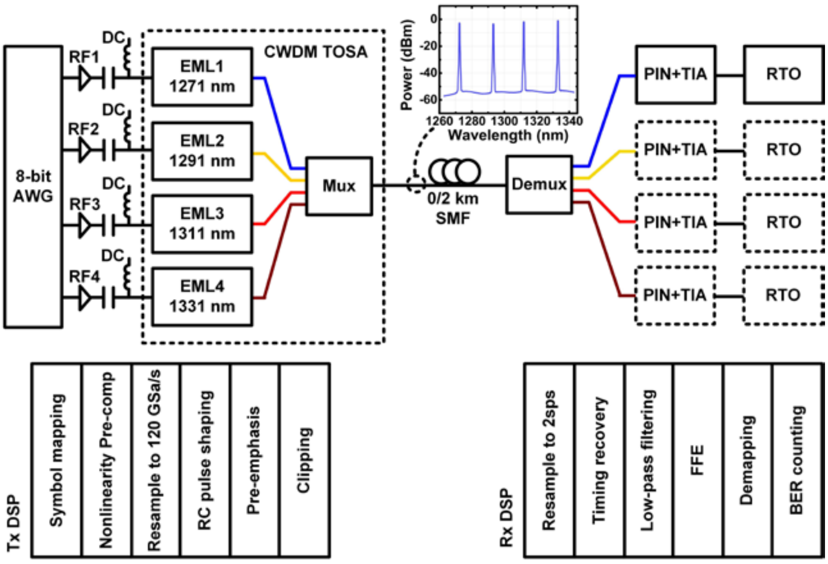

Fig. 3.3. Schematics of the experimental setup, the Tx and Rx DSP block, and the optical signal spectrum at the output of the TOSA.

including resampling, timing recovery, low-pass filtering, linear feedforward equalization (FFE), symbol-to-bit demapping and BER counting.

Within the PAS structure, the information bits per sign bit γ is calculated as $l \times c$-(l-1), where l bits are used to label each PS-PAM symbol and c is the code rate equal to 0.933 for the chosen staircase code; the information bits per positive PAM symbol β is calculated as k/n, where k bits are mapped to n symbols. Thus, the IR for full PS-PAM symbols is γ+β and the required symbol rate to reach a throughput of 200 Gbit/s per wavelength can be determined for any given IR. Fig. 3.4 shows the BER as a function of IR for the 1311 nm channel at a received optical power (ROP) of -3 dBm over 2 km of SMF. Note that the PS-PAM 6 and PS-PAM-8 signals are both generated using CMDMs at a short symbol block length of 7 assuming the LUT-based implementation. The symbol rate at each IR is set to achieve a single-lane 200 Gbit/s throughput. As can be seen from the figure, the BER increases for PS-PAM-6 signals at lower IRs because higher symbol rates are required, thereby resulting in stronger ISI due to limited channel bandwidth; the BER of PS-PAM-8 signals increases at higher IRs because of limited system SNR. Apparently, neither PAM-4 nor PAM-8 enables error-free decoding with respect to the pre-FEC BER threshold. Amongst all the *IR*s, PS-PAM-8 at an IR of 2.375 bits/symbol achieves the lowest BER that is below the FEC threshold.

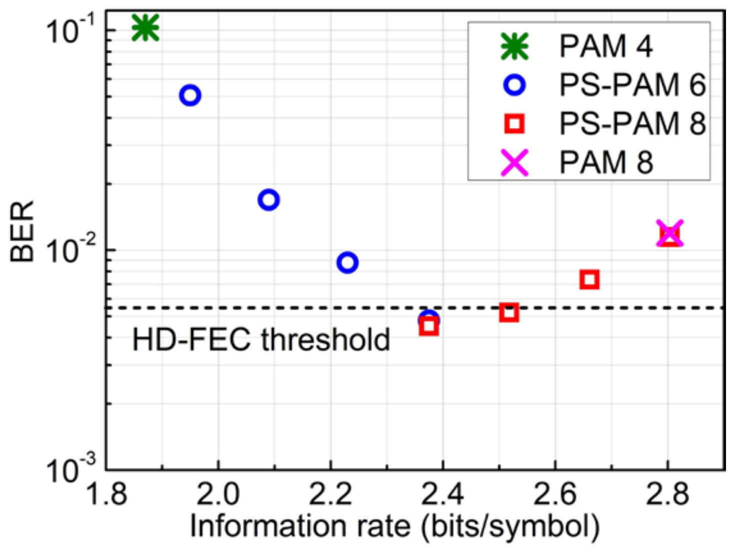

Fig. 3.4. BER vs. IR over 2 km of SMF for the 1311 nm channel.

Next, we measure the sensitivity gain of the 2.375 bits/symbol PS-PAM-8 signal relative to PAM-4 and PAM-8 signals. The BER is plotted as a function of the ROP as shown in Fig. 3.5. We also include in the figure the curve of a CCDM-generated PS-PAM-8 signal with approximately the same IR and same entropy loss using a symbol block length of 70. It can be observed in the figure that the two PS-PAM-8 curves are the ones that go below the HD-FEC threshold. We also verify that the distributions are similar with the relative entropy from the CMDM distribution with respect to the CCDM one as low as 0.0043 bit/symbol. The CCDM generated PS-PAM-8 signal produces marginal sensitivity gain compared with the one based on CMDM, however, at the cost of a much longer symbol block length.

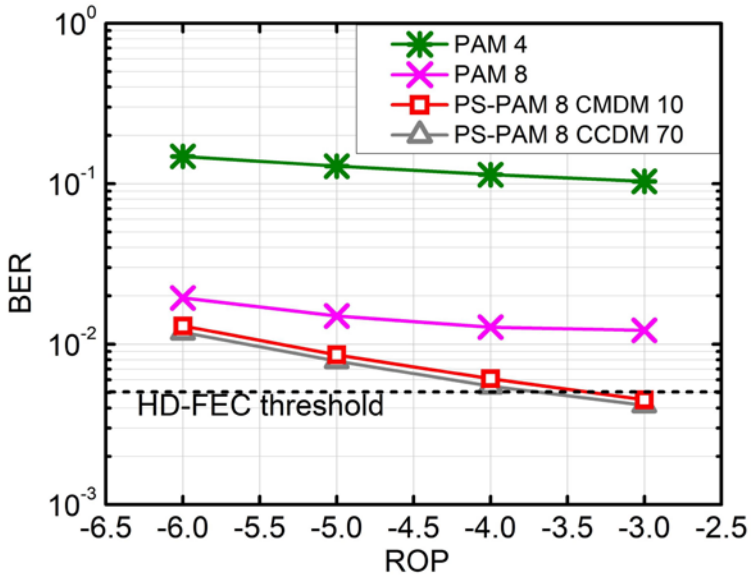

Fig. 3.5. BER vs. ROP for the PS-PAM signals, PAM-4 and PAM-8.

Then we operate the four-channel EML TOSA to transmit 2.375 bits/symbol PS-PAM-8 signal. Fig. 3.6 shows the transmission results. Each of the four TOSA channels is signaling simultaneously a net 200 Gbit/s PS-PAM-8 signal. In the figure, the average BERs are below the HD-FEC threshold, thereby ensuring the error-free decoding of an 800 Gbit/s throughput CWDM signal assuming that the four channels are encoded in an interleaved way. Note that the average BER is slightly lower after propagation over 2 km relative to at back-to-back (B2B). More specifically, the BERs of channels 1271 nm and 1291 nm decrease after propagation due to the interaction between a negative chromatic dispersion (CD) and a positive EML chirp.

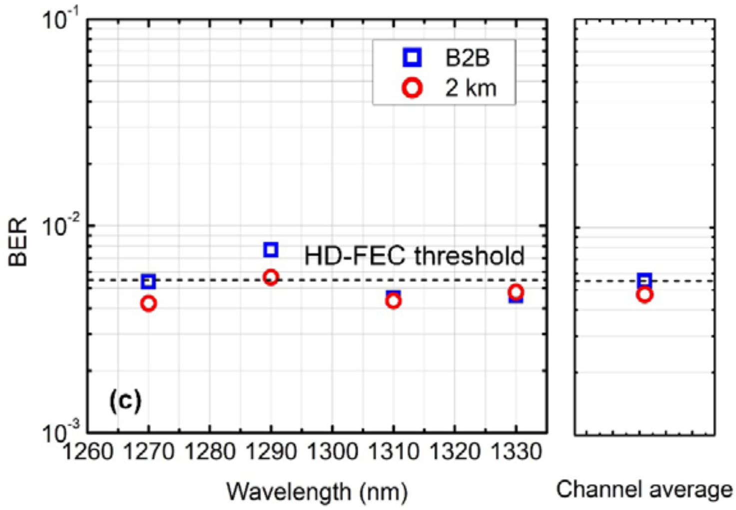

Fig. 3.6. The transmission results using the CWDM EML TOSA at B2B and over 2 km of SMF.

3.3. Input distribution optimization for practical IMDD systems

3.3.1. Introduction

Recent demonstrations of PS in short-reach IMDD systems often adopt the Maxwell-Boltzmann (MB) distribution, which is conventionally used in long-haul optical communications for achieving the highest entropy in AWGN channels. However, the AWGN approximation is not a close fit for actual IMDD systems, where the signal is also impacted by the device nonlinearity and non-AWGN noise sources including the laser flicker noise, clock jitter, and clock leakage harmonics. Thus, the MB distribution is suboptimal in practical IMDD systems, and it is desirable to optimize the input distribution based on the actual channel properties in a feasible way. Previous papers propose solutions that perform either exhaustive search [65] or numerical optimization techniques [66, 67] for the optimization of the input distribution which requires prior knowledge of an analytical system model. However, a comprehensive and accurate system model is often difficult to build and requires precise measurement of numerous system parameters that are coupled with each other.

It is known that neural networks have a strong nonlinear approximation capability and can be used to build a data-driven model that predicts the performance metrics of the system for any given input distribution. In this section, we propose a novel approach to optimizing the input distribution of practical IMDD systems using a neural network (NN) and the genetic algorithm (GA) [68]. The NN is used to predict the generalized mutual information (GMI) corresponding to a given input distribution, whereas the GA is used to search the optimal input distributions at desired spectral efficiencies (SE) using the trained NN as the fitness function. We first show numerically the effectiveness of the NNGA-algorithm in finding near-optimal input distributions that outperform the MB distribution in an IMDD system with sinusoidal nonlinearity. Next, we experimentally validate the NNGA scheme in optimizing the input distribution of a practical O-band IMDD system over 2-km of single-mode fiber (SMF) with a silicon photonic (SiP) traveling wave Mach-Zehnder modulator (TWMZM). It is found that the NNGA-optimized distribution achieves 23.5 % higher throughput relative to the MB distribution assuming an 8/9 fixed-rate low-density parity-check (LDPC) code with an NGMI threshold of 0.91 at 80 Gbaud, which corresponds to a net data rate of 197.3 Gb/s.

3.3.2. Principle of the NNGA-assisted distribution optimization

The AWGN channel model for short reach IMDD systems are often not valid due to (i) the device nonlinearity resulting from the phase shifter, the modulator, and the trans-impedance amplifier (TIA); (ii) the colored noise spectrum after equalization in a bandlimited channel; (iii) non-AWGN sources such as the laser flicker noise and the clock leakage harmonics. Fig. 3.7 depicts a schematic of the NNGA-assisted distribution optimization scheme for a non-AWGN channel.

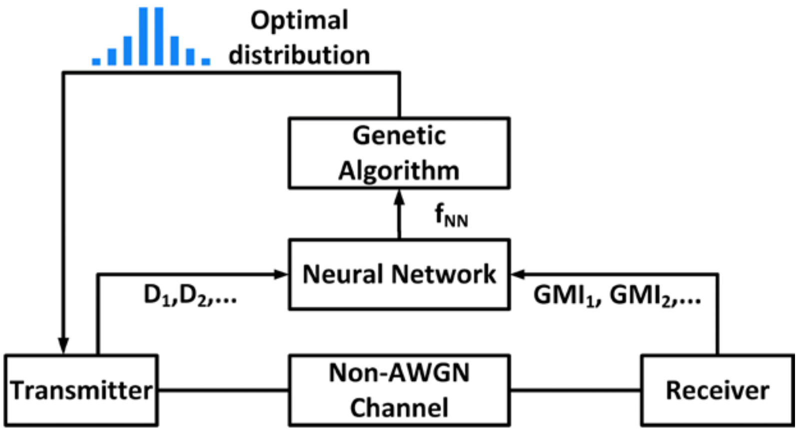

Fig. 3.7. Schematic of the distribution optimization using NNGA.

In this scheme, we use a neural network (NN) to approximate the nonlinear multivariable function that maps the input distribution D at the transmitter to the GMI at the receiver, which is chosen as the performance metric in the PAS scheme [58]. Note that symbols of different input distributions D_1, D_2… are sent at the transmitter to probe the channel so that the NN can effectively learn to predict the system performance for any given distributions. The trained NN is seen as a multivariable function noted as f_{NN} and is fed to a GA module as a second stage which optimizes the input distribution at desired SEs, i.e. entropies. Note that this combined NNGA scheme is also applicable to the distribution optimization of long-reach channels with low dispersion.

Here we send PS-PAM-8 signals in both the numerical and experimental IMDD systems. As the distribution of PS-PAM-8 symbols is symmetric due to the PAS scheme, we reserve only the probability mass function (PMF) of the positive half PS-PAM-4 symbols to reduce the number of inputs to the NN, thereby reducing the complexity of the network. The PMF is formulated as $D = [P_1\ P_2\ P_3\ P_4]$ and each PMF is created by first generating a 1×4 vector of uniformly distributed random numbers within [0,1], whose sum is normalized to 1 for a valid PMF. Constant composition distribution matching (CCDM) is used to generate symbols following the desired PMFs [19].

Fig. 3.8 shows a schematic of the optimized NN with two hidden layers that contain 16 and 32 hidden units, respectively. The PMF is taken as the input of the NN, whereas the GMI is taken as the output of the NN. We use the rectified linear unit (ReLU) function as the activation function in the hidden layers and minimize the mean squared error (MSE) between the NN output and the GMI from the training set. We use a mini-batch size of 128 and the Adam algorithm to optimize the NN weights and biases. The training set, validation set, and testing set contain 1000, 250, and 250 PMF-GMI examples, respectively. The NN is trained over 1000 epochs. We note that it is important to minimize the error on the examples of validation set so that the GA can effectively approach the optimal input distribution. Thus, the model parameters with the lowest validation error are chosen to predict the GMI.

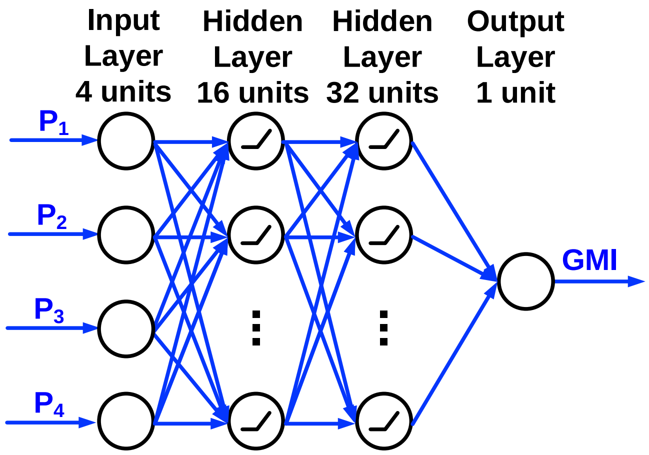

Fig. 3.8. Schematic of the NN with two hidden layers.

Fig.3.9 plots a toy model of an IMDD system that we use to evaluate the effectiveness of the NNGA algorithm. The sinusoidal function introduces a certain level of nonlinearity controlled by k, which is a parameter within [0,1] that controls the swing of a normalized signal x. The maximum swing, i.e. from $-\pi/2$ to $\pi/2$ is obtained at k=1. A 20 dB AWGN source is cascaded after the nonlinear module to simulate the overall system noise.

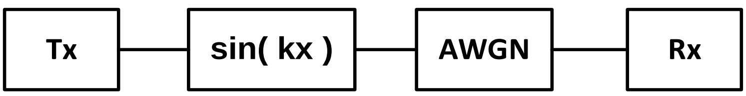

Fig. 3.9. A simplified model for short-reach IMDD systems.

Note that this simplified model is used to assess the effectiveness of the NNGA scheme in order to optimize the distribution of a short-reach IMDD system with nonlinearity. In actual systems, the material nonlinearity of the phase shifter, the saturation of the TIA also contribute to the overall system nonlinearity. After training, the NN is seen as a multivariable function f_{NN}, and finding the PMF that maximizes the function output, i.e. GMI at a certain entropy is equivalent to an optimization problem formulated as follows

$$\begin{aligned}
&\underset{D}{\textit{Minimize}} \;\; -f_{NN}(D) \\
&\textit{subject to} \; \sum P_i = 1, \\
&\qquad\qquad\quad \sum -P_i \log_2(P_i) = \textit{Entropy} - 1, \\
&\qquad\qquad\quad 0 \le P_i \le 1, \\
&\textit{where} \;\; i = 1,2,3,4 \;\; \textit{for all constraints}.
\end{aligned}$$

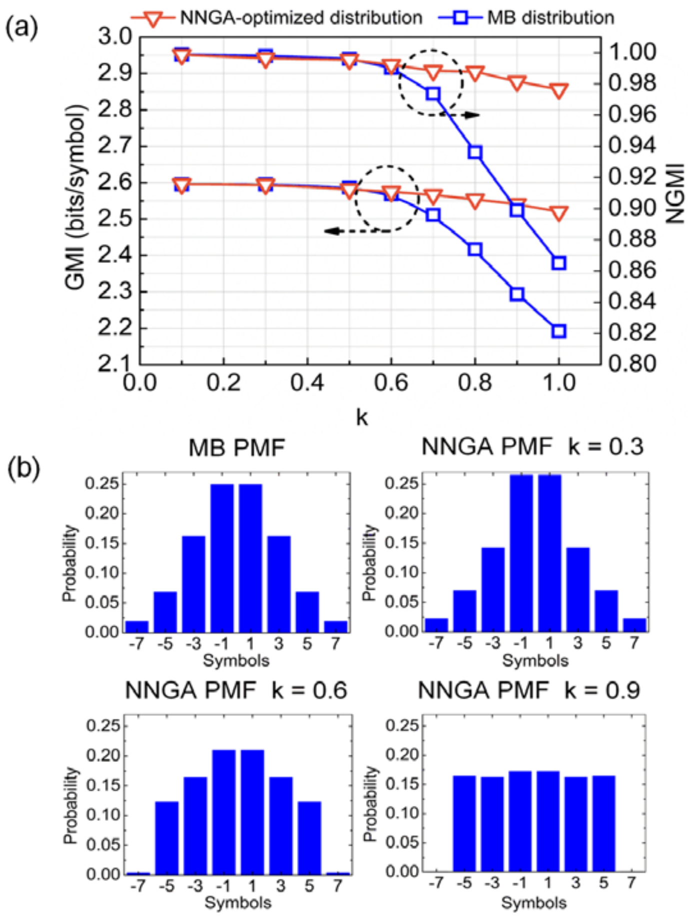

Fig. 3.10. (a) GMI and NGMI as a function of k for the MB and NNGA-optimized distributions. (b) PMF histograms of the MB distribution and NNGA-optimized distributions at different k.

Since this is a nonconvex nonlinear minimization problem, we use the genetic algorithm to search for approximated solutions by setting $-f_{NN}$ as the fitness function and performing mutation, crossover, and selection of the encoded input distributions. Fig. 3.10 (a) plots the GMI and NGMI as a function of k for both the MB and the NNGA-optimized distributions at entropy of 2.6.

The figure shows that the GMI of the MB distribution decreases sharply when k is greater than 0.6, whereas the GMI of the NNGA-optimized distribution decreases in a much slower rate. The NGMIs also show a similar trend for the MB and the NNGA-optimized distributions. As rate-adaptive FECs are costly, a fixed-rate FEC combined with PS is more desirable in practical systems to enable the rate adaptation. It is observed from the figure that the NNGA-optimized distribution with a higher NGMI indicates a higher bound of the allowed code rate of practical FECs when k is greater than 0.6. Fig. 3.10 (b) shows the corresponding PMF histograms of the MB distribution and the NNGA-optimized distribution at k of 0.3, 0.6, 0.9 at entropy of 2.6. It is observed that as k increases, i.e. with stronger nonlinear effect, the NNGA scheme determines that the probability of the outermost symbol level needs to be reduced to mitigate the impact of the MZM nonlinearity.

3.3.3. Experimental setup and results

We experimentally evaluate the performance of the NNGA-optimized shaping in an IMDD system in the O-band. Fig. 3.11 depicts the experimental setup. The carrier at 1302 nm is coupled into a SiP-TWMZM with a 3-dB E-O bandwidth of 45 GHz. The TWMZM modulates the carrier with an amplified RF signal generated by a 120 GSa/s arbitrary waveform generator (AWG). After propagation over 2 km of SMF, the signal is detected by a photodiode (PD)+TIA with a 3-dB bandwidth of 45 GHz and sampled by a 62 GHz real-time oscilloscope (RTO) for the post-processing. The transmitter and receiver DSP are also shown below the setup in the figure.

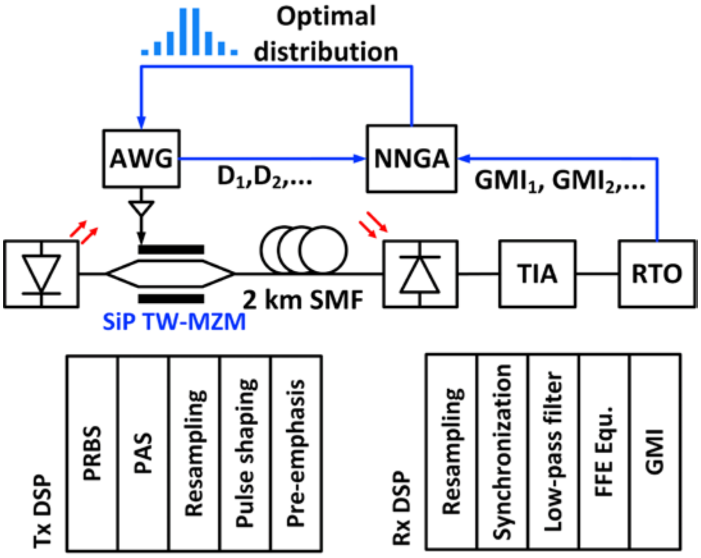

Fig. 3.11. Experimental setup and DSP blocks.

The NN is trained following the procedure as described earlier. We transmit 80 Gbaud PS-PAM 8 signals to assess the performance of the NNGA-optimized shaping in this setup. Fig. 3.12 shows the PMF histograms and eye diagrams of the MB distribution and NNGA-optimized distribution, respectively, at entropy of 2.6. For the MB distribution, it is seen that the eye-openings close to the outermost levels are almost indiscernible due to the system nonlinearity. By contrast, the NNGA distribution has much more distinguishable eye openings and thus a 1.2-bits/symbol higher GMI.

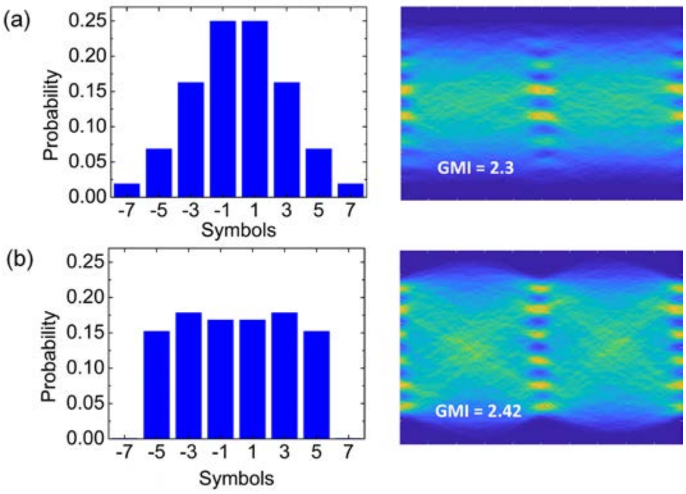

Fig. 3.12. PMF histograms and eye diagrams of (a) the MB distribution, and (b) the NNGA distribution at entropy of 2.6.

Fig. 3.13 plots the GMI and NGMI versus a varied entropy for both the MB distribution and NNGA-optimized distribution. The figure shows that the NNGA-optimized distribution leads to a higher GMI than the MB distribution at the same NGMI, i.e. the code rate of an ideal FEC. Assuming a practical 8/9 LDPC code with an NGMI threshold of 0.91 [69], the NNGA-optimized distribution allows a 0.47 bit/symbol higher information rate. This translates to 23.5 % higher throughput at 80 Gbaud and corresponds to a net data rate of 197.3 Gb/s.

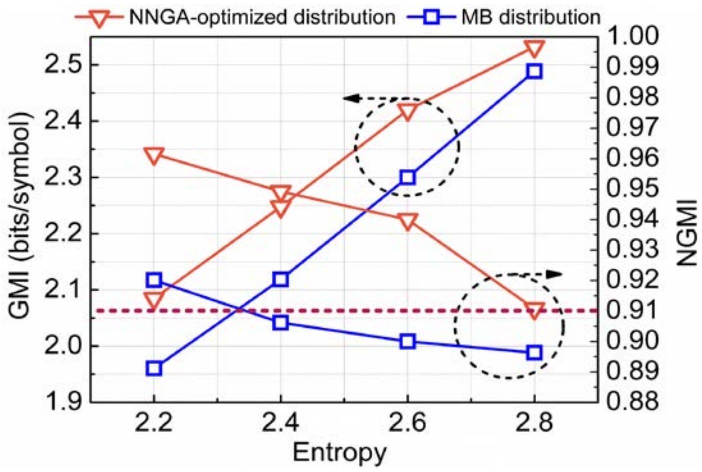

Fig. 3.13. GMI and NGMI as a function of the entropy.

3.4. Conclusions

We verified both numerically and experimentally that probabilistic shaping is an effective scheme to achieve 200 Gb/s throughput per lane. We propose two techniques to address the practical challenges that the potential implementation of PS faces in IMDD systems, i.e. (a) realize the shaping and deshaping using a short block length distribution matcher, (b) identify the optimal input distribution in practical IMDD systems. We conclude this chapter with a few remarks on the potential impact of these two techniques:

- The integration of CMDM into PAS enables the generation of PS-PAM signals with a short block length and allows almost continuous tuning of the IRs beyond those available from standard PAM formats. Moreover, we show the distribution is tunable by changing the weight assigned to the symbols, which can provide additional coding gain when compared to the MB distribution for non-AWGN IMDD systems. We also present the two different ways to implement CMDM, i.e. the LUT-based method and the IL-based method. At a relatively shorter block length, the LUT-based method is more suitable as a small memory is required, whereas at a longer block length, it is preferable to generate the shaped symbols online using the IL-based method to avoid the need for a large memory footprint. By using the CMDM-based PS, we report, to our knowledge, a first net 800 Gbit/s IMDD system over 2 km using a CWDM TOSA in the O-band.

- We also show the effectiveness of the NNGA based method in approaching the optimal input distribution for practical IMDD systems at a given spectral efficiency. The NN has only two hidden layers, which is well-suited for deployments in practical IMDD modules requiring a low power consumption. We show that in an O-band IMDD setup, the NNGA-optimized distribution achieves 23.5% higher throughput compared with the MB distribution over 2 km assuming an 8/9 LDPC code. We note that the proposed NNGA scheme can also be extended for other transmission systems including the long-haul DCO systems with the NN and GA modified accordingly to improve the modeling accuracy and the searching efficiency.

4 Self-coherent single-sideband direct detection systems

4.1. Overview

As discussed in Chapter 1, DSP is available to enhance the performance of optical communication systems as the processing speed of CMOS integrated circuits catches up with the data rate of optical interfaces [70]. For phase-diverse detection schemes such as the homodyne coherent detection, the signal field can be fully reconstructed at the receiver and mapped to the electrical baseband such that we can digitally compensate for various link impairments including CD and PMD. Due to this, coherent detection systems possess a greater throughput-distance product compared to IMDD systems and are substituting IMDD systems for the data center interconnect from 40 km to 120 km as the capacity demand grows at an exponential speed. Nevertheless, DCO systems are still expensive for optical links below 40 km, where the dense deployment of optical modules on rack switches is required and a tight limit on power dissipation is imposed.

Though IMDD systems are dominant for short-reach connections below 10 km in the data center network, their throughput is constrained by (a) one-dimension modulation, i.e. intensity modulation and (b) retrieval of only the field amplitude with all the phase information lost. As a result, the electrical spectrum of the received signal shows multiple notches due to the power fading effect as detailed in Chapter 2, which limits the attainable reach of IMDD systems since the throughput is significantly degraded at a longer transmission distance beyond 10 km.

We show in chapter 3 that at a distance less than 10 km where the link impairment is marginal, probabilistic shaping is an effective technique to improve the system throughput by achieving an optimal trade-off between the system bandwidth and the system SNR. At a reach from 10 km to 40 km, we can greatly improve the throughput of IMDD systems by replacing the intensity-modulated signal with a field modulated signal having a co-propagating CW tone. More specifically, the CW-tone is located outside of the signal spectrum with a minimal guard band configured to maintain high signal SE. This type of signal is referred to as a self-coherent (SC) single-sideband (SSB) signal. The SC-SSB-DD system has a distinct advantage compared to the IMDD system: using the same single-ended DD receiver, the incident optical signal beats with the CW tone, giving rise to a linear term from which the signal field can be reconstructed. A DD system with such a signaling scheme can digitally compensate for the channel impairments similar to DCO systems at the receiver. Thus, the SC-SSB DD system as an advanced DD system can achieve higher throughput at a longer transmission reach.

Numerous papers can be found in the literature proposing a variety of approaches to remove the SSBI as detailed in Chapter 2, which is a nonlinear interference that could be present within the signal spectrum and degrade the system performance. Apart from this, another major problem is to generate wideband SC-SSB signals with an image band that is effectively suppressed without significantly increasing the cost and power consumption of the system [71, 72]. For this, it is desirable to use only one DAC channel, since more DAC channels in the transmitter subsystem increase the hardware complexity and power consumption, e.g. additional driver amplifiers and power sources, which makes it more challenging to realize a compact low-power optical module. In this chapter, we describe two different approaches to address this issue with experimental results showing up to 800 Gb/s system throughputs. In addition, we present a polarization multiplexing scheme for SC-SSB-DD systems to further improve the throughput per wavelength. We show experimentally that a low complexity DD receiver can detect beyond 300G net data rate dual-pol SC-SSB signals.

4.2. SC-SSB signal transmitter based on a quadrature hybrid

4.2.1. Introduction

A conventional way to generate SC-SSB signals requires two DAC channels that provide the in-phase and quadrature signals, respectively. The CW tone can be generated by either shifting the bias of the modulator from the null point or split the optical carrier into another branch, which recombines with the modulated carrier part at the output of the transmitter. An alternative approach that attracts extensive interest in recent years uses a band-rejection filter to rejects a sideband of a real-valued double-sideband (DSB) signal, thus enabling the generation of SC-SSB signal using one DAC channel. This generation scheme creates a vestigial sideband signal (VSB) [73] due to the limited band rejection ratio of band-rejection filters. A typical VSB system is depicted in Fig. 4.1.

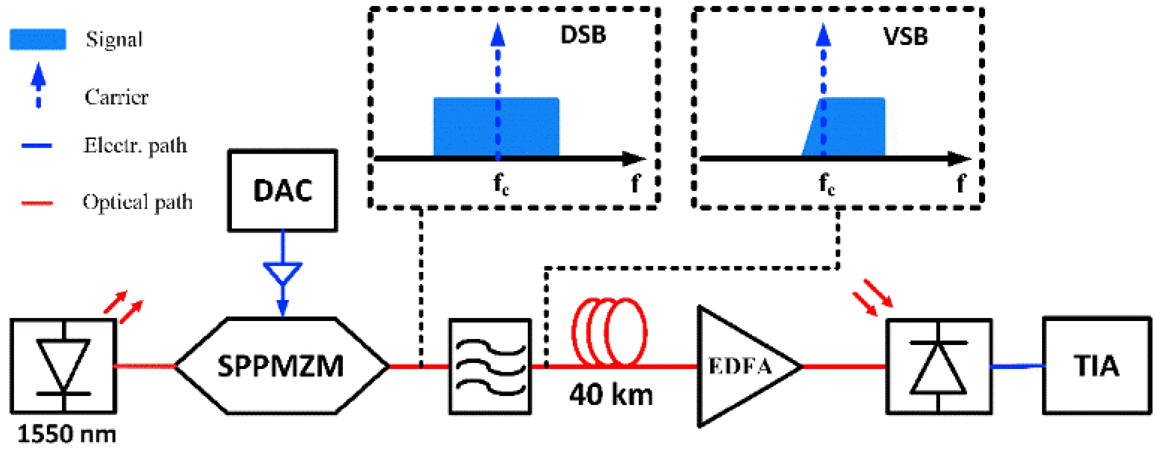

Fig. 4.1. Schematic of a VSB system and the optical signal spectrum.

In the figure, a single DAC channel drives a series push-pull Mach-Zehnder modulator (SPPMZM) biased at the intensity quadrature to modulate a real-valued DSB signal onto the optical carrier. The DSB signal is transformed into a VSB signal by optical filtering and can be reconstructed after detection by different means including the Kramers-Kronig (KK) algorithm [45, 46, 74, 75]. However, this scheme has three problems:

(a) This scheme requires an optical filter with a steep rejection slope, which is both demanding and costly to realize in current optical filter technologies. A slow rejection slope results in a strong residual signal sideband which results in power fading that degrades the system performance.

(b) The high insertion loss of the optical filter (normally around 5 dB) entails the use of EDFAs to ensure enough received optical power, which increases the power consumption of the system.

(c) A third problem is the laser wavelength drift due to temperature change or laser aging. Thus, without precise wavelength management, the wavelength misalignment between the laser and filter can lead to either over suppression of the LO tone or ineffective rejection of the signal image band. However, the need for wavelength control requires thermoelectric cooling systems which can significantly increase the power consumption of the system. Otherwise, uncooled lasers can be used in CWDM systems with a wide spacing between ajacent wavelengths.

It is known that dual-drive MZMs (DDMZM) biased at the intensity quadrature can generate SSB signals when driven by a pair of Hilbert transform signals [76, 77]. Alongside the generated SSB signal, this transmitter scheme also produces a CW tone because of the bias at the quadrature point. Instead of using two separate DAC channels to provide the in-phase and quadrature signals, we can use a wideband quadrature hybrid (WQH) to convert a single RF signal from one DAC channel into a pair of Hilbert transform signals. As a passive device, WQH does not incur additional power consumption and thus is well-suited for the data center application with a stringent power consumption constraint. Moreover, this transmitter configuration allows for SC-SSB signals with adequate signal power which is favorable for amplifier-free transmission over 40-km in the C-band. The challenge with this signal generation scheme, however, is to mitigate the modulator nonlinearity and maximize the system capacity under a colored noise spectrum and a bandwidth limit of this WQH.

In the first section of this chapter, we describe a C-band SC-SSB DD system having beyond 100 Gb/s throughput over 40-km and 60-km of reach enabled by a wideband SC-SSB transmitter consisting of a quadrature hybrid and a DDMZM [78]. We analyze the performance impact of the modulator nonlinearity and discuss different mitigating approaches including a symbol-pattern-dependent nonlinear lookup table that pre-distorts the transmitted symbols. The SC-SSB signal is detected by a single-ended PD and recovered by the KK algorithm for the post-CD compensation in the receiver DSP. The SC-SSB DD system based on this SSB generation scheme removes the need for an optical amplifier due to a strong CW-tone, requiring only a single DAC channel, an MZM, a PD+TIA, and a single ADC. We discuss the results of a parametric study where the impact of critical system parameters are evaluated including the regenerated DC component of the photocurrent, the driving voltage, and the launch power. Next, we characterize the power sensitivity improvement by performing nonlinearity pre-compensation and SSBI mitigation. We experimentally demonstrate the transmission of single-wavelength 155.14 Gb/s and 104.67 Gb/s SSB-PAM-4 signals over 40-km and 60-km of SSMF below the HD-FEC threshold of 3.8×10^{-3}, respectively. Due to the colored channel SNR within a bandwidth of 40 GHz limited by the WQH, we approach the capacity limit of our set-up by transmitting probabilistically shaped multi-subcarrier (MSC) signals. 175 Gb/s throughput is achieved over 40-km of SSMF assuming a practical SD-FEC having an NGMI threshold of 0.88. We also note that the proposed scheme is cost- and power-efficient in the C-band at 100 Gb/s throughput using DD and could be an attractive candidate for the data center interconnect below 40 km of reach.

4.2.2. Source of performance degradation

We analyze the main sources of degradation for the SC-SSB DD system using the proposed SC-SSB transmitter and discuss suitable approaches to mitigating these performance degradations. Fig. 4.2 is a schematic of the SSB transmitter. A real-valued signal is generated by a DAC channel, linearly amplified, and then sent to the input of a WQH, which is denoted as $\sqrt{2}s$ in the figure. The WQH splits the signal into two portions with equal power and creates a relative wideband phase shift of 90^o between the two signal portions within an electrical bandwidth of f_S. For analysis simplicity, we ignore the absolute phase delay caused by the WQH and denote the generated pair of Hilbert transform signals as $s, \hat{s}$. The signals $s, \hat{s}$ drive the DDMZM biased at intensity quadrature to imprint an SSB signal onto the optical carrier. The field of the incident optical carrier is expressed as $E_c e^{j\omega t}$, where E_c is the carrier amplitude, ω is the angular frequency.

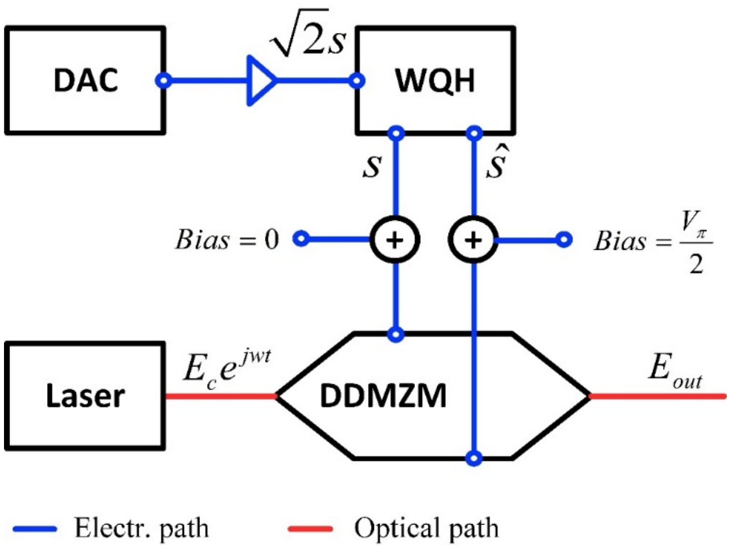

Fig. 4.2. Schematic of the SSB transmitter.

The output electric field from the modulator is expressed as:

$$E_{out} = \frac{1}{\sqrt{2}} E_c e^{jwt} \left(e^{j\frac{\pi}{V_\pi}s} + je^{j\frac{\pi}{V_\pi}\hat{s}} \right), \tag{4.1}$$

where V_π is the half-wave voltage of the modulator. Based on the Taylor series of e^x, (4.1) can be expanded as

$$\frac{1}{\sqrt{2}}E_c e^{jwt}\left(\begin{array}{l}\left(1+j\frac{\pi}{V_\pi}s-\frac{\pi^2}{2V_\pi^2}s^2-j\frac{\pi^3}{6V_\pi^3}s^3+\cdots\right)\\+j\left(1+j\frac{\pi}{V_\pi}\hat{s}-\frac{\pi^2}{2V_\pi^2}\hat{s}^2-j\frac{\pi^3}{6V_\pi^3}\hat{s}^3+\cdots\right)\end{array}\right)$$
$$=\frac{1}{\sqrt{2}}E_c e^{jwt}\left(1+j+j\frac{\pi}{V_\pi}\left(s+j\hat{s}\right)-\frac{\pi^2}{2V_\pi^2}\left(s^2+j\hat{s}^2\right)+\cdots\right). \tag{4.2}$$

Assume that the system bandwidth is mainly limited by the transmitter which is usually the case due to the current DAC technologies and we apply a pre-emphasis filter to flatten the transmitter response in order to alleviate the impact of ISI. By setting the term $E_c e^{j\omega t}/\sqrt{2}$ as one for simplicity, we can express the signal after propagation as

$$1+j+j\frac{\pi}{V_\pi}\left(s+j\hat{s}\right)\otimes h_{CD}-\frac{\pi^2}{2V_\pi^2}\left(s^2+j\hat{s}^2\right)\otimes h_{CD}+\cdots, \tag{4.3}$$

where h_{CD} is the transfer function of CD.

Note that the high order nonlinear terms are complex-valued DSB signals, thus giving rise to a faded power spectrum upon direct detection. Though it is possible to digitally alleviate the impact of these nonlinear terms at the receiver, we cannot fully linearize the signal since the field of these DSB nonlinear terms cannot be fully reconstructed at the receiver. In short-reach data center communications which faces a tight power constraint, it is desirable to implement a simple nonlinear LUT to pre-distort the transmitted symbols as opposed to resorting to high complexity Volterra equalizers. Moreover, we can complement this with appropriate attenuation of the RF signal power, e.g. using variable RF attenuators or adjusting the gain of the driver amplifier, such that the high-order nonlinear terms become negligible compared to the first-order linear term. We stress that the attenuation should be adjusted carefully. Otherwise, the modulation depth will be too small such that the system performance will be severely degraded by the receiver noise from the PD and the ADC.

After square-law detection, the linearly approximated signal is expressed as

$$\begin{aligned}&\left|1+j+j\frac{\pi}{V_\pi}\left(s+j\hat{s}\right)\otimes h_{\mathrm{CD}}\right|^2\\&=2+2\,\mathrm{Re}\left(\frac{\sqrt{2}\pi}{V_\pi}\left(\left(s+j\hat{s}\right)\exp\left(j\frac{\pi}{4}\right)\right)\otimes h_{\mathrm{CD}}\right)\\&+\frac{\pi^2}{V_\pi^2}\left|\left(s+j\hat{s}\right)\exp\left(j\frac{\pi}{4}\right)\otimes h\right|^2.\end{aligned} \tag{4.4}$$

Eq. (4.4) can be rewritten and regarded as the square-law expansion of a signal expressed below

$$\left|\sqrt{2}+\exp\left(j\frac{\pi}{4}\right)\frac{\pi}{V_\pi}\left(s+j\hat{s}\right)\otimes h_{\mathrm{CD}}\right|^2, \tag{4.5}$$

which contains a real-valued DC term $\sqrt{2}$ and an SSB signal with a constant phase shift of $\exp\left(j\pi/4\right)$, which is removed during the linear equalization. Since a PD+TIA is used in our setup to achieve the best sensitivity possible without optical amplifiers, the DC component of the photocurrent is blocked and therefore not sampled by the ADC. Thus, the DC component needs to be regenerated in the postprocessing DSP if the KK algorithm is used to reconstruct the field of the signal. Alternatively, the SSBI can be ignored if the signal-carrier beating term is significantly stronger such that a simple Hilbert-transform operation suffice to reconstruct the field of the signal.

In short-reach DD systems, the SNR is often colored with a lower SNR at higher frequencies due to sources including the equalization-enhanced noise, and the frequency-dependent effective number of bits (ENOB) of the DAC and ADC because of timing jitter. In our system, the response of the WQH also affects the SNR at higher frequencies. Note that as the frequency increases, the relative phase shift of the WQH tends to deviate from 90$^{\mathrm{o}}$ and the amplitudes of the two outputs become more imbalanced. This incurs stronger image signal components at higher frequencies that destruct the ideal SSB form of the signal and reduce the signal SNR at higher frequencies. Thus, to approach the capacity limit of the system, we can use muti-subcarrier (MSC) signaling and load each subcarrier with appropriately optimized entropy based on probabilistic shaping (PS) to best exploit the channel margin [79].

4.2.3. Experimental setup and DSP deck

Fig. 4.3 shows the experimental setup and the DSP deck. As seen in the figure, a PRBS sequence is first generated and Gray-mapped to PAM-4 symbols. Then a symbol pattern-dependent nonlinear look-up-table (NLLUT) is used to pre-distort the symbols to mitigate the impact of the nonlinearity from sources including the modulator, driver amplifier, and TIA. The symbols are then resampled to the DAC sampling rate of 120 GSa/s for pulse shaping by use of a raised-cosine (RC) pulse shaping filter with a roll-off factor of 0.01. Then a pre-emphasis filter is applied to the signal to flatten the RF channel including the DAC and the linear amplifier. We clip the signal to a peak-to-average power ratio (PAPR) around 10 dB that is tuned accordingly at different symbol rates. Finally, the signal is sent to the memory of an 8-bit DAC for the RF signal generation.

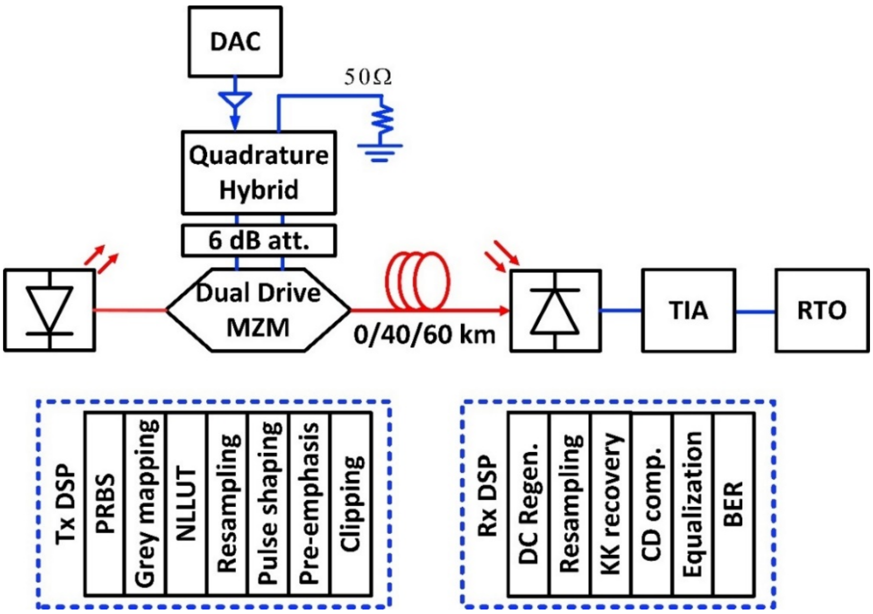

Fig. 4.3. Experimental setup and the DSP decks of the transmitter and receiver.

The signal is amplified by a linear amplifier with a 3-dB bandwidth of 60 GHz and fed to a WQH that generates a pair of Hilbert transform signals. The WQH has a functioning frequency range from 2 to 40 GHz. The amplitudes of the outputs are more imbalanced and the relative phase shift between the outputs deviates from 90° near the edge of this frequency range. RF attenuators are cascaded after the WQH outputs to reduce the swing of the RF signal in order to mitigate the modulator nonlinearity. Since variable RF attenuators are not available, we use discrete attenuation values, i.e. 3-dB, 6-dB, and 9-dB, and measure the system performance. 6-dB attenuators are found to be the optimal trade-off between the modulator nonlinearity mitigation and the modulation depth. The attenuated pair of signals drive the DDMZM with a 3-dB bandwidth of 37 GHz to modulate a carrier produced from an external cavity laser which operates at 1550.22 nm.

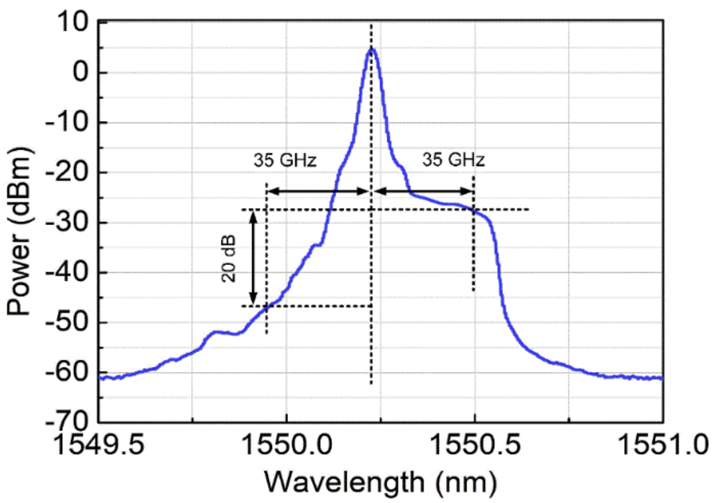

Fig. 4.4. Optical spectrum of the signal measured at the output of the DDMZM.

Fig. 4.4 is the measured optical spectrum of an 80 Gbaud PAM-4 signal at a roll-off factor of 0.01 out of the DDMZM by use of an optical spectrum analyzer (OSA) with a resolution of 0.05 nm. As indicated in the figure, there is a 20-dB rejection ratio at a frequency gap of 35 GHz from the optical carrier, indicating a negligible image sideband signal. Note that in the figure the rejection ratio is lower for frequency components closer to the carrier which is attributable to the limited resolution of the OSA.

After propagation over fiber lengths of 0, 40, and 60-km, the optical signal is directly detected by a PD+TIA with a 3-dB bandwidth of 40 GHz and sampled by an 8-bit 160 GSa/s ADC with a brick-wall low-pass filter response of 62 GHz. In the Rx postprocessing DSP, the DC term blocked by the TIA is regenerated such that the signal can be linearized using the KK algorithm after digitally resampled to 3 samples per symbol. Then the signal samples are resampled to 2 samples per symbol for the subsequent CD compensation and linear equalization using a feedforward (FFE) equalizer. Finally, the symbols are decoded and the BER is computed.

4.2.4. Results and discussion

In this subsection, we present the experimental results by first discussing the performance impact of the critical system parameters. Fig. 4.5 plots the BER as a function of the regenerated DC voltage for an 80 Gbaud and a 56 Gbaud SSB PAM-4 signals transmitted over 40-km at a received optical power of -3 dBm. The figure shows a similar

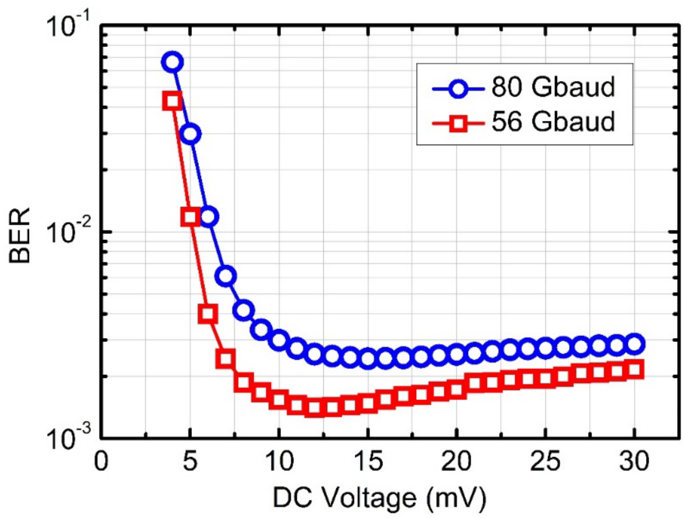

Fig. 4.5. BER versus the change of the regenerated DC term for an 80 Gbaud SSB PAM-4 signal transmitted over 40-km SMF.

trend at both symbol rates. As the added DC voltage increases, the BER decreases till reaching a minimum point before turning to a gentle increase with a mild BER variation within 1×10^{-3} for the DC voltage less than 25 mV. We regard the DC voltages that minimize the BER as a proper estimate of the filtered DC component by the AC-coupled PD and further estimate the carrier-to-signal power ratio (CSPR) based on two different ways described in [80, 81]. The two methods provide very similar CSPR estimates of 18.5 and 21 dB for the 56 Gbaud and 80 Gbaud signal, respectively. Hence, the SSBI is marginal compared to the carrier-signal beating term at both symbol rates, which explains this mild increase of BER after the DC voltage surpasses the value that minimizes the BER.

Next, we change the number of active DAC quantization levels to study how the power of the driving signal impacts the performance of the system with the 6 dB attenuators at the transmitter. To keep the impact of the varied quantization noise low, the number of quantization levels is merely changed from 8 bits to 7.5 bit corresponding to 256 and 180, respectively. Fig. 4.6 plots BER as a function of the measured root-mean square of the driving voltage V_{RMS} for an 80 Gbaud SSB PAM-4 signal transmitted over 40-km. It is seen in figure that a 2.5×10^{-2} BER decrease is observed even the number of active quantization level is reduced by merely 0.2 bits. This indicates that at this level of driving voltage, the mitigation of the modulator nonlinearity is less important compared to increasing the voltage swing at the receiver. Thus, it is more suitable to use the full quantization levels to achieve a higher modulation depth so that a stronger carrier-signal beating term can be obtained at the receiver. This increases the signal SNR considering the presence of Rx noise sources including the thermal noise of the PD+TIA, and the distortion and quantization noise of the ADC.

We also measure the BER change with the launch power by means of a variable optical attenuator (VOA) with the results shown in Fig. 4.7 for an 80 Gbaud SSB PAM-4 signal transmitted over 40-km. In the figure, the BER decreases with increasing launch power. The explanation is that the fiber nonlinearity is marginal for a 40-km of reach and a higher launch power leads to a higher received optical power (ROP) when no EDFAs are used. Note that the BER does not show a kink point in the figure since the ROP is not high enough to induce severe saturation of the TIA.

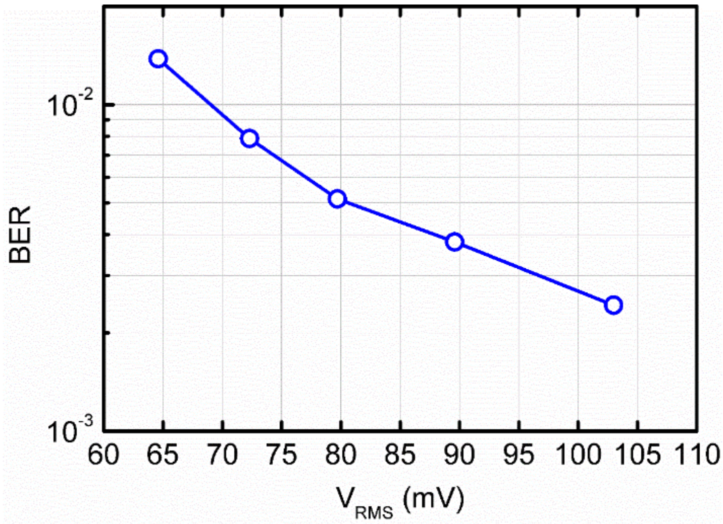

Fig. 4.6. BER as a function of VRMS for an 80 Gbaud PAM-4 signal transmitted over 40-km SMF.

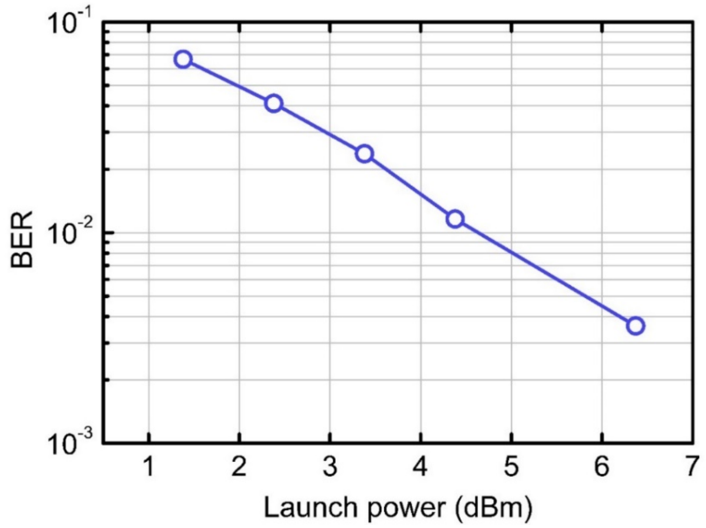

Fig. 4.7. BER versus launch power for an 80 Gbaud SSB PAM-4 signal transmitted over 40-km SMF.

Next, we experimentally study the sensitivity impact of the system nonlinearity and demonstrate transmission of beyond 100 Gbit/s throughput SSB PAM-4 signals over 40- and 60-km of SMF. Fig. 4.8 plots the BER as a function of the ROP for a 56 GBaud and an 83 GBaud SSB PAM-4 signal over 40-km SMF at an ROP of -3.12 dBm, respectively. Note that the symbol rate of 56 Gbaud is chosen to attain a throughput of 100 Gb/s considering the 7% HD-FEC and the 5% Optical Transport Network (OTN) overhead; whereas 83

Gbaud symbol rate is found to reach the maximum throughput below the HD-FEC threshold of 3.8×10^{-3}. As the CSPRs are high at both symbol rates, the launch power is mainly determined by the tone and was measured to be 6.37 dBm for both symbol rates with a small variation beyond the resolution of the power meter. The span loss was 9.39 dB over 40-km reach. We first characterize the sensitivity improvement due to the SSBI mitigation by means of the KK algorithm as shown in the figure. It is seen that there exists a 2.6 dB sensitivity gain at the HD-FEC threshold of 3.8×10^{-3} for a 56 Gbaud PAM-4 signal, whereas a marginal sensitivity gain is seen at 83 Gbaud by KK. The explanation is that as the symbol rate increases, the modulation efficiency decreases because of a reduced driving voltage swing applied to the modulator and an increased RF $V\pi$, which leads to decreased SSBI. Therefore, the removal of the SSBI by the KK algorithm at 83 Gbaud does not provide a significant sensitivity gain compared to the case with a 56 Gbaud SSB PAM-4 signal. Note that at 83 Gbaud, the signal also suffers more from the uncompensated low-pass response of the PD+TIA that results in less effective mitigation of the SSBI based on the KK algorithm [82]. Moreover, there is stronger in-band thermal noise at 83 Gbaud due to a higher signal bandwidth which could dwarf the impact of the SSBI.

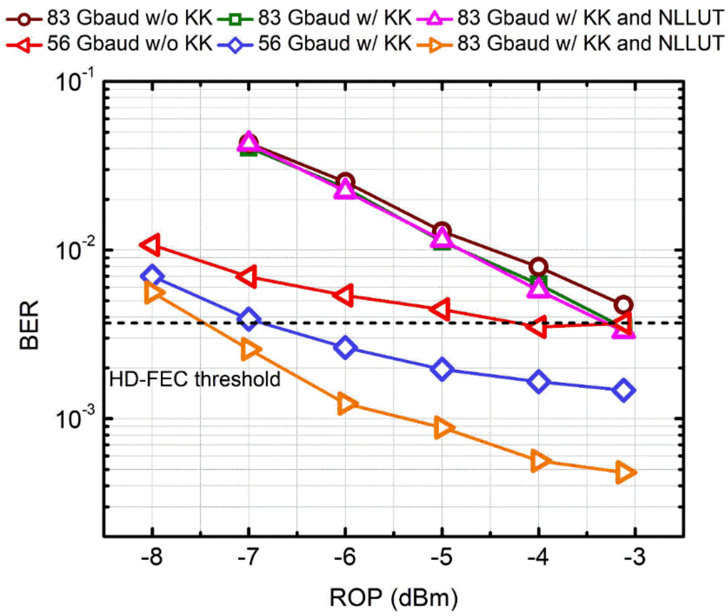

Fig. 4.8. BER versus ROP for a 56 and 83 Gbaud SSB PAM-4 signal transmitted over 40-km SMF, respectively.

Next, we test how the nonlinearity compensation improves the sensitivity by means of NLLUT with a 3-symbol memory length. Fig. 4.9 shows the NLLUTs for the 56 Gbaud and 83 Gbaud SSB PAM-4 signals at an ROP of -3.12 dBm, respectively. The NLLUTs are obtained by averaging the symbol error for each of the consecutive ternary symbol combinations at the receiver and are applied at the transmitter to pre-distort the symbols. As in the figure, the peak-to-peak symbol error of the 56 Gbaud signals is much higher than the 83 Gbaud signals, indicating a stronger nonlinearity. At a higher symbol rate, the modulator driving voltage is lower, the RF V_π is higher, therefore the system is less impacted from the modulator nonlinearity, and the TIA is less saturated due to a lower RF swing, all leading to reduced nonlinearity. This is in agreement with our observation of the curves with and without NLLUT in Fig. 4.8, where a 0.5 dB sensitivity improvement is seen for the 56 Gbaud signal, whereas the sensitivity improvement for the 83 Gbaud signals is almost negligible, indicating a weak nonlinearity in this case.

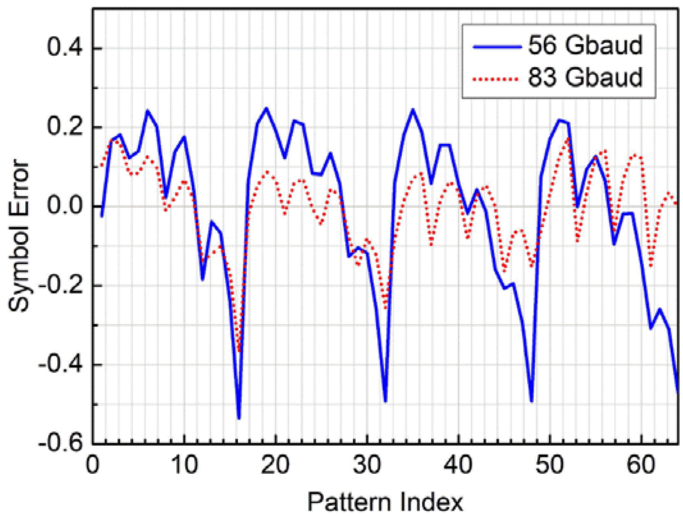

Fig. 4.9. The NLLUT for 56 and 83 Gbaud SSB PAM-4 signals transmitted over 40-km SMF.

We also study the attainable reach of our set-up using the proposed scheme by extending the transmission reach to 60-km of SMF. It is found that a 56 Gbaud SSB PAM-4 signal can be successfully transmitted with a BER below the HD-FEC threshold. The launch power and span loss are measured to be 6.37 dBm and 13.64 dB respectively. The BER versus ROP curve is shown in Fig. 4.10. It is observed that the SSB PAM-4 signal with

NLLUT has a slightly improved sensitivity and goes below the HD-FEC threshold of 3.8× 10^{-3} at an ROP of -7.27 dBm.

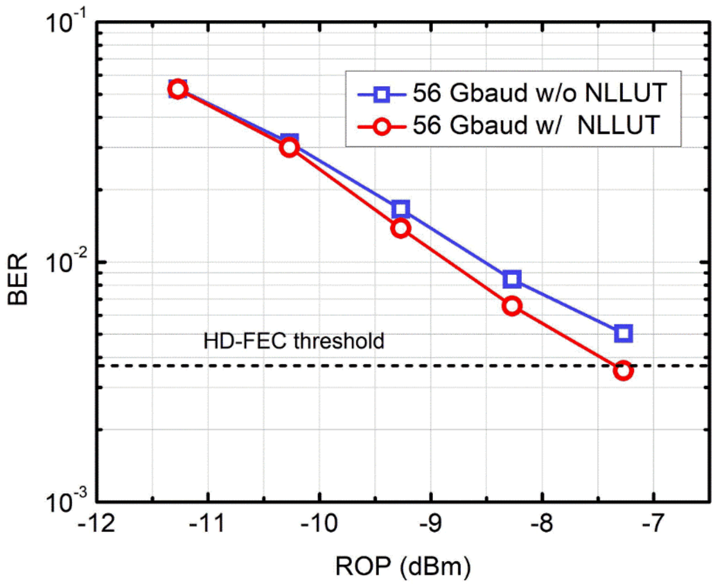

Fig. 4.10. BER versus ROP for a 56 Gbaud SSB PAM-4 signal transmitted over 60-km SMF.

In order to explore the attainable capacity of this setup, we assume the use of an SD-FEC encoder with a higher coding gain at the expense of an FEC overhead of approximately 20%. However, due to the limited bandwidth of the WQH, only a slightly higher symbol rate of 88 Gbaud results in a BER above the SD-FEC threshold of 2×10^{-2} for an SSB PAM-4 signal over a reach of 40-km. This is due to the strong image frequency components outside of the 40 GHz bandwidth of the WQH. In addition, it is found that the system SNR can only support up to a 60 Gbaud PAM-8 signal with a BER below the SD-FEC threshold with even lower throughput. Thus, within the bandwidth limit of 40 GHz, it is desirable to use intermediate spectral efficiencies to best exploit the link margin.

PS is a technique that allows flexible tuning of the spectral efficiency and outperforms uniformly distributed signals such that lower SNR is required to reach the same throughput in IMDD systems [55]. This technique is well-suited for the WQH-based setup, whose relative phase shift is maintained within a certain bandwidth. We transmit PS-shaped SSB signals and discuss the experimental results in the sequel.

In the experiment, PS is performed within the probabilistic amplitude shaping (PAS) architecture and a constant composition distribution matcher (CCDM) is used to map the bit to symbols following the Maxwell-Boltzmann distribution [19, 58]. We transmit a single carrier 40 Gbaud PS-256-QAM SSB signal over 40-km of SMF and plot the NGMI as a function of beta as shown in Fig. 4.11, where beta is the average number of bits used to generate a positive 8-level symbol. The signal spreads from 0 GHz to 40.4 GHz and the launch power and span loss are characterized to be 6.37 dBm and 9.37 dB, respectively. Note that no nonlinear compensation is performed in this section since the nonlinearity is negligible as we try to squeeze out extra throughput from the system by transmitting a wide bandwidth signal. We use a sufficiently long block length with a negligible rate loss and a practical FEC to assess the system performance which is formed by an SC-LDPC as the inner code and a BCH (8191,8126,5) as the outer code with altogether a combined code rate of 0.8402 (19.02% overhead) and an NGMI threshold of 0.88 [27].

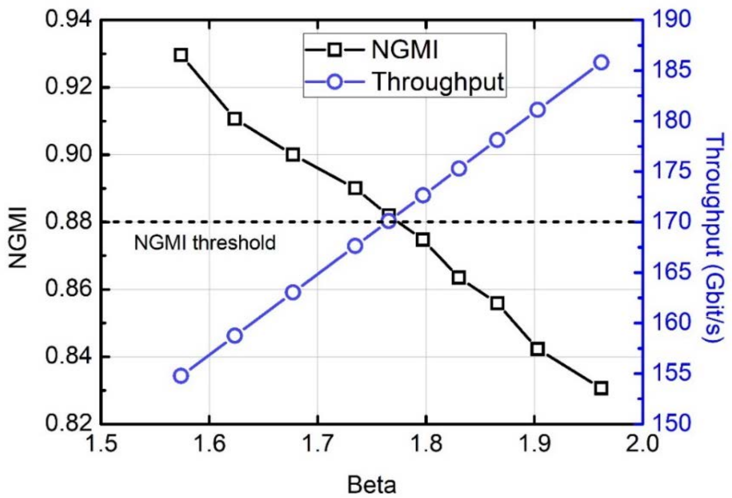

Fig. 4.11. The NGMI and throughout as a function of beta for a single carrier SSB PS-256-QAM signal transmitted over 40-km SMF.

The average number of information bits used to generate a sign bit of a real-valued symbol is expressed as:

$$gamma = 1 + m(c-1) = 1 + \log_2 16(0.8402-1) = 0.3608 \qquad (4.6)$$

where c is the code rate, m is the number of bits to label the PAM-16 symbols using the Binary Reflected Gray Code (BRGC). The throughput is calculated as:

$$Throughput = 2\times\left(Beta + gamma\right)\times baud \tag{4.7}$$

As can be observed in Fig. 4.11, the NGMI of 0.882 above the NGMI threshold is obtained at a beta value of 1.765. This corresponds to a throughput of 170.11 Gb/s with the distribution of the real-valued symbols after distribution matching and the received constellation shown in Fig. 4.12. Due to a very small probability at the outermost symbol levels and a limited symbol block length, these levels are not activated as shown in Fig. 4.12, thereby partially relieving the burden on the DAC ENOB. Note that additional truncation of the symbol levels could also help improve the system performance yet at the cost of extra DSP complexity. Note that WQH's outputs are also more imbalanced below 2 GHz out of the frequency range and we also tested whether setting a 2 GHz guard band would help improve the system throughput. However, we found that the 2 GHz guard band leads to a lesser throughput of 167 Gbit/s. The explanation is that the guard band causes the signal to be more impacted not only by the WQH imbalance at higher frequency but also the low-pass filtering of the system which results in higher ISI. Thus, it is desirable to set a very small or even zero guard band.

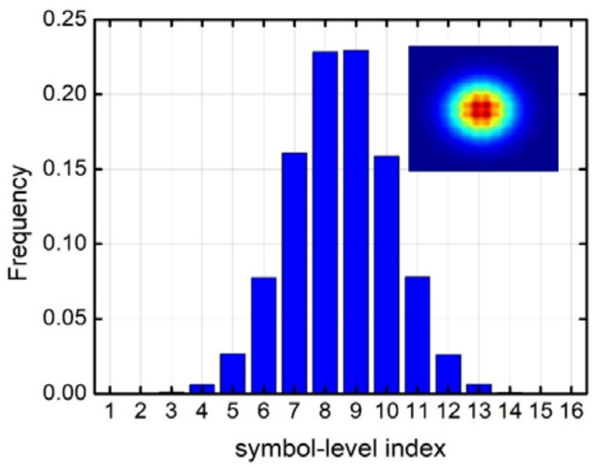

Fig. 4.12. The histogram of the symbols after distribution matching at a beta of 1.765. The inset shows a colored map to indicate the point density distribution. The point density decreases from red to blue.

However, even within the bandwidth of the WQH, the relative phase shift is found to deviate from 90^{o} and the WQH outputs are more imbalanced approaching 40 GHz, thus giving rise to frequency-dependent SNR. It is known that the throughput of a colored-SNR channel can be improved by loading appropriate entropy onto each subcarrier depending on its SNR. We transmit a 4-subcarrier SSB PS-256 QAM signal with constant water filling over a 40-km SMF with the baseband spectrum schematically plotted in Fig. 4.13 versus a single carrier signal. Each subcarrier operates at 10 Gbaud without a frequency gap in between or from the zero frequency. Note that a greater number of subcarriers and even digital multitone modulation are applicable yet at the cost of increased peak-to-average power ratio and higher implementation complexity.

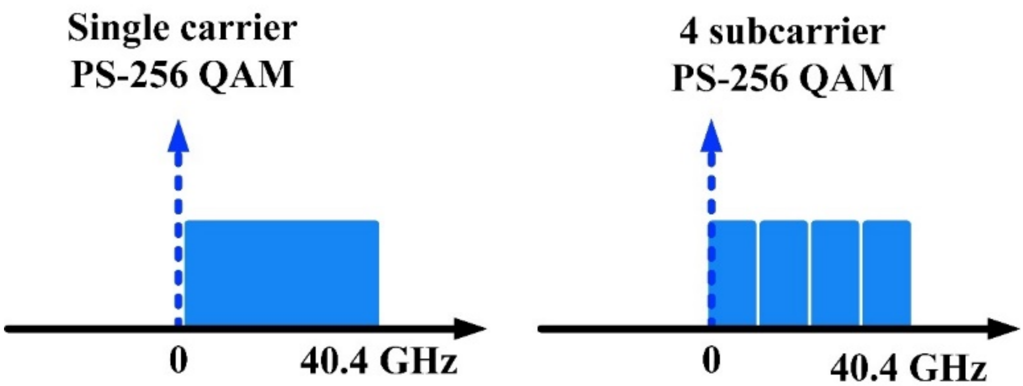

Fig. 4.13. Schematics of the single-carrier signal spectrum versus the 4-subcarrier signal spectrum.

The entropy of each subcarrier is tuned to be greater than the NGMI threshold assuming separate decoding. Table 4.1 shows the NGMI, beta, and throughput of each subcarrier with an aggregate throughput of 176.1 Gb/s, which is 5 Gb/s higher than the single carrier case. The launch power and span loss are measured to be 6.37 dBm and 9.39 dB, respectively. Fig. 4.14 (a)-(d) shows the constellations of subcarrier 1 to subcarrier 4 (SC1 to SC4), respectively. As indicated in the table, the beta of SC4 is lower than the other subcarriers since the relative phase shift deviation from 90^{o} is larger for the frequency components contained in SC4.

TABLE 4.1. The NGMI, beta, and net rate of each subcarrier.

	SC1	SC2	SC3	SC4
NGMI	0.881	0.880	0.881	0.881
beta	1.953	1.998	1.915	1.594
Throughput	45.562	46.432	44.811	38.494

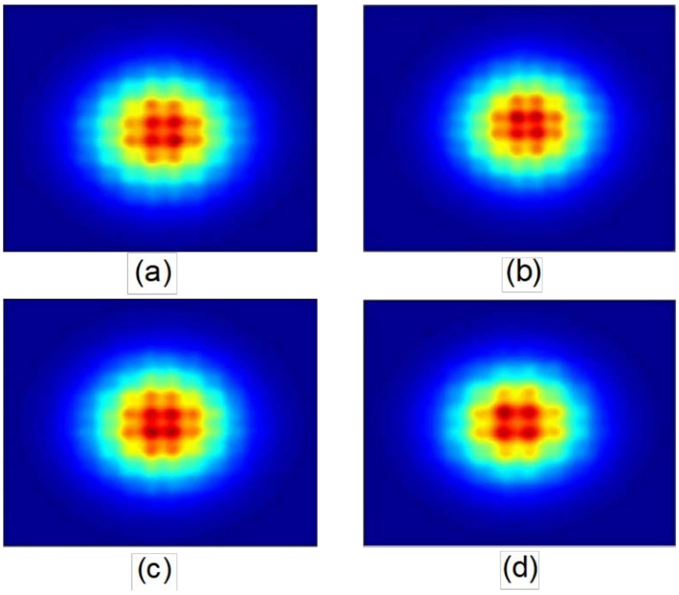

Fig. 4.14. (a)-(d) The constellations are shown in a colored map to indicate the point density distribution for subcarrier 1 to subcarrier 4, respectively. The point density decreases from red to blue.

4.3. SC-SSB signal transmitter based on a pair of time-misaligned differential signals and an offset WDM grid

4.3.1. Introduction

We present in section 4.2 an SC-SSB transmitter that generates wideband SC-SSB signals by converting an RF signal from a single DAC channel to a pair of Hilbert transform signals using a wideband quadrature hybrid. However, further scaling of the system throughput per carrier in this scheme is constrained by the limited bandwidth of the quadrature hybrid [78]. [83] shows that by using a strong Volterra equalizer, an image band suppressed by a notch in the spectrum allows the transmission of a 38 Gbaud PAM-4 signal over 80 km of SMF. However, at a higher symbol rate, the power fading becomes more severe due to an image band with a higher bandwidth, which could prevent this system from operating at a higher baud as required to attain a single-wavelength throughput of 200 Gb/s for the data center communications. Moreover, it is desirable to devise novel SC-SSB generation schemes that are readily compatible with a WDM system having a throughput of 800 Gb/s or 1.6 Tb/s over 40 km of reach as required in the future.

In this section, we describe an SSB generation scheme that is suitable for the generation of ultra-wideband SC-SSB signals within a WDM architecture [84]. This scheme utilizes a pair of time-misaligned differential signals from a single DAC to create a notch that suppresses the low-frequency image band components, and complementarily the passband filter edge of a WDM multiplexer (Mux) to suppress the high-frequency image band components. This joint approach lifts the bandwidth limit faced by RF SSB generation techniques while not increasing the hardware complexity of the system. With this WDM-SSB transmitter, we achieve net 823 Gbit/s probabilistically shaped (PS) PAM-8 signals over 40 km of SSMF in the C-band assuming a 20% overhead (OH) practical SD-FEC with an NGMI threshold of 0.88.

4.3.2. Delay assisted WDM-SSB transmitter with an offset WDM grid

Figure 4.15 depicts a schematic of the WDM-SSB transmitter (Tx) and the optical spectra at the output of the modulator and the DWDM multiplexer, respectively. The Tx architecture uses one DAC and a balun to produce a pair of differential signals, one of which is delayed by τ. When the time-misaligned differential signals drive a DDMZM, the output field has a notch within the image band as shown in Fig. 4.15(b). An analytical expression of the field $E_o(t)$ at the modulator output in the Fourier domain is $FFT\{E_o(t)\} = C - 2e^{-j\pi f\tau}\, sin(\varphi + \pi f\tau)S(f)$, where C is the CW-tone, φ is the phase shift in each MZM arm induced by a voltage bias, and $S(f)$ is the Fourier transform of the non-delayed driving signal [83]. This equation shows the tunability of the notch size and position by means of the modulator bias and the delay between the differential signals. In this scheme, we intentionally tune the notch close to the CW-tone to suppress the low-frequency image band components and leverage the DWDM Mux to complementarily reject the high-frequency image band components by offsetting the Mux grid such that the signal center wavelength is aligned with the edge of the Mux passband. This cost-effective combination of optical and RF image band rejection results in a spectrum shown in Fig. 4.15(c), where the image band is substantially suppressed.

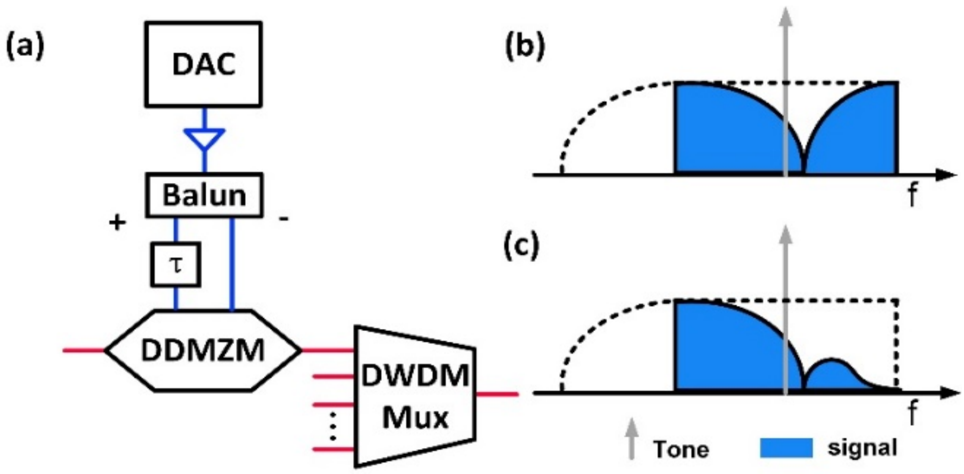

Fig. 4.15. Schematic diagrams of a) the WDM-SSB transmitter, b) the spectrum at the modulator output, and c) the spectrum at the common port of the Mux.

4.3.3. Experimental setup and DSP deck

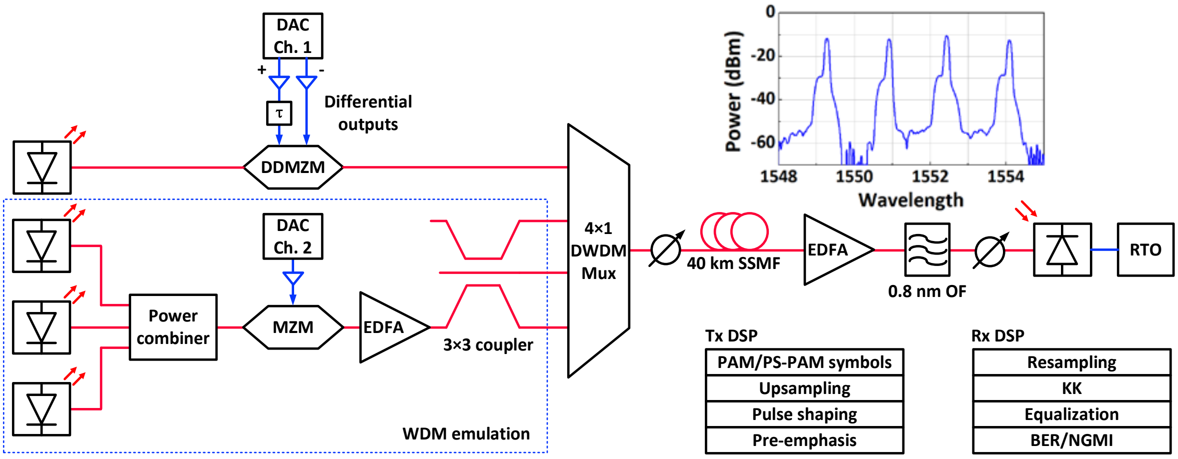

Fig. 4.16. Schematic of the 4×200 Gbit/s DWDM experimental setup and the DSP deck. Inset: optical spectrum of the Tx signal.

Fig. 4.16 shows the 4-channel DWDM experimental setup and the DSP deck at the transmitter and receiver. The 4×1 DWDM Mux has a bandwidth of 125 GHz with the passband center wavelengths ranging from 192.98 THz to 193.58 THz with a 200 GHz spacing. Four tunable external cavity lasers (ECL) generate 4 optical carriers, whose wavelengths are shifted to the passband edge to suppress the signal image band. We use an 8-bit 120 GSa/s DAC at the Tx to generate the RF signal preprocessed with Tx DSP including upsampling, pulse shaping, and pre-emphasis. The channel under test (CUT) utilizes the time-misaligned differential outputs of one DAC channel (Ch. 1) to drive the two arms of a DDMZM with a 3-dB E-O bandwidth of 30 GHz. Due to the lack of a high bandwidth RF Balun, we use the differential outputs of this DAC channel. More specifically, the temporal misalignment is realized by delaying one of the two RF outputs using a variable RF delay line. RF attenuators are cascaded after the amplifiers to optimize the RF signal power in order to mitigate the modulator nonlinearity. In the WDM emulator, the optical carriers from the other three ECLs are combined, bulk modulated by an MZM, and multiplexed with the CUT by means of a 3×3 coupler and a 4-channel DWDM multiplexer with a 200 GHz spacing. To equalize the power of the four DWDM channels in the WDM emulator, an EDFA is used to compensate for the insertion loss resulting from the power combiner, 3×3 coupler, and DWDM Mux. The WDM SSB signal is then propagated over 40 km of SSMF, pre-amplified, filtered by an 0.8 nm OF which emulates a demultiplexer (Demux) and detected by a photodetector (PD) without a TIA. Note that the pre-amplifier EDFA is enlisted because of a high insertion loss of 9 dB from the Mux and OF used in this setup. Given that Mux/Demux pairs with insertion loss per lane limited below 3 dB and a PD with TIA are used in the setup, the pre-amplifier could be eliminated over a transmission reach of 40 km. The signal out of the PD is sampled by an RTO operating at 160 GS/s and processed offline for the performance evaluation.

4.3.4. Results and discussion

We offset the WDM grid to partially reject the sideband of an SSB signal and measure the optical and electrical signal spectrum with and without an optimized RF delay between the differential driving signals. Fig. 4.17 shows the optical spectra of an 85 Gbaud PAM-4 signal propagated over 40 km of SSMF using a 0.05 nm-resolution optical spectrum analyzer (OSA).

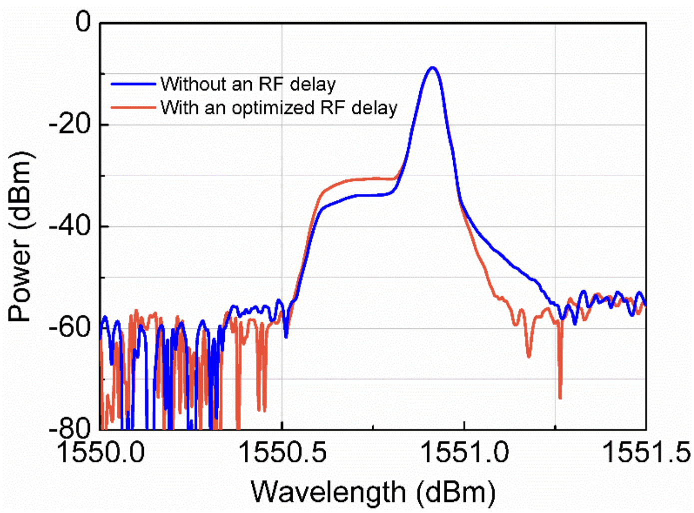

Fig. 4.17. Optical spectra of 84 Gbaud PAM-4 signal transmitted over 40 km of SSMF with and without an optimized RF delay.

The figure shows that without an RF delay, the residual image band is not effectively suppressed due to the limited edge roll-off of the multiplexer. By contrast, the image band is suppressed more completely with an optimized delay. This is in agreement with the electrical spectra as shown in Fig. 4.18 below.

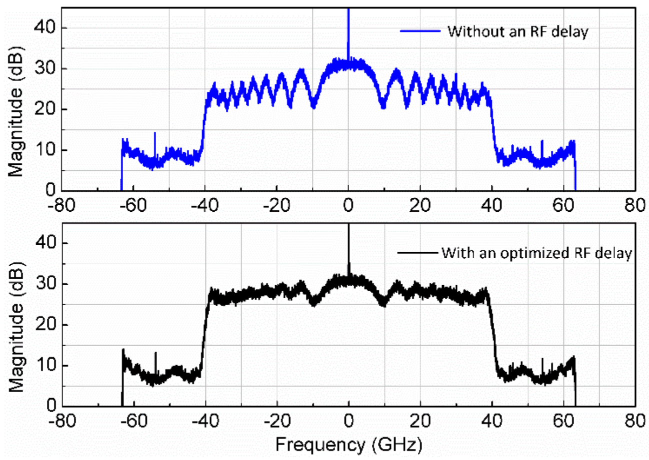

Fig. 4.18. Electrical spectra of 85 Gbaud PAM-4 signal transmitted over 40 km of SSMF with and without an optimized RF delay.

As observed from the figure, strong spectrum notches are present when no RF delay is applied since a stronger residual image band is more affected by the power fading. By optimizing the RF delay, the notches are substantially mitigated, which is due to improved suppression of the image band at a lower frequency.

In Fig. 4.19 we plot the BER of an 85 Gbaud PAM-4 signal of the CUT as a function of the launch power at a received optical power (ROP) of 8 dBm, with an offset WDM grid. Kramers-Kronig (KK) algorithm is performed to extract the field of the signal and a linear feed-forward equalizer (FFE) is used to compensate for the ISI. The figure shows that without an RF delay, the transmission performance is considerably worse due to a stronger residual image band at a lower frequency. In comparison, with an optimized delay, the BER decreases with an increasing launch power and then saturates at a launch power greater than 8 dBm due to the fiber nonlinear effect which gets stronger. Thus, the launch power is set to 8 dBm. Moreover, a CSPR of 15 dB is found to perform best at this symbol rate, which is tuned by controlling the swing of the MZM driving signals.

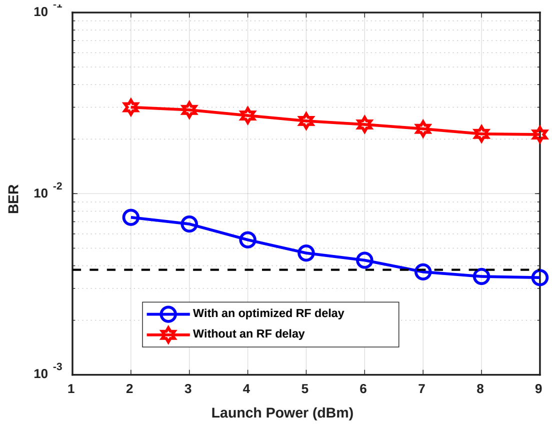

Fig. 4.19. BER vs. launch power for an 85 Gbaud PAM-4 signal transmitted over 40 km of SSMF at an ROP of 8 dBm.

Next, we plot BER versus ROP in Fig. 4.20 for the same transmitted signal. In the case with an offset Mux grid, the signal without an RF delay has a more pronounced image band, thereby leading to more substantial power fading and a much higher BER compared to the signal treated with an optimized RF delay. It is also found that the signal with an optimized delay reaches below the 3.8×10^{-3} pre-FEC threshold of an HD-FEC with a 7% overhead. The curve without a Mux grid offset and with an optimized delay is also included in this figure for comparison, which shows much higher BER due to the image band components at higher frequency without any suppression.

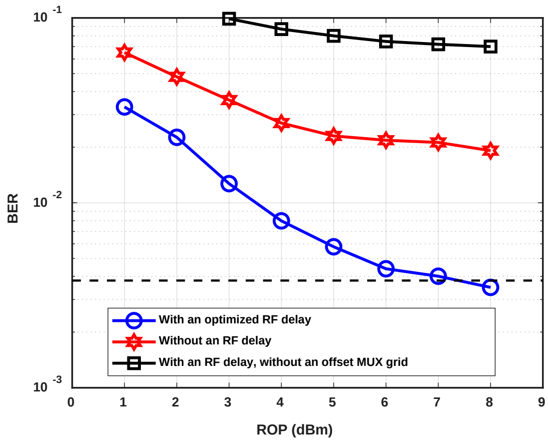

Fig. 4.20. BER vs. ROP for an 85 Gbaud PAM-4 signal transmitted over 40 km of SSMF.

Next, we transmit PAM-4 symbols at different symbol rates and show the results in Fig. 4.21. For the CUT, PAM-4 signals up to 87 Gbaud can be detected without error assuming the HD-FEC. This corresponds to 162.6 Gbit/s throughput, which is still lower than the target throughput of 200 Gb/s due to the system bandwidth. PAM-8 signals are also transmitted to evaluate the achievable system throughput assuming a 20% SD-FEC with an NGMI threshold of 0.88 which has a higher coding gain given the lower noise tolerance of this modulation format. It is found from Fig. 4.21 that PAM-8 signals cannot reach the NGMI threshold for a 200 Gbit/s throughput due to the requirement of high SNR.

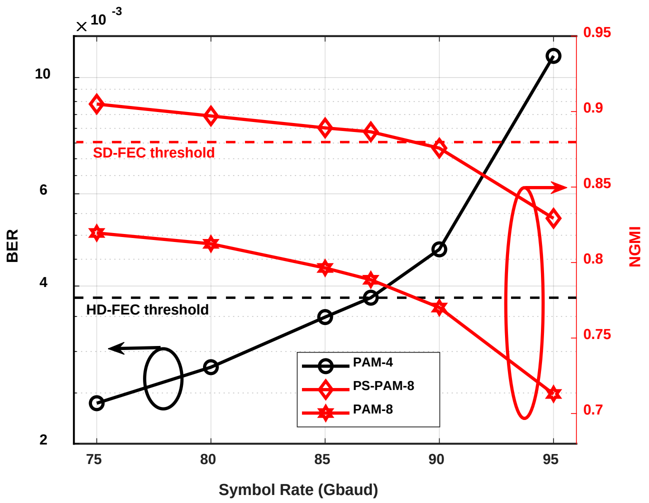

Fig. 4.21. BER and NGMI of signals with different modulation formats transmitted over 40 km of SSMF at different symbol rates.

Thus, we transmit PS-PAM-8 signals with intermediate SE following the Maxwell-Boltzmann distribution in order to push the throughput limit of the system. An information rate of 2.26 is found to achieve 200 Gbit/s with 88.8 Gbaud PS-PAM-8 signal for this channel. The attainable throughputs of the other channels are summarized in Table 4.2. All four channels can achieve net 200 Gbit/s data rate with NGMIs above the NGMI threshold, which leads to a total throughput of 823.5 Gbit/s. It is found that a symbol rate of 88.82 Gbaud and a CSPR of 15 dB achieves the best transmission performance for these channels.

Table 4.2. IBPS and Throughput of each channel.

	Ch 1	Ch 2	Ch 3	Ch 4
Information rate	2.33	2.26	2.33	2.35
Throughput	207	200.75	207	208.75

4.4. Direct Detection of polarization-division multiplexed SC-SSB signals

4.4.1. Introduction

As discussed in the overview of this chapter, the transmission performance of IMDD systems is severely degraded by CD-induced power fading in the C-band beyond 10 km of reach [71, 85]. This throughput constraint can be relaxed by transmitting an SC-SSB signal which allows the field reconstruction in the receiver DSP and digital compensation of the link impairments such that higher throughput can be achieved at extended reach [73, 86-88]. Polarization-division multiplexing (PDM) doubles the spectral efficiency such that fewer wavelengths are required to reach the same aggregate capacity when PDM and WDM are used simultaneously. This prospect could facilitate high-capacity transceivers with a compact footprint and has motivated the effort to realize PDM-SC-SSB systems [89]. One approach widely pursued in recent years uses the Stokes vector receivers (SVR) to demultiplex the dual-pol SSB signals [89-94]. In [89], the Kramers-Kronig (KK) algorithm is introduced into a PDM-SC-SSB-SVR system to retrieve the field of X-Pol based on $|X|^2$ obtained from the Stokes parameters S_0 and S_1. The field of Y-Pol is obtained by dividing the field of X-Pol from the beating term XY^* obtained from S_2 and S_3. [90, 91] proposed an alternative scheme that implements the KK algorithm after polarization de-rotation to recover the field of the PDM-SSB signal based on the intensities $|X|^2$ and $|Y|^2$. Later in [92], the SSB signal in the Y-Pol in [89] is replaced by a complex DSB signal to improve the spectral efficiency. However, PDM-SSB-SVR systems are complex in terms of the hardware, and an extra overhead from the data is required to train a de-rotation matrix. [95] reported a filter-based alternative for PDM-SSB signal that employs a pair of filters, PDs, and ADCs at the receiver. This scheme requires filters with a sharp slope (800 dB/nm) and iterative DSP to mitigate the inter-polarization signal-signal beating interference (SSBI) [87], which constrains the throughput of the digital signal processor.

In this section, we present a novel DD scheme for PDM-SC-SSB signals. The scheme has a simple receiver subsystem consisting of a single optical filter (125 dB/nm), two single-ended PDs, and two ADC channels [96]. We refer to this scheme asymmetric direct detection (ADD) in this section. The ADD scheme improves the spectral efficiency compared to [95] by assigning a guard band only in the X-Pol as opposed to a guard band in both polarizations. In addition, the DSP developed to linearize the received PDM-SSB signal does not require an iterative algorithm, and thus is more suitable for high throughput signal processing. At the receiver, the signal is split into two parts with one part being filtered before detection, whereas the other part is detected without filtering. The Y-Pol interference in the X-Pol is removed by exploiting the PD current difference, whereas the X-Pol SSBI in the Y-Pol is removed by a non-iterative estimate based on the intensity of the recovered X-Pol signal. The Y-Pol signal can be subsequently reconstructed by KK recovery. We first study the impact of system parameters on the performance of ADD at 40 Gbaud in the B2B configuration. We then demonstrate the transmission of a 52 Gbaud PDM 16-QAM signal with a BER below the soft-decision forward error correction (SD-FEC) threshold of 2×10^{-2}, which corresponds to a throughput of 346 Gbit/s (raw data rate 416 Gbit/s). We also conduct a numerical study on the effectiveness of a 2×2 multiple-input-multiple-output (MIMO) equalizer in mitigating the linear crosstalk resulting from the non-orthogonal PDM-SSB signals induced by the polarization-dependent-loss (PDL), which is often not negligible especially for the potential on-chip implementation of the ADD scheme [97-100].

4.4.2. Principle of the ADD scheme for PDM-SSB signal

The working principle of the ADD scheme is illustrated through a spectrum block diagram in Fig. 4.22. Figure 4.22(a) shows the optical spectrum of the transmitted PDM-SSB signal with orthogonal offset carriers assigned on the opposite edges of the signal similar to [95]. The signal can be generated via a dual-pol IQ modulator (IQM) driven by the amplified RF signals from a four-channel arbitrary waveform generator (AWG) as in [91, 95, 101, 102]. Compared with [95], the spectral efficiency of the PDM-SSB signal for ADD is improved, since a guard band is assigned only in the X-Pol between the signal and the carrier as opposed to a guard band in each polarization. The generated signal is split into two copies at the receiver, where one copy is optically filtered to attenuate the X-Pol offset carrier, whereas the other copy is detected without filtering as depicted in Figs. 4.22(c) and 4.22(b), respectively. When the X-Pol carrier power is negligibly low after filtering, the baseband spectra after square-law detection are schematically shown in Figs. 4.22(d) and 4.22(e), respectively. The subtraction of the photocurrent between Fig. 4.22(d) and Fig. 4.22(e) helps remove the interference from the Y-Pol, retaining only the linear term of the X-pol signal as shown in Fig. 4.22(g). Figure 4.22(g) is used to recover the X-Pol signal as well as estimate the X-pol SSBI shown in Fig. 4.22(f). Then Fig. 4.22(f) is removed from Fig. 4.22(e) to create the signal containing only the intensity of the Y-Pol signal shown in Fig. 4.22(h), which can be recovered by the KK method.

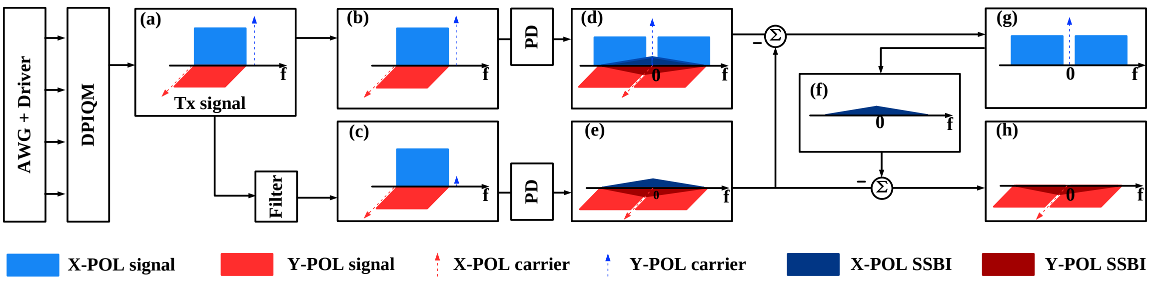

Fig. 4.22. The transmitted signal spectrum and the Rx signal spectrum evolution in the linearization DSP.

To best describe the feasibility of the scheme, we formulate the transmitted signal as below

$$E_T = \begin{pmatrix} T_X e^{jw_X t} + E_X \\ T_Y e^{j(-w_Y t)} + E_Y \end{pmatrix} + \begin{pmatrix} n_X \\ n_Y \end{pmatrix} \tag{4.8}$$

where E_T represents the transmitted signal as a Jones vector, E_X and E_Y represent the field of the X-Pol and Y-Pol, T_X and T_Y represent the carrier of X-Pol and Y-Pol, respectively, W_X and W_Y represent the upconversion frequency of the X-Pol carrier and Y-Pol carrier, respectively, and n_X and n_Y represent the in-band noise associated with E_X and E_Y, respectively. After square-law detection (Fig. 4.22(b) to Fig. 4.22(d)), the photocurrent generated by the unfiltered signal can be expressed as,

$$\begin{aligned} I_1 &= \left|T_X\right|^2 + \left|E_X + n_X\right|^2 + 2T_X \operatorname{Re}\left(\left(E_X + n_X\right)e^{-jw_X t}\right) \\ &+ \left|T_Y\right|^2 + \left|E_Y + n_Y\right|^2 + 2T_Y \operatorname{Re}\left(\left(E_Y + n_Y\right)e^{jw_Y t}\right) + n_{Th1} \end{aligned} \tag{4.9}$$

where n_{Th1} represents the combined electrical noise produced from the corresponding PD and ADC channels. Similarly, after square-law detection (Fig. 4.22(c) to Fig. 4.22(e)), the photocurrent generated by the filtered signal can be expressed as

$$\begin{aligned} I_2 &= \left|\alpha T_X\right|^2 + \left|E_X + n_X\right|^2 + 2\alpha T_X \operatorname{Re}\left(\left(E_X + n_X\right)e^{-jw_X t}\right) \\ &+ \left|T_Y\right|^2 + \left|E_Y + n_Y\right|^2 + 2T_Y \operatorname{Re}\left(\left(E_Y + n_Y\right)e^{jw_Y t}\right) + n_{Th2} \end{aligned} \tag{4.10}$$

where n_{Th2} represents the electrical noise produced from the other PD and ADC channels, and α characterizes the amount of residual carrier after filtering. The subtraction of I_1 from I_2 gives

$$I_1 - I_2 = \left(1-\alpha^2\right)\left|T_X\right|^2 + 2\left(1-\alpha\right)T_X \operatorname{Re}\left(\left(E_X + n_X\right)e^{-jw_X t}\right) + n_{Th3} \tag{4.11}$$

where n_{Th3} represents the electric noise after subtraction. The subtraction removes the common-mode signal of the photocurrents including the Y-Pol signal intensity

$|T_Y|^2 + |E_Y + n_Y|^2 + 2T_Y \operatorname{Re}\left((E_Y + n_Y)e^{jw_Y t}\right)$ and the X-pol SSBI $|E_X + n_X|^2$, therefore leaving only the desired linear term E_X and the direct current (DC) term which can be removed to recover the field of X-pol.

The Y-pol signal recovery DSP depends on the sharpness of the optical filter. When a sharp optical filter is used, the linearization DSP can be further simplified with α set to zero such that the X-Pol SSBI can be estimated using the recovered X-Pol signal and then removed in Eq. (4.10) for the subsequent processing of E_Y using the KK algorithm. When a slow roll-off filter is employed, α needs to be optimized to estimate and remove the undesired linear crosstalk $2\alpha T_X \operatorname{Re}\left((E_X + n_X)e^{-jw_X t}\right)$ in Eq. (4.10). Moreover, the overall signal-to-noise ratio (SNR) of the PDM-SSB signal degrades as α increases. This is due to the decreased linear term of E_X relative to the dominant PD and ADC noise n_{Th3} in Eq. (4.11); this further leads to reduced SNR for the recovered E_X signal. The SNR of E_Y is reduced as well since the estimate of the X-Pol SSBI $|E_X + n_X|^2$ in Eq. (4.10) depends on the SNR of E_X.

The impact of the distributed component PDL is often not negligible if the ADD scheme were to be implemented on a silicon photonics (SiP) chip, since the orthogonal transverse electric (TE) and transverse magnetic (TM) modes are subjected to different propagation losses and insertion losses due to the asymmetric silicon waveguide cross-section [97-99]. The presence of nontrivial PDL depolarizes the PDM-SSB signals, thus penalizing the system performance. The non-orthogonal PDM-SSB signal can be formulated as

$$E_T = \begin{pmatrix} T_X e^{jw_X t} + E_X + \cos(\theta)\left(T_Y e^{-jw_Y t} + E_Y\right) \\ \sin(\theta)\left(T_Y e^{-jw_Y t} + E_Y\right) \end{pmatrix} + \begin{pmatrix} n_X \\ n_Y \end{pmatrix} \tag{4.12}$$

where θ represents the angle between the depolarized SOPs.

By denoting $E_X + \cos(\theta)\left(T_Y e^{j(-w_Y t)} + E_Y\right)$ as E'_X, Eq. (4.12) can be reformulated as

$$E_T = \begin{pmatrix} T_X e^{jw_X t} + E'_X \\ \sin(\theta)\left(T_Y e^{j(-w_Y t)} + E_Y\right) \end{pmatrix} + \begin{pmatrix} n_X \\ n_Y \end{pmatrix} \tag{4.13}$$

which has a similar form as (4.8). Thus, the linear crosstalk between E'_X and E_Y can be resolved by means of a 2×2 MIMO equalizer. We conduct a numerical study to investigate the effectiveness of a 2×2 MIMO in mitigating the inter-polarization linear crosstalk in section 4.4.4.

4.4.3. Experimental setup and DSP deck

The digital generation of the offset carriers requires the perfect match of the signal amplitude and phase between the I and Q channels at the carrier frequency, which is over 30 GHz in the experiment. Otherwise, the presence of the image carriers creates extra interference terms that degrade the SNR. Due to the limited transmitter bandwidth of 14 GHz in our set-up, the suppression of image carriers beyond 30 GHz is hard to tune due to the imbalanced loss and phase difference resulting from the RF chains and child MZMs at higher frequencies. We follow to use separate lasers to generate the offset carriers in the experiment. Figure 4.23 shows the experimental setup and the DSP with the polarization-maintaining components shown in blue including the patch cord, power splitter, and power combiner. The IQ MZM biased at null point is driven by the linearly amplified RF signals from two channels of an 8-bit AWG to modulate the 1550.12 nm optical carrier from an external cavity laser (ECL). An EDFA follows to boost the signal power for CSPR control. Next, the SOP of the signal is aligned with the SOP of two separate lasers that generate the orthogonal offset carriers. The PDM signal is created through a polarization emulator comprising a power splitter, a variable optical delay line (VODL), a variable optical attenuator (VOA) and a polarization beam combiner (PBC). The decorrelation delay between the orthogonal SOPs is tuned to an integer number of symbol duration. After transmission, a pre-amplifier and a VOA are used to optimize the received optical power before electrical to optical conversion. At the receiver, the signal is split into two branches by a 50/50 power splitter. The signal in the upper branch is filtered by a Santec OTF-350 filter with a 125 dB/nm edge roll-off and then detected by a 50 GHz 3-dB bandwidth single-ended PD without a trans-impedance amplifier (TIA). The signal in the lower branch is attenuated by the same amount of power equivalent to the insertion loss of the filter in the upper branch before the PD. Finally, the waveforms are sampled and stored by a 160 GSa/s 8-bit real-time oscilloscope (RTO) with 62 GHz bandwidth for offline DSP processing.

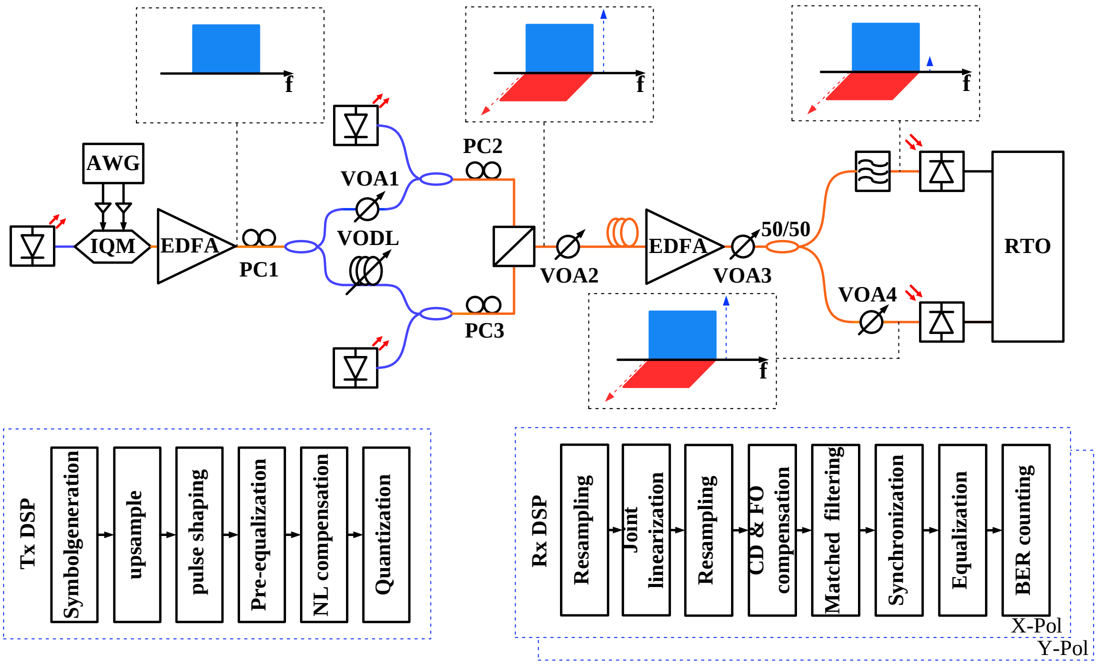

Fig. 4.23. Experimental set-up and DSP of the proposed scheme.

The Tx DSP generates 16-QAM symbols which are upsampled to the AWG sampling rate of 88 GSa/s for pulse shaping via a root-raised cosine (RRC) filter. Then a pair of pre-emphasis filters are applied to compensate for the low pass filtering of the transmitter for both quadrature channels. Next, modulator non-linearity is compensated before the signal is quantized and sent to the AWG memory for digital to analog conversion.

At the receiver, the sampled waveforms are resampled to 3 samples per symbol. Next, the PDM-SSB signal is linearized jointly following the procedure described in section 4.4.2, downconverted to the baseband and resampled to 2 samples per symbol. After compensating for CD, the frequency offset (FO) is compensated based on the 4th-power method [103]. The signal is then matched-filtered and synchronized for time-domain equalization. A phase-locked loop (PLL) interleaved single-input and single-output (SISO) feedforward equalizer (FFE) is employed to compensate for the ISI and the phase noise simultaneously. The equalizer filter contains 71 T/2-spaced taps, where T is the symbol duration. Finally, the symbols are determined and decoded for BER counting.

4.4.4. Results and discussion

We first conduct a parametric study at 40 Gbaud in the B2B configuration on the impact of various system parameters including the CSPR of each SOP, the roll-off factor of the RRC filter, and the guard band size. First, the CSPR is swept for each SOP with the roll-off factor and the signal-carrier guard band set to 0.1 and 13 GHz, respectively. Herein the CSPR is defined as the carrier power to signal power ratio per polarization. The optical filter is tuned to attenuate only the X-Pol carrier as much as possible without filtering the X-Pol signal. This helps improve the signal SNR as discussed earlier. The optical spectrum before and after filtering is shown in Fig. 4.24(a), where substantial attenuation of the X-Pol carrier is observed. Figs. 4.24 (b)-(d) shows the BER as a function of the Y-Pol CSPR when the X-Pol CSPR takes 11.85 dB, 14.24 dB, 16.39 dB, respectively. It is consistently found that the X-Pol BER increases with the Y-Pol CSPR, which is due to the increased inter-polarization crosstalk in the X-Pol due to the limited polarization extinction ratio of the PBC. By comparison, the Y-Pol BER reduces as the Y-Pol CSPR increases due to improved satisfaction of the minimum phase criterion for the KK algorithm. Despite the divergence of the X-Pol and Y-Pol BER curves, the average BER is the figure of merit which should be kept below the FEC threshold for error-free decoding given that the bits of the two polarizations are interleaved and decoded together using one FEC decoder. Among the three different X-Pol CSPR values, it is found that 14.24 dB corresponds to the minimum average BER. A lower X-Pol CSPR causes the X-Pol signal more vulnerable to the Y-Pol crosstalk, whereas a higher X-Pol CSPR degrades the signal SNR because of the decreased signal power after optical amplification due to larger proportion of the carrier power.

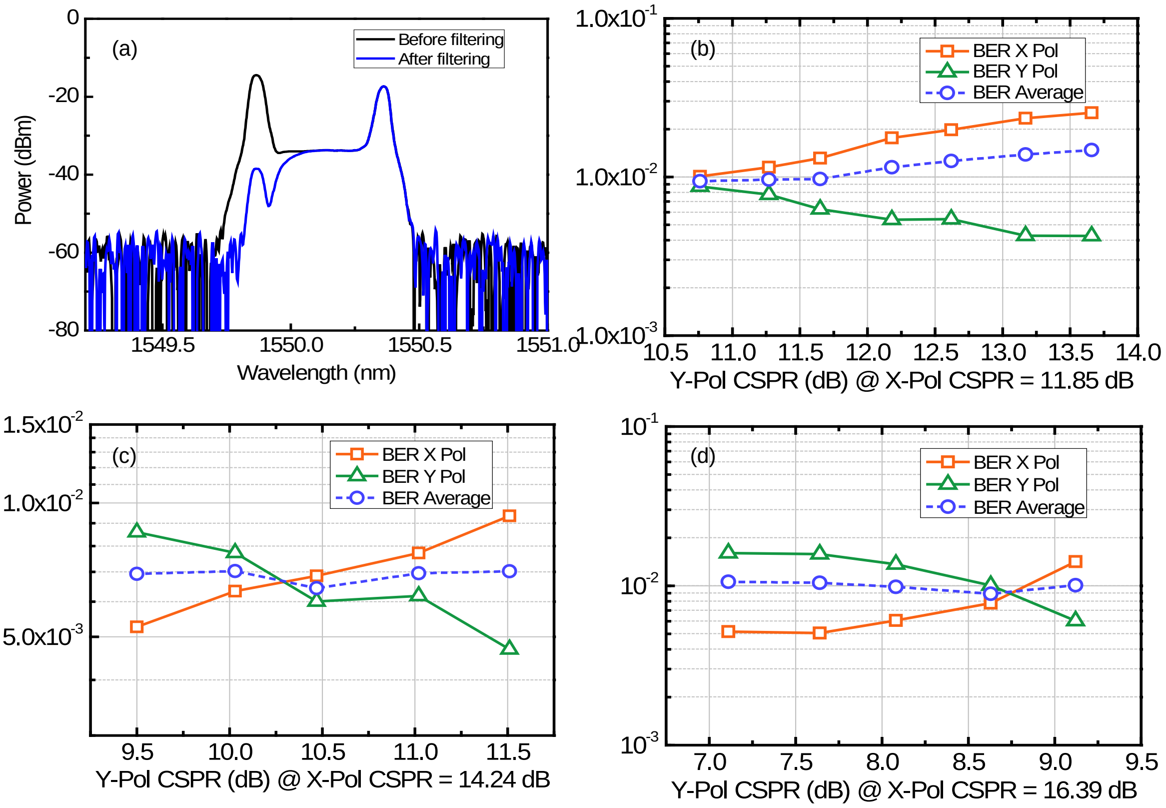

Fig. 4.24. (a) signal spectrum before and after optical filtering, (b) (c) (d) BER as a function of the Y-Pol CSPR when X-Pol CSPR equals to 11.85 dB, 14.24 dB, and 16,39 dB, respectively.

With the X-pol CSPR and Y-pol CSPRs set to 14.24 dB and 10.47 dB, respectively, we measure the BER change versus the RRC filter roll-off factor with the X-Pol carrier set away from the zero frequency by 35 GHz. Figure 4.25 plots the BER as a function of the RRC filter roll-off factor. It can be observed that as the roll-off factor of the RRC filter increases, the average BER increases and the X-Pol BER and Y-Pol BER diverge. This is caused by the increased filtering of the signal when the roll-off factor increases. As the signal has a higher excess bandwidth, the signal is more affected by the band-rejection filter. This not only detrimentally affects the effectiveness of the Y-Pol interference removal through the subtraction of the PD photocurrents but also degrades the X-Pol SSBI estimate. Hence, it is desirable to select a small roll-off factor for the ADD scheme and we proceed with a roll-off factor of 0.1 for the remainder of the following study.

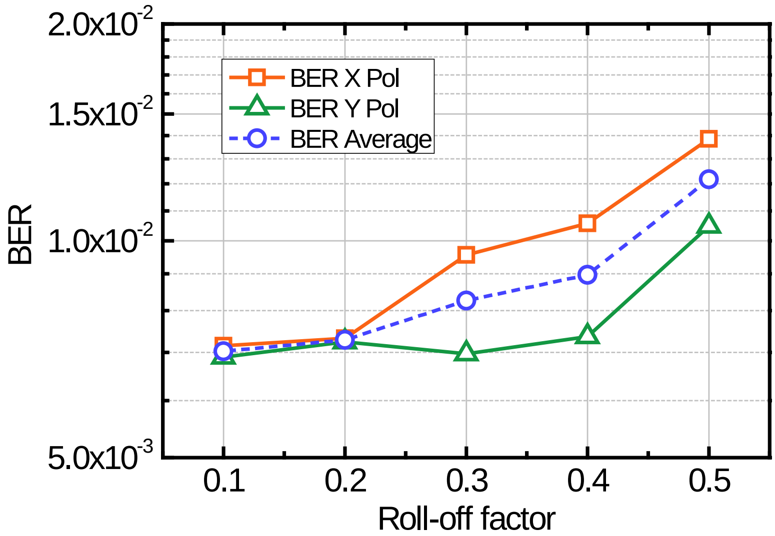

Fig. 4.25. BER as a function of the RRC filter roll-off factor.

Next, we study the tolerance of the system performance to a narrow guard band. Figure 4.26 plots the average PDM signal BER as a function of the guard band size. The two curves in the figure correspond to the coefficient α in Eq. (4.11) set to zero and an optimized value, respectively. For both cases, the average BER decreases with an enlarging guard band, since the X-Pol carrier is more suppressed, and the undesired signal filtering is relaxed. A steep BER decrease is observed when the guard band increases from 1 GHz to 8 GHz. For a guard band greater than 13 GHz, the BER levels off. It can also be observed that the average BER with optimized α is slightly smaller compared with α at zero, which is attributable to the removal of the linear X-Pol crosstalk in addition to the X-Pol SSBI while recovering the Y-Pol signal. However, the BER improvement is negligible with an optimized α, which indicates that the X-Pol SSBI is the dominant crosstalk in this experiment. This means that α can be set to zero with trivial penalty which simplifies the DSP.

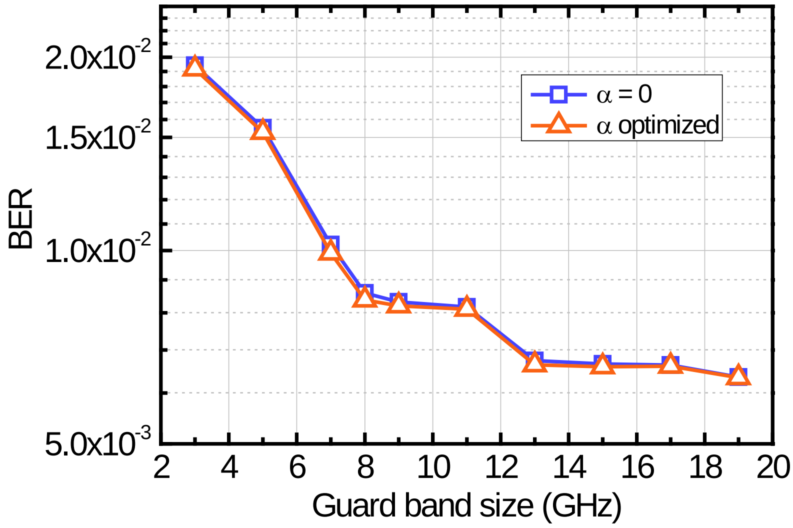

Fig. 4.26. Average BER versus the guard band size when α is set to either zero or an optimized value.

The pre-amplifier and VOA are then used to find the optimum incident optical power (IOP) to the single-ended PD at B2B. Figure 4.27(a) plots the BER as a function of the PD IOP of the unfiltered branch at B2B. It is shown in the figure that as the PD IOP increases, the BER decreases with more converged performance between two polarizations. This is due to the more dominant signal power relative to the power of the electrical noise produced by the PD and ADC, which improves the signal SNR. As a result, the IOP is selected as 7.4 dBm for the remainder of the following study.

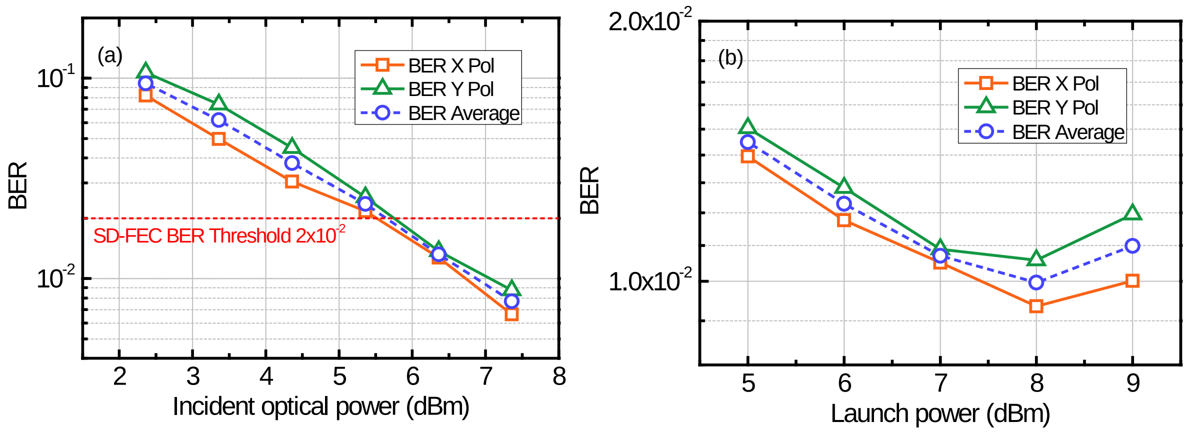

Fig. 4.27. (a) BER as a function of IOP in B2B; (b) BER as a function of launch power after 80 km.

Next, a transmission experiment is carried out over 80 km SSMF to optimize the launch power. Figure 4.27(b) plots the BER as a function of the launch power. As shown in the figure, the lowest average BER is obtained at a launch power of 8 dBm. Higher launch power will exacerbate the fiber nonlinear effects, while lower launch power will undesirably increase the noise from the EDFA. Therefore, 8 dBm is chosen as the optimum launch power.

Then we scale up the baud to explore the maximum throughput of the ADD-based system over 80 km of SSMF. The X-Pol carrier is fixed at 35 GHz away from the zero frequency for all the symbol rates. We cannot set the carrier to higher frequencies for symbol rates beyond 52 Gbaud due to the 63-GHz brick wall bandwidth of the RTO. The matched filter roll-off is 0.1, and the CSPRs of X-Pol and Y-Pol are fine-tuned around 14.24 dB and 10.47 dB respectively to achieve the minimum average BER with the optimized IOP and launch power.

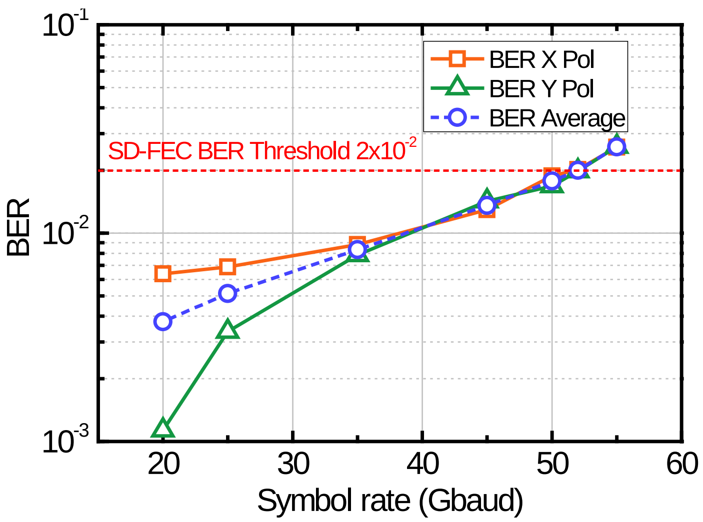

Fig. 4.28. BER versus symbol rate.

Figure 4.28 plots the BER as a function of the symbol rate. As the symbol rate increases from 20 Gbaud to 55 Gbaud, the guard band decreases from 24 GHz to 4.75 GHz, which introduces extra SNR penalty at higher symbol rates. By using an interleaved FEC encoder, the system with ADD can operate up to 52 Gbaud over 80 km SSMF with the average BER below the SD-FEC threshold of 2×10^{-2}, corresponding to a throughput of 346.6 Gbit/s (raw bit rate 416 Gbit/s) after removing the 20% overhead.

We also perform a numerical study of a 2×2 MIMO equalizer in mitigating the linear crosstalk resulting from the non-orthogonal PDM-SSB signals induced by PDL. Herein a lumped PDL emulator with constant PDL value is used in the simulation at 40 Gbaud at B2B. Figure 4.29(a) plots the angle deviation from 90° as a function of the PDL value when the angle θ between the SOPs and the main axis of the emulator equals to 0°, 15°, 45°. Since the angle deviation from 90° for a specific PDL is symmetric over $\theta = 45^o$, the curves with θ larger than 45° are not plotted in the figure. In addition, $\theta = 45^o$ corresponds to the largest angle deviation from 90°. Figure 4.29(b) plot the aggregate PDM signal SNR after SISO/MIMO equalization as a function of the angle deviation from 90°. It can be observed that the signal SNRs decrease with enlarging angle deviation for both SISO and MIMO equalization, but the MIMO equalization leads to higher signal SNR over the SISO counterpart with more than 6 dB SNR gain for angle deviations over 50°. This demonstrates the effectiveness of the 2×2 MIMO in mitigating the linear crosstalk for a single carrier PDM SSB signal. Taking the constant PDL as the worst PDL instance with an occurrence probability of 10^{-5}, the MIMO and the SISO equalizer have the 1 dB SNR penalty tolerance to mean PDL of 1.33 dB and 1.02 dB, respectively [104].

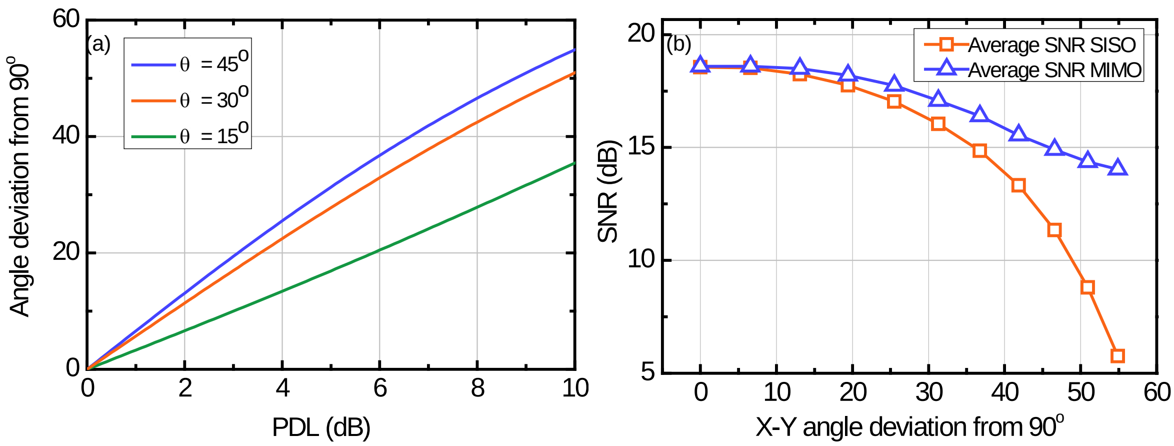

Fig. 4.29. (a) Angle deviation from 90o versus PDL. (b) Aggregate SNR versus X-Y angle deviation from 90o.

4.5. Conclusions

In this chapter, we present two approaches to generate wideband SC-SSB signals. The WQH-based approach converts a signal from a DAC channel into a pair of Hilbert transform signals, which drive a DDMZM to generate an SC-SSB signal. Based on this approach, we demonstrate the first amplifier-free transmission of a single-carrier net 100 Gb/s data rate over up to 60 km of SSMF. Moreover, we scale the net data rate to 176 Gb/s using MSC signaling and entropy loading over a reach of 40 km. To lift the bandwidth limit resulting from the WQH, we present another approach that uses a pair of time-misaligned differential signals and a WDM mux to jointly suppress the image band. Since the edge of the mux passband can effectively remove the high-frequency components of the image sideband, this approach can generate SC-SSB signals with a higher bandwidth compared to the WQH-based approach. An additional benefit is an inherent compatibility with a WDM architecture. Based on this approach, we demonstrate net 4×200 Gbit/s SSB PS-PAM-8 signals over 40 km of SSMF using only a linear equalizer. This cost-effective SSB signal generation scheme is attractive for realizing high-speed SC-SSB-DD systems for data center communications beyond 40 km of reach.

In order to further improve the capacity of SC-SSB-DD systems, we propose a polarization-division-multiplexed SC-SSB-DD scheme using a DD receiver referred to as ADD. The ADD receiver has a simple architecture, consisting of one optical filter, two single-ended PDs, and two ADC channels. The ADD scheme allows non-iterative signal linearization by exploiting the current difference to remove the inter-polarization interferences. We verify the feasibility of this scheme in a proof-of-concept experiment and achieve 416 Gb/s raw data rate (346.6 Gb/s net data rate) over 80 km of SSMF with an aggregate BER below the SD-FEC threshold of 2×10^{-2}. We also find that a 2×2 MIMO equalizer can effectively mitigate the linear crosstalk induced by PDL in the system.

5 Self-coherent double-sideband direct detection systems

5.1. Overview

As described in Chapter 1, DCO systems are entertained for 400G data center interconnects beyond 40 km due to higher throughput and spectral efficiency compared to IMDD systems [105-109], whereas IMDD systems are dominant for shorter reach connections, e.g. intra-data center communications below 10 km because of the simplicity and cost-efficiency. The lower throughput-distance product of IMDD systems is due to one-dimension modulation and the CD-induced power fading. As the required link capacity grows, the power fading effect becomes more severe due to a higher signal bandwidth such that more optical lanes are enlisted to reach the same aggregate throughput compared to DCO systems beyond 10 km of reach. This makes it challenging to meet the specifications of optical modules in terms of footprint and power consumption. Thus, as the link capacity grows, the lack of phase diversity of IMDD systems will constrain their deployment to an increasingly shorter connection distance.

In Chapter 4, we discuss an advanced DD scheme, i.e. SC-SSB-DD scheme, which attracts interest in recent years [87, 102, 110-116]. SC-SSB-DD schemes require a continuous-wave (CW) tone to co-propagate with an SSB signal in the fiber channel. After detection, the signal field can be retrieved from the signal-tone beating term. This scheme eliminates the need for a local oscillator (LO) at the receiver compared to DCO systems. Considering a CWDM configuration with wide wavelength spacing, the removal of the receiver LO can allow for uncooled lasers with lower cost and power consumption. Moreover, the DSP complexity is also reduced without a need to perform carrier phase recovery and frequency offset compensation. As detailed in Chapter 2, one major challenge of SC-SSB-DD schemes is the mitigation of the SSBI, which could appear within the signal band and compromise the signal SNR. Schemes proposed earlier use a guard band as wide as the information-bearing signal to accommodate the SSBI at the expense of reduced electrical spectral efficiency (ESE) [111], defined as the ratio between the signal throughput per unit electrical bandwidth (bit/s/Hz). Note that ESE is used to characterize the efficiency of the use of the receiver electrical bandwidth. The guard band can be reduced by removing the SSBI in an iterative manner [87, 110]. Alternatively, the Kramers-Kronig (KK) coherent detection handles the SSBI via the KK relation such that the guard band is eliminated provided that the CW-tone and the SSB signal satisfy the minimum phase condition as described in Chapter 2 [45, 117]. Note that SC-SSB-DD schemes can down-convert the full optical information to the electrical baseband, thereby enabling the digital compensation of CD and allowing for an extended transmission reach [46, 118]. Nonetheless, these SC-SSB-DD schemes have an inherent capacity limit: the CW tone is at the edge of the signal spectrum and no information is encoded in the image band. The unused image band not only constrains the ESE but also degrades the signal SNR since the optical noise in the image band beats with the CW tone after detection and contributes to the in-band noise.

Doubling the ESE without substantially increasing the complexity in DSP and system hardware is thus an appealing objective that requires novel DD schemes to reconstruct the field of *complex double-sideband* (DSB) signals [23, 119-121]. Otherwise, more optical lanes are required for SC-SSB-DD systems to achieve the same throughput at a given receiver electrical bandwidth, which requires more lasers and more stringent wavelength management. In [121], a time-domain interleaved scheme allocates the CW-tone and signal to different time slots and relies on two matched signal copies and a conventional coherent receiver to extract the in-phase and quadrature components of the electric field. However, the ESE is not improved compared to SC-SSB-DD schemes, because only half of the time-domain waveform carries a signal. In [23, 120] the carrier-assisted differential detection (CADD) is proposed, which restores the signal field by adding an extra PD to detect the intensity of a delayed signal copy in addition to the receiver structure in [121]. The ESE improvement is achieved using five PDs (2 BPDs and 1 PD) and three ADCs, which significantly increases the hardware complexity compared to SC-SSB-DD systems. Another approach utilizes two band-rejection filters to reject the opposite sidebands of an SC-DSB signal such that two PDs at the receiver detect an SC-SSB signal, respectively [119]. However, schemes based on band-rejection filters (BRF) are sensitive to the laser drift and make it more challenging to stabilize the wavelength. A sharp filter edge is required for BRFs to effectively reject the sideband, which is costly and difficult to fabricate in current filter technologies.

In this chapter, we propose a novel DD scheme for SC-DSB signals, which can increase the ESE by a factor of two compared to the SC-SSB-DD systems discussed in Chapter 4. We refer to this DD scheme asymmetric self-coherent direct detection (ASCDD) [75, 122]. The ASCDD scheme enables the field reconstruction of SC-DSB signals using two single-ended PDs and ADCs. Each PD detects a portion of the received optical signal that experiences different optical transfer functions via an optical filter having a configurable response. We derive equations to reconstructing the field of SC-DSB signals, such that link impairments including CD can be digitally compensated in the receiver DSP. Furthermore, we analyze the properties of the spectral singularities of the ASCDD scheme and discuss suitable signaling schemes in order to mitigate the impact of these singularities. Next, we discuss experimental results of two variations of ASCDD schemes based on a CD-filter and a BRF in section 5.3 and section 5.4, respectively. In section 5.5, we assess the impact of the filter response on the SNR of the reconstructed signal and show that the optimal filter is an all-pass filter whose phase response consists of an even part having a notch at 0 GHz. We discuss a different ASCDD scheme in section 5.6 where a Mach-Zehnder interferometer (MZI) is used in the receiver such that the two signal portions interfere with each other. We show that the MZI-ASCDD scheme also allows the field reconstruction of SC-DSB signals. Finally, we conclude this chapter by comparing the hardware complexity of different self-coherent direct-detection schemes in section 5.7 .

5.2. Principle of asymmetric self-coherent direct detection

Fig. 5.1 shows the architecture of the ASCDD scheme. The received optical signal is divided into two portions, which are detected by two single-ended PDs, respectively. The receiver of the ASCDD scheme has two branches, where two signal portions experience different optical transfer functions due to an optical filter (OF). The OF is configured in a way such that additional information can be obtained from the detection of the filtered signal portion. In order to maximize the SNR of the reconstructed signal, the filter response needs to be optimized.

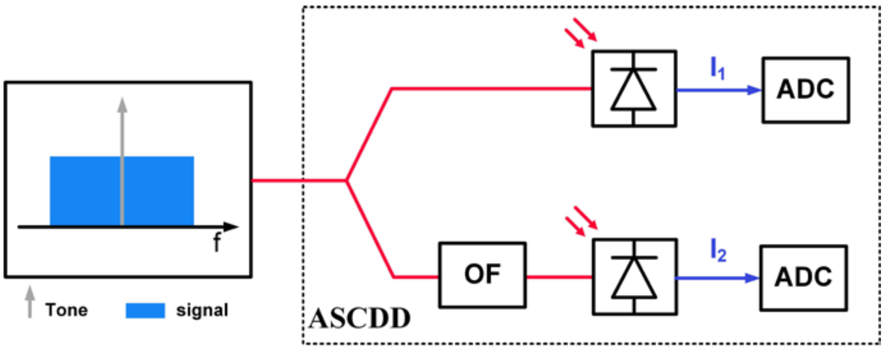

Fig. 5.1. Architecture of asymmetric self-coherent receiver. OF: optical filter.

The photocurrents after square-law detection are denoted as i_1(t) and i_2(t), which are expressed as follows:

$$i_1(t) = |T + s(t)|^2 + n_1(t) = |T|^2 + 2T\,\mathrm{Re}(s(t)) + |s(t)|^2 + n_1(t) \tag{5.1}$$

$$\begin{aligned} i_2(t) &= |(T + s(t)) \otimes h(t)|^2 + n_2(t) \\ &= |T \otimes h(t)|^2 + 2\,\mathrm{Re}\left(\overline{T \otimes h(t)} \cdot s(t) \otimes h(t)\right) + |s(t) \otimes h(t)|^2 + n_2(t) \end{aligned} \tag{5.2}$$

where T is the CW-tone, $s(t)$ is the complex DSB signal, h(t) is the transfer function of the optical filter, $\bar{x}$ represents the complex conjugate of x, n_1(t), and n_2(t) represents the noise. For the simplicity of the following analysis, we assume the noise terms to be uncorrelated white Gaussian noise, which has the highest entropy at a given noise power. Equations (5.1) and (5.2) both contain a DC component, a real part of the signal, and a signal-signal beating interference (SSBI).

By denoting $r_1(t)=|s(t)|^2$ and $r_2(t)=|s(t)\otimes h(t)|^2$, we express the photocurrents in the frequency domain as follows:

$$I_1(\omega)\text{-}R_1(\omega)=2TS_1(\omega)+N_1(\omega) \tag{5.3}$$

$$I_2(\omega)-R_2(\omega)=2T\text{Hermitian}\left\{\overline{H(0)}S(\omega)H(\omega)\right\}+N_2(\omega) \tag{5.4}$$

where the DC components are ignored, I_1, I_2, R_1, R_2, S, N_1, N_2 are the Fourier transform of i_1, i_2, r_1, r_2, s, n_1, n_2, respectively, subscripts I and Q denote the real and imaginary parts of the terms, respectively, Hermitian(x) denotes the part of x that equals its complex conjugate. Since it is more convenient to analyze the filter transfer function in polar coordinates, we express $H(\omega)$ in polar form as follows, whose amplitude and phase can be decomposed into even and odd parts denoted by the subscripts E and O, respectively.

$$\begin{aligned} H(\omega) &= A(\omega)\exp\left(j\Phi(\omega)\right) \qquad \left(0\le A(\omega)\le 1\right) \\ &= \left(A_O(\omega)+A_E(\omega)\right)\exp\left(j\left(\Phi_O(\omega)+\Phi_E(\omega)\right)\right) \end{aligned} \tag{5.5}$$

Note that $A_O(0)=\Phi_O(0)=0$ due to the property of odd functions. Without loss of generality, we set $\Phi(0)=0$, insert (5.5) into (5.4), and derive the equation below:

$$I_2(\omega)-R_2(\omega)=2T\left(S_I(\omega)Q(\omega)-S_Q(\omega)P(\omega)\right)+N_2(\omega) \tag{5.6}$$

where $Q(\omega)$ and $P(\omega)$ are expressed as follows:

$$Q(\omega)=A_E(0)\exp\left(\Phi_O(\omega)\right)\begin{pmatrix} A_E(\omega)\cos\left(\Phi_E(\omega)\right) \\ +jA_O(\omega)\sin\left(\Phi_E(\omega)\right)\end{pmatrix} \tag{5.7}$$

$$P(\omega)=A_E(0)\exp\left(\Phi_O(\omega)\right)\begin{pmatrix} A_E(\omega)\sin\left(\Phi_E(\omega)\right) \\ -jA_O(\omega)\cos\left(\Phi_E(\omega)\right)\end{pmatrix} \tag{5.8}$$

Thus, we derive the equations of the real and imaginary parts of the received DSB signal in the frequency domain:

$$S_I(\omega)+\frac{N_1(\omega)}{2T}=\frac{I_1(\omega)-R_1(\omega)}{2T} \tag{5.9}$$

$$S_Q(\omega)+\frac{N_1(\omega)Q(\omega)+N_2(\omega)}{2TP(\omega)} =\frac{\left(I_1(\omega)-R_1(\omega)\right)Q(\omega)-\left(I_2(\omega)-R_2(\omega)\right)}{2TP(\omega)} \tag{5.10}$$

SC-DSB signals can be reconstructed from photocurrents I_1 and I_2 based on (5.9) and (5.10) with the impact of the noise and SSBI moved to the left side of the equations. However, observing that $S_Q(\omega)$ recovered based on (5.10) is impaired by a noise term as a function of $Q(\omega)$ and $P(\omega)$, $H(\omega)$ should be optimized in order to maximize the signal SNR. In addition, the ASCDD scheme can be extended to a dual-polarization configuration by use of a controllable polarization rotator concatenated with a polarization beam splitter (PBS), which ensures that the CW tone is equally split between the two output ports of the PBS [123, 124]. There are also other ways to realize a dual-pol ASCDD scheme, which is beyond the scope of our discussion. Fig. 5.2 depicts a schematic of the SSBI mitigation process by means of a recursive feedback algorithm. During a first field recovery based on (5.9) and (5.10), the SSBI terms $R_1(\omega)$ and $R_2(\omega)$ are set to zero. The restored signal field S(ω) is utilized to estimate $R_1(\omega)$ and $R_2(\omega)$, which are fed back, and removed from the photocurrents I_1 and I_2 according to (5.9) and (5.10). Thus in the section iteration, the estimate of S(ω) has improved accuracy due to alleviated SSBI terms. The SSBI cancellation is implemented iteratively until the impact of SSBI is marginal compared to the system noise.

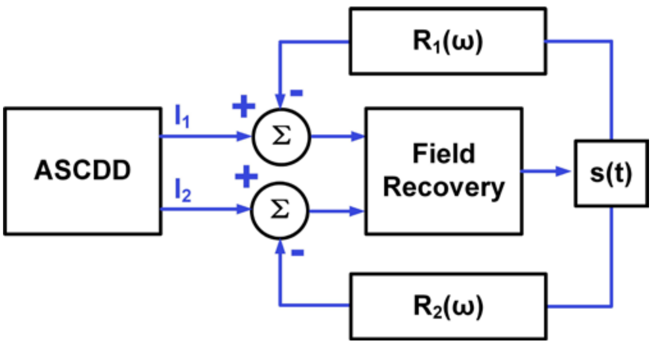

Fig. 5.2. Schematic of the recursive SSBI mitigation algorithm.

In addition, it is found that $P(\omega)=0$ at $\omega=0$ regardless of the design of the filter frequency response and the ASCDD scheme inherently loses the information of the imaginary part at $\omega=0$ based on (5.6). This incidates that the noise in the imaginary part of the signal as expressed in (5.10) has a singularity at $\omega=0$. Thus, the transmitted signal requires a guard band in order to mitigate the noise enhancement around this singularity.

5.3. ASCDD systems with a chromatic dispersion filter

In this section, we describe the numerical and experimental results of an ASCDD scheme based on a CD-filter in the receiver. Compared to the carrier-less signaling scheme reported in [125], thousands of iterations are not required since the field recovery is performed using the equations (5.9) and (5.10) derived in the last section. There is also no need to set the receiver electrical noise to zero due to the finite difference approximation in [126]. Another advantage of the CD-filter-based ASCDD scheme is the availability of mature CD components including dispersion-compensating fiber, and grating structures. This scheme is also compatible with a WDM architecture as displayed in Fig. 5.3, where the CD filter can be shared by multiple optical lanes to reduce the component cost. There are also other different filter transfer functions which can enable field reconstruction based on the ASCDD scheme, which will be detailed in the next section.

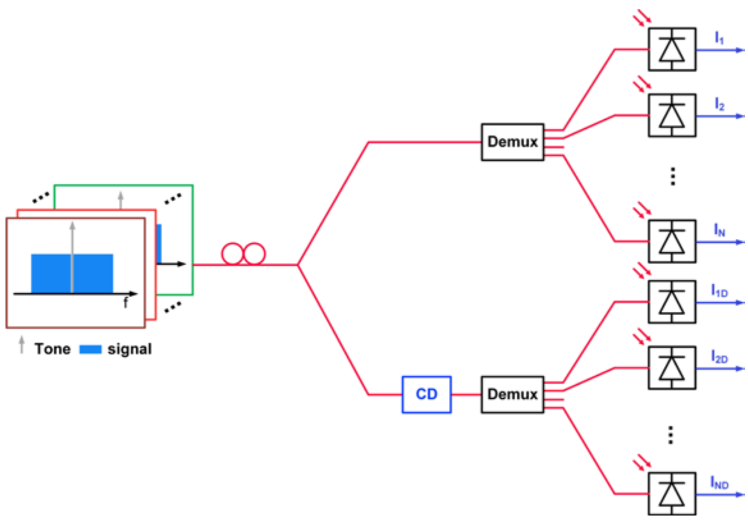

Fig. 5.3. Schematic of a WDM architecture compatible with the ASCDD scheme.

First, we characterize the performance of the CD-based ASCDD scheme. Based on (5.9) and (5.10), the reconstructed field is expressed as follows:

$$\hat{S}_I(\omega) = \frac{I_1(\omega) - R_1(\omega)}{2T} \tag{5.11}$$

$$\hat{S}_Q(\omega) = \frac{\left(I_1(\omega) - R_1(\omega)\right)\cos\left(\omega^2 \beta_2 L / 2\right) - \left(I_2(\omega) - R_2(\omega)\right)}{2T \sin\left(\omega^2 \beta_2 L / 2\right)} \tag{5.12}$$

where $\hat{S}_I(\omega)$ and $\hat{S}_Q(\omega)$ represent the estimates of the imaginary and real parts of the signal in the frequency domain, respectively, β_2 is the second-order derivative of the filter's propagation constant, and L is the length of the filter. The system configuration in the numerical analysis is as follows: a self-coherent DSB signal pulse-shaped via 0.1 raised-cosine filter is propagated over 80 km of single-mode fiber. The fiber channel is assumed linear, lossless with a CD coefficient of 17 ps/nm/km. AWGN is linearly added to the signal to simulate the amplified spontaneous emission (ASE) noise in order to investigate the theoretical performance of the ASCDD scheme. In addition, the electrical bandwidth of the PD and ADC is simulated using a brick-wall filter for which a minimum bandwidth is chosen to pass only the tone-signal beating term and reject the out-of-band noise and interferences. The postprocessing DSP includes signal field recovery, CD compensation, synchronization, linear equalization, and BER counting.

Based on the analysis in section 5.2, the ASCDD scheme has a singularity at 0 GHz regardless of the filter response, which results in noise and SSBI enhancement in the recovered signal field. Thus, the transmitted self-coherent DSB signal is composed of two independent signal sidebands, each with a guard band between the CW-Tone and the edge of the signal spectrum. Each sideband carries a single-sideband PAM 4 signal at 28 Gbaud, which leads to an aggregate symbol rate of 56 Gbaud.

Fig. 5.4. plots the BER as a function of OSNR for the CD-based ASCDD scheme at varied CD values. Note that the power of the CW-tone is considered as part of the 'signal power' for the OSNR calculation. The CSPR and guard band are set to 11 dB and 2 GHz, respectively. 4 iterations are implemented to mitigate the impact of SSBI. It can be

observed from the figure that the BER only depends on the absolute value of CD. In addition, the lowest BER is achieved at an absolute CD of 350 ps/nm among three different CD values. The performance difference at varied CDs is due to the changed profile of the noise and the SSBI which are enhanced by multiple singularities of $1/P(\omega)$ due to the use of a CD filter. To visualize this more clearly, we show in Fig. 5.5 the noise-SSBI spectra of the reconstructed signal based on (5.9) and (5.10) at two absolute CD values of 200 ps/nm and 500 ps/nm.

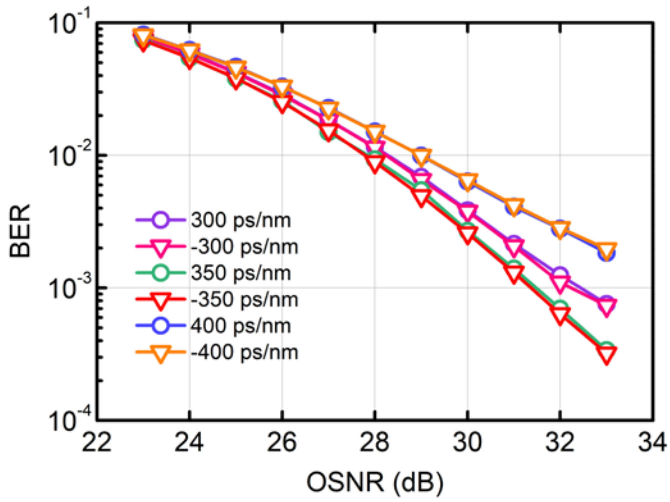

Fig. 5.4. BER as a function of the OSNR at varied CD for the CD filter-based ASCR. The performance of the optimal filter is also included as a reference.

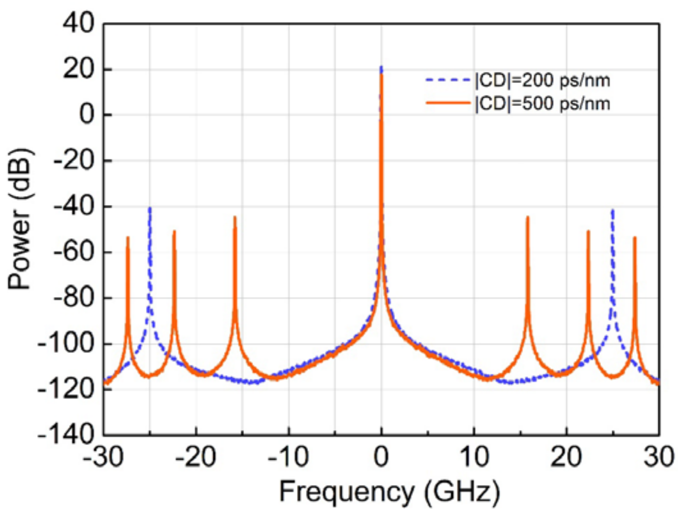

Fig. 5.5. Noise spectra at different CDs of 300, 350 and 400 ps/nm.

It is seen from Fig. 5.5 that the CD-based ASCDD scheme has multiple singularities, which enhances the noise and the SSBI. Furthermore, at a higher absolute CD of 500 ps/nm compared to 200 ps/nm, the separations between the singularities are reduced and the enhanced noise and SSBI are less pronounced around the 0 GHz singularity. Thus, at an absolute CD higher than the optimal value, e.g. 400 ps/nm used in Fig. 5.4, the second-order singularities moves within the signal bands and enhances the noise and the SSBI, whereas at an absolute CD lower than the optimal value, e.g. 300 ps/nm, the enhanced noise and SSBI around 0 GHz are more pronounced, which also leads to deteriorated performance. Due to the above reason, the absolute CD should be optimized to properly accommodate the signal bands within the frequency intervals separated by the singularities in order to minimize the noise-SSBI enhancement. Note that the requirement of an optimal CD can be relaxed by sending an SC-DSB signal with multiple digital subcarriers, each loaded with an appropriate information rate. This modulation format offers more flexibility such that the frequency intervals at higher frequency can be utilized, which is advantageous for achieving a higher aggregate symbol rate.

As described in section 5.2, the SSBI is mitigated iterativly. Since more iterations increase the implementation complexity of the algorithm, it is important to determine the minimum iteration number required to effectively mitigate the SSBI. In Fig. 5.6, we plot BER as a function of the iteration number at varied OSNRs. It is seen in this figure that the BER curves first decrease and then level off when greater than 4 iterations are performed. More specifically, as the OSNR decreases from 33 dB to 27 dB, the iteration number required to reach the BER floor decreases from 4 to 2. This is the consequence of a stronger ASE noise power at a lower OSNR such that the impact of the residual SSBI becomes already marginal after fewer iterations

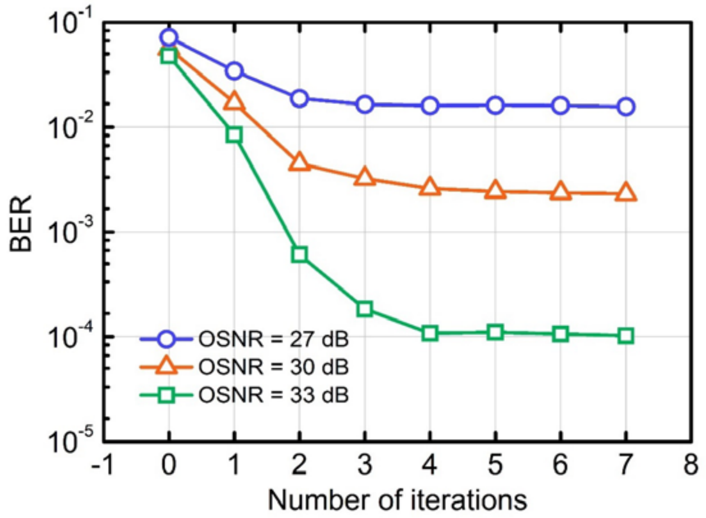

Fig. 5.6 BER change as a function of the number of iterations at different OSNRs.

The effectiveness of the iterative SSBI cancellation algorithm can be visualized from Fig. 5.7, where the noise spectra after 4 iterations are plotted against the spectra without SSBI cancellation. Note that both the noise and residual SSBI are enhanced in Fig. 5.7 due to the singularities. The figure shows a significant noise power reduction after 4 iterations of SSBI cancellation, which explains the performance improvement in Fig. 5.6.

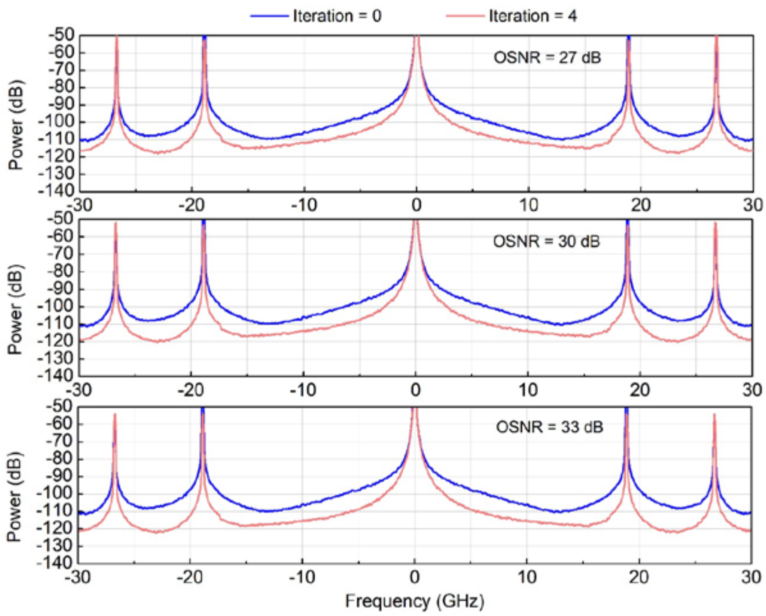

Fig. 5.7. Change of the noise spectra after iterative SSBI cancellation at different OSNRs.

Next, we characterize the performance impact of the guard band and CSPR with the iteration number and CD configured to the optimal values accordingly. Fig. 5.8 shows the change of the BER as a function of the CSPR at an OSNR of 30 dB and the guard band is varied from 1 to 3 GHz. It is found that all the curves are convex, because at a lower CSPR the SSBI removal is less effective due to inaccurate SSBI estimates, whereas at a higher CSPR, the ratio between the effective signal power and the ASE noise power is reduced since the CW-tone also contributes to the total signal power. In addition, we find that a slightly wider guard band can significantly improve the transmission performance, which is attributed to the alleviated impact from the enhanced noise and SSBI near the 0 GHz singularity.

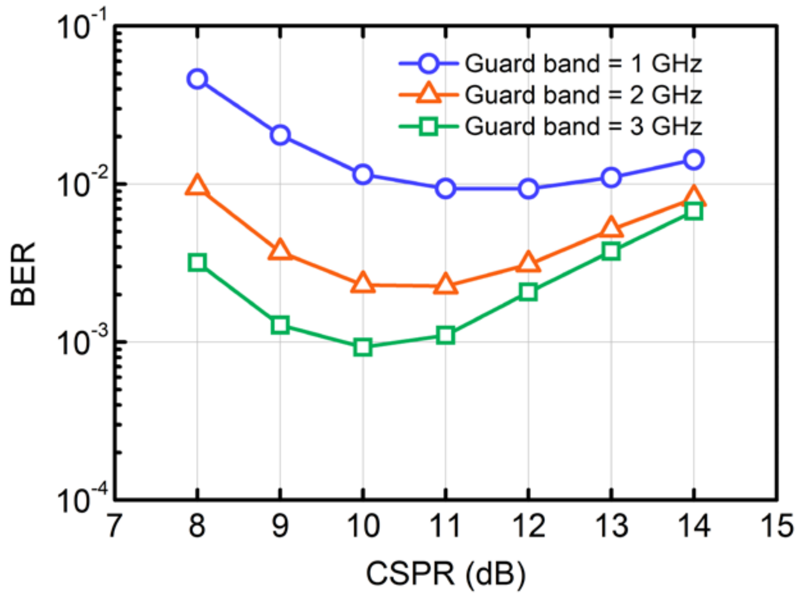

Fig. 5.8. BER vs. CSPR at varied guard bands from 1 to 3 GHz.

Next, we experimentally validate the principle of the ASCDD scheme based on a CD filter. Fig. 5.9 depicts the experimental setup and DSP blocks of the transmitter and receiver. The self-coherent DSB signal is generated from a dual-drive Mach-Zehnder modulator (DDMZM) with a 3 dB E-O bandwidth of 30 GHz. The DDMZM is biased at the intensity quadrature such that a CW-tone is produced to produce a self-coherent signal. Two channels of an arbitrary waveform generator (AWG) operating at 88 GSa/s are used to provide the in-phase and quadrature driving signals. After propagation over 80 km of single-mode fiber, the optical signal is pre-amplified by an EDFA before impinging upon the CD-based ASCDD. The CD filter is realized by a tunable dispersion compensation module (DCM). Note that two PDs with trans-impedance amplifiers having a 3-dB bandwidth of 35 GHz are used to detect the two parts of the split optical signal, respectively, which are subsequently sampled by 62-GHz ADCs with a sampling rate of 160 GSa/s. A brick-wall filter with a 17.4 GHz bandwidth is used to limit the electrical bandwidth of the receiver for a 56 Gbaud PAM-4 signal with a 2 GHz guard band per sideband. The two variable optical attenuators (VOA) are used to adjust the launch power and the incident optical power to ASCDD, respectively. In the transmitter DSP, two independent PAM-4 signals are pulse-shaped via a raised-cosine filter with a roll-off factor of 0.1, transformed into SSB PAM 4 signals, and subsequently up-converted to an intermediate frequency to accommodate a guard band for the 0 GHz singualrity. Pre-compensation of the modulator nonlinearity is performed based on [127], and followed by a pe-emphasis filter to flatten the response of the transmitter RF chain. In the receiver postprocessing DSP, the field reconstruction is implemented based on the derived analytical solution. After synchronization, MIMO equalization is performed to remove the ISI and linear crosstalk due to imbalanced PD responses.

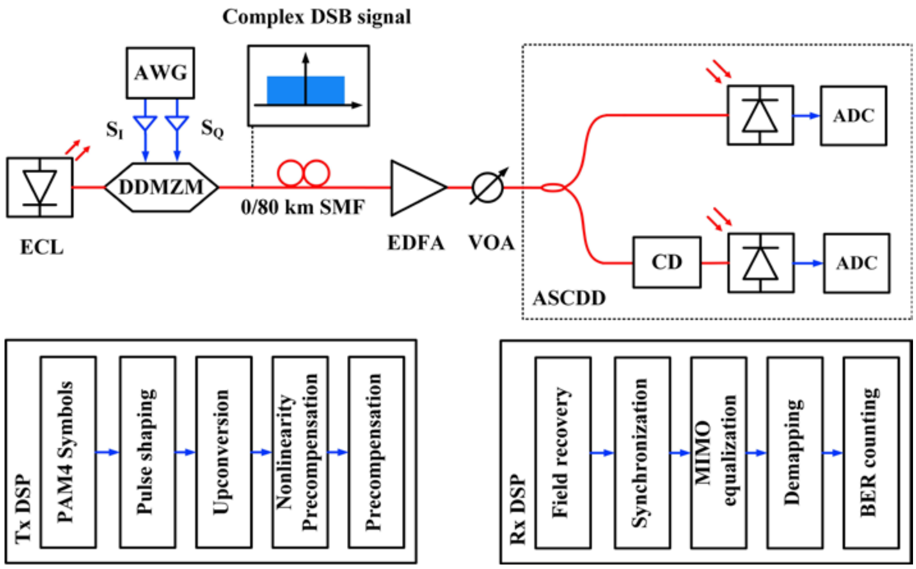

Fig. 5.9. Experimental setup and DSP decks of the transmitter and receiver.

Note that the DDMZM nonlinearity needs to be carefully handled; otherwise, the transmission performance will be significantly compromised. In order to generate a SC-DSB signal of the form $a(t)\exp(j\varphi(t))$, the driving RF signals V1 and V2 that pre-compensates the nonlinear transfer function of the DDMZM are expressed as

$$V_1 = \frac{V_\pi}{\pi}\left[\varphi(t) + \sin^{-1}(a(t))\right] \tag{5.13}$$

$$V_2 = \frac{V_\pi}{\pi}\left[\varphi(t) - \sin^{-1}(a(t)) + \pi/2\right] \tag{5.14}$$

respectively, where V_π is the voltage to induce a π phase shift in one DDMZM arm, $a(t)$ is the amplitude of the signal and $\varphi(t)$ is the phase of the signal. Since the AC-coupled driving signals in our setup has a limited swing, a relatively high CSPR of 17 dB is needed in order to invert the nonlinear transfer function of the modulator based on (5.13) and (5.14). Note that the CSPR can be reduced by use of driver amplifiers with a higher gain or the transmitter structure in [120] where an IQ-MZM with moderate nonlinearity is utilized. However, since a single EDFA is used in the proof-of-concept experiment, the performance impact of the ASE noise is marginal despite a relatively high CSPR. The launch power, filter CD, incident optical power to the PDs are optimized to 6.2 dBm, -320 ps/nm, and -1 dBm, respectively. Fig. 5.10 shows the BER change as a function of the iteration number for a 56 Gbaud PAM 4 signal with a 2 GHz guard band per sideband. Note that the DDMZM nonlinearity needs to be carefully handled; otherwise, the transmission performance will be significantly compromised. Pre-compensating the DDMZM nonlinearity requires a relatively higher CSPR due to the requirement of zero-DC driving signals and a DDMZM biased at the intensity quadrature. In out setup, 17 dB CSPR is found to optimize the system performance. The launch power, CD of the DCM, incident optical power to the PDs are optimized to 6.2 dBm, -320 ps/nm, and -1 dBm, respectively. As seen in the figure, merely 1 iteration is sufficient in alleviating the impact of the SSBI, achieving a net 112 Gb/s data rate with a pre-forward error correction (FEC) BER below the hard decision (HD)-FEC threshold of 3.8×10^{-3}. Remarkably, the small iteration number could benefit the high-speed parallel implementation of the field recovery DSP.

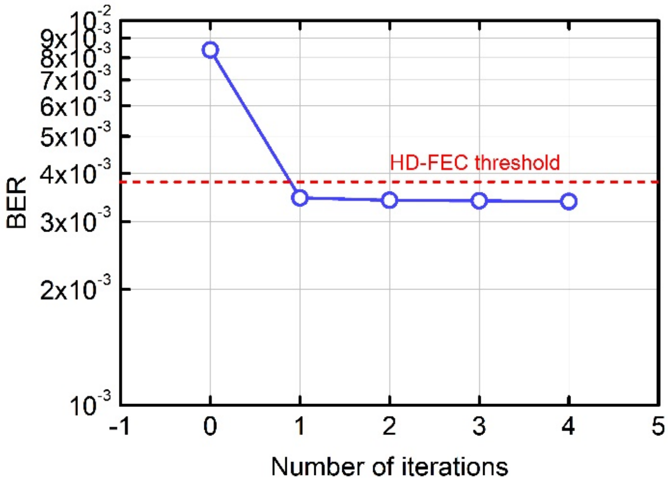

Fig. 5.10. BER versus the number of iterations for a 56 Gbaud PAM 4 signal.

Fig. 5.11 shows the change of the system BER as a function of the incident optical power to the PDs with or without the transmitter nonlinear pre-compensation (NLPC). As seen in the figure, NLPC is required to attain a pre-FEC BER below the HD-FEC threshold of 3.8×10^{-3} in our setup. Further, it is found that the enhanced noise and residual SSBI can be effectively mitigated for SSB PAM 4 signals by use of a post-filter (PF) cascaded with a maximum likelihood sequence estimator (MLSE), which achieves much lower BER.

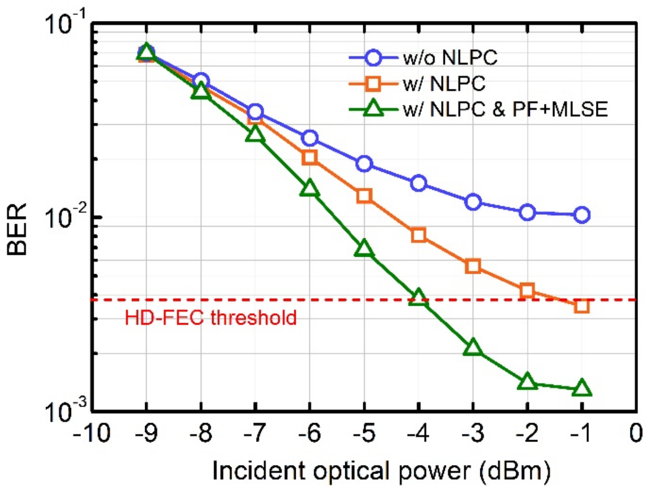

Fig. 5.11 Sensitivity improvement by means of the nonlinear pre-compensation (NLPC) and a post-filter (PF) combined with a maximum likelihood sequence estimator (MLSE).

Fig. 5.12 characterizes the impact of the guard band on the transmission performance with or without PF+MLSE in the postprocessing DSP. We can observe that there exists an optimal guard band and therefore a BER minimum for both curves when the signal is neither severely impacted by the 0 GHz singularity or the second nearest singularity. Furthermore, the use of PF+MLSE significantly reduces the BER because of better suppression of the noise enhancement near 0 GHz.

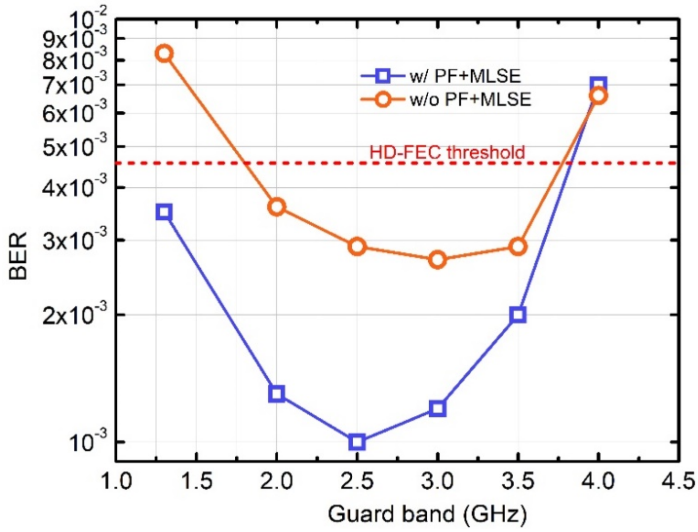

Fig. 5.12 BER change as a function of the guard band.

To explore the attainable throughput of the CD-based ASCDD system, we scale the symbol rate and assume the use of an ideal SD FEC with a code rate of 0.91. One iteration is performed to mitigate the SSBI. Table 5.1 shows the raw bit rate with the CD and guard band optimized accordingly. 200 Gbit/s raw data rate can be achieved over 80 km of SSMF in the C-band. By excluding the overhead, the net data rate is 182 Gbit/s.

Table 5.1. Raw bit rate and the optimized CD and guard band.

Raw Bit rate (Gbit/s)	Optimal CD (ps/nm)	Optimal guard band (GHZ)
140	-250	1.1
160	-200	1.3
170	-160	1.8
180	-135	3.4
200	-100	4.5

5.4. ASCDD systems with a band-rejection filter

In this section, we present a different realization of ASCDD scheme based on a band-rejection filter (BRF), which is a zero-phase filter that suppresses a sideband of the received dual-sideband DSB signal [75]. Fig. 5.13 is a schematic of the BRF-based ASCDD scheme. SC-DSB signals with two independent sidebands are transmitted and detected by the receiver shown in the figure. The SC-DSB signal is split into two portions with the signal portion in the lower branch in the figure filtered into a VSB signal via the BRF.

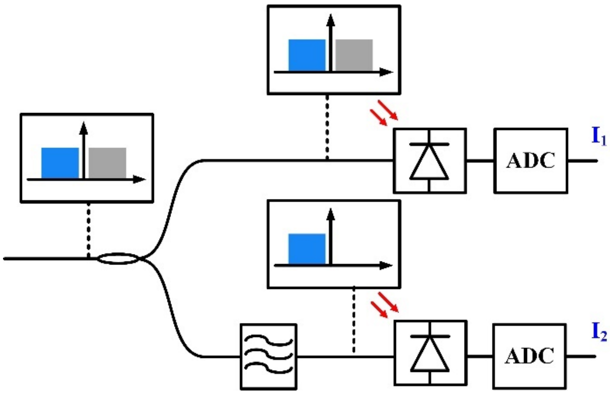

Fig. 5.13 Schematic of the band-rejection filter-based ASCDD scheme. The boxes display the spectra of the signal seen at different positions.

We assume an ideal BRF filter with a step filter response for the field reconstruction expressed as follows:

$$H(\omega) = \begin{cases} 0, \omega < 0 \\ 1, \omega \geq 0 \end{cases} \tag{5.15}$$

Thus, the real and imaginary parts of the signal can be expressed in the frequency domain based on (5.9) and (5.10) , respectively:

$$\hat{S}_I(\omega) = \frac{I_1(\omega) - R_1(\omega)}{2T} \tag{5.16}$$

$$\hat{S}_Q(\omega) = \frac{\left(I_1(\omega) - R_1(\omega)\right)A_E(\omega) - \left(I_2(\omega) - R_2(\omega)\right)}{-2T \cdot jA_O(\omega)} \tag{5.17}$$

where $A_E(\omega)$ and $A_O(\omega)$ are shown below

$$A_E(\omega) = \begin{cases} 1/2, & \omega \neq 0 \\ 1, & \omega = 0 \end{cases} \tag{5.18}$$

$$A_O(\omega) \begin{cases} \text{-1/2}, & \omega < 0 \\ 0, & \omega = 0 \\ 1/2, & \omega > 0 \end{cases} \tag{5.19}$$

Alternatively, the left-sideband (LSB) signal can be reconstructed by means of the KK algorithm, whereas the right-sideband signal can be achieved by subtracting $I_1(t)$ from $I_2(t)$. The cross-sideband beating interference can be mitigated in a similar manner as described in section 5.2. However, note that the optical filter is not ideal rectangular, and the frequency responses of the PDs are not identical in a practical transmission system, and there remains linear crosstalk in the recovered LSB and RSB signal after the iterative SSBI cancellation. This remnant crosstalk is resolved by means of a multi-input-multi-output (MIMO) equalizer in the receiver DSP.

Figure 5.14 shows the experimental setup to test the BRF-based ASCDD scheme. As shown in the transmitter DSP block, two independent sequences of 16-QAM symbols are upsampled to two samples per symbol for pulse shaping via a root-raised-cosine (RRC) filter with a roll-off factor of 0.1. Next, the shaped signal is resampled to the DAC sampling rate of 88 GSa/s and up-converted to an intermediate frequency with a guard band. After pre-emphasis, the in-phase and quadrature signals from the two DAC channels are amplified in order to drive an IQ modulator based at the null point. An external cavity laser (ECL) generates a carrier at 1550.12 nm, which is split into two portions at the transmitter. A variable optical delay line (VODL) and a variable optical attenuator (VOA) in the lower branch are utilized to match the phase of the two carrier portions and tune the carrier-signal power ratio (CSPR), respectively. A polarization controller is used in the upper receiver branch to align the polarizations of the signal and the carrier. The launch power is optimized to 8 dBm by use of an EDFA and a VOA.

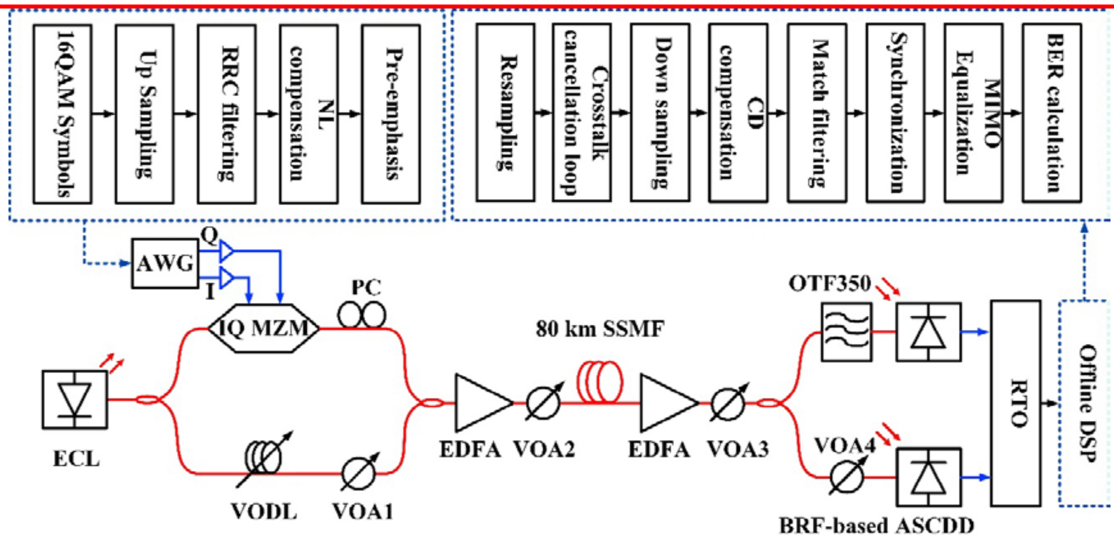

Fig. 5.14. Experimental setup and DSP decks of the transmitter and receiver.

The signal is propagated over 0/80 km and a pre-amplifier along with a VOA are used to adjust the received optical power impinging upon the receiver. The signal is split by use of a 50/50 power splitter and fed to two branches as shown in Fig. 5.14. In the upper branch, the signal goes through a tunable optical filter (Santec OTF350) with a measured edge roll-off of 125 dB/nm in order to remove the RSB. The measured signal spectra before and after the optical filtering are shown in Fig. 5.15. After optical-electrical (OE) conversion, the photocurrents are digitally sampled by a two-channel 8-bit 160 GSa/s real-time oscilloscope (RTO). VOA4 is used to attenuate the optical signal in the lower branch in order to equalize the power into the PDs due to the insertion loss of the optical filter. In the receiver DSP, I_1 and I_2 are resampled to three samples per symbol for the field reconstruction. After down-conversion and down-sampling, the rest of the receiver DSP is implemented, which includes CD compensation, matched filtering, synchronization, MIMO equalization, and BER calculation.

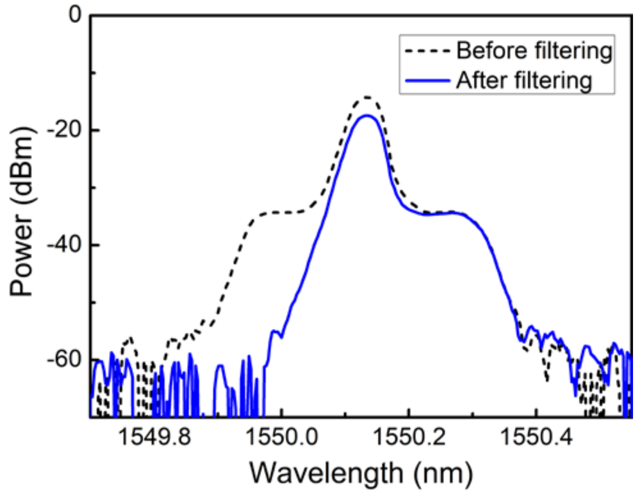

Fig. 5.15. The optical spectra before and after optical filtering.

First, we study the impact of different system parameters in the back-to-back (B2B) configuration. The transmitted signal contains two sidebands each carrying an independent 20 Gbaud 16 QAM signal. Since the intra and inter-sideband SSBIs are mitigated in an iterative manner, a processing delay is incurred which increases with more iterations performed and thereby constrains the throughput of the digital circuit. Thus, we measure the signal SNR versus the iteration number as shown in Fig. 5.16 to determine a suitable number of iterations. It can be seen in this figure that the SNR of the RSB signal increases with an increasing number of iterations due to improved mitigation of the SSBI terms, whereas the SNR change of the LSB is relatively moderate. Assuming that the bits in the LSB and RSB sidebands are interleaved and coded together, the average SNR of the LSB and RSB signal serves as a performance metric. It is seen in the figure that the average SNR initially increases and then levels off when greater than four iterations are performed. Thus, four iterations are used to post-process in the subsequent measurements.

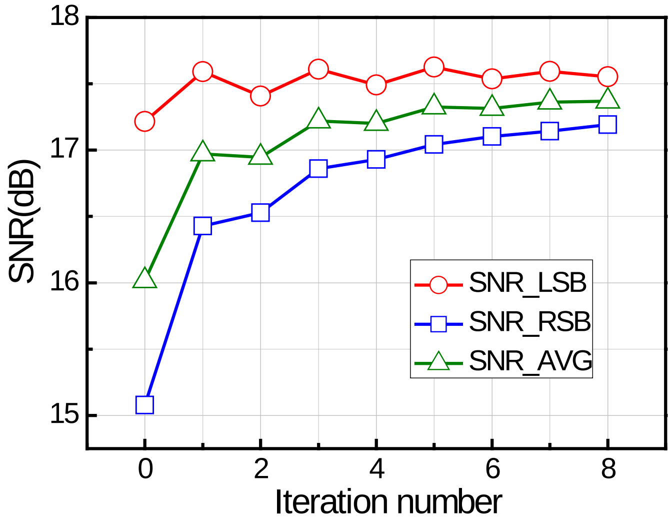

Fig. 5.16. The signal SNR versus the iteration number.

Next, we change CSPR by tuning VOA1 to study how the signal SNR is affected by varied CSPR. Here the CSPR is defined as the ratio between the carrier power and the power of one signal sideband. Fig. 5.17 plots the SNR as a function of CSPR. It is observed that the SNR of the LSB, of the RSB, and the average SNR increase with increasing CSPR and tend to saturate for CSPR greater than 15.8 dB. The increased SNR of the RSB signal at higher CSPR is attributed to a more accurate estimate of the SSBI terms since the linear term as part of the detected RSB signal is stronger compared to the SSBI. On the other hand, the increased SNR for the LSB signal is the consequence of the improved mitigation of the linear crosstalk by use of a MIMO equalizer due to the higher SNR of the RSB signal.

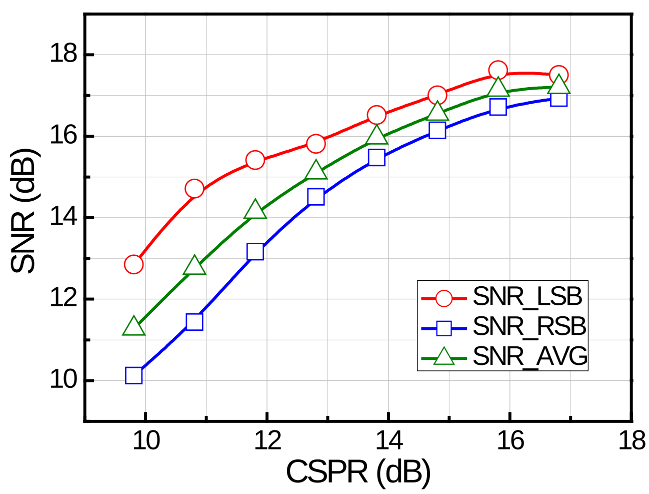

Fig. 5.17. The signal SNR versus the CSPR.

To investigate the achievable spectral efficiency by this approach, we characterize the impact of the roll-off factor of the pulse shaping filter and the size of the guard band on the average signal SNR in Fig. 5.18. As seen from the figure, the average signal SNR increases with an increasing roll-off factor when the guard band size is less than 4 GHz. The explanation is that the excess bandwidth of the signal increases with increasing roll-off factor, thus leading to wider frequency spacing between the LSB and RSB signal within the Nyquist frequency. This contributes to an improved rejection of the RSB signal due to a limited edge roll-off of the optical filter, thus improving the SNR of the reconstructed LSB signal. However, at a guard band size greater than 4 GHz, a greater roll-off factor cannot improve the average signal SNR. This is due to increased ISI induced by the limited bandwidth of the channel and a twin SSB signal with higher bandwidth due to a wider guard band.

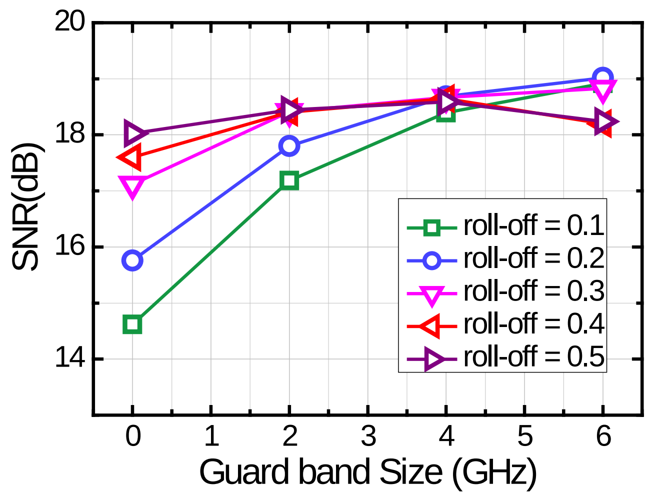

Fig. 5.18. Average signal SNR versus the guard band size.

After characterizing the performance impact from different system parameters at B2B, we conduct a transmission experiment over 80 km of SSMF to explore the attainable capacity using this set-up. Fig. 5.19 shows the measured BER versus the aggregate baud of the 16-QAM twin-SSB signal with the roll-off factor and guard band optimized for each baud listed in the table. CSPR is tuned accordingly to obtain the lowest BER at each baud.

It can be seen in the figure that an aggregate 66 Gbaud 16-QAM signal with an ESE of 6.03 b/s/Hz is transmitted over 80 km below the 0.875 rate HD-FEC threshold. This corresponds to a net data rate of 231 Gbit/s.

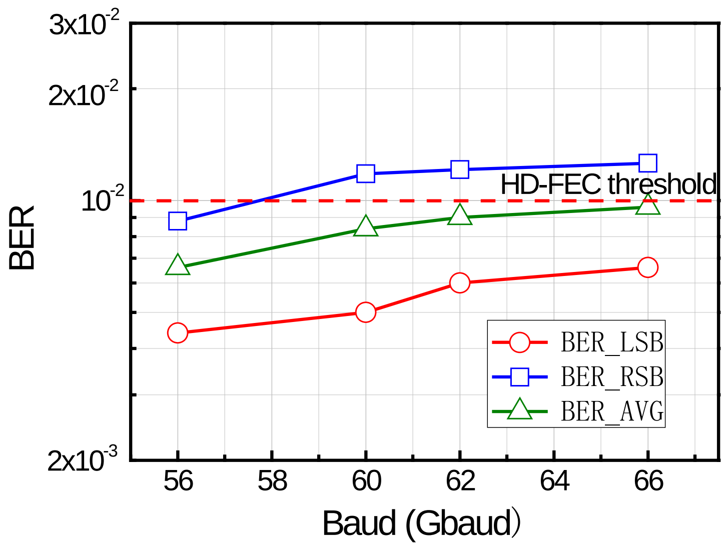

Baud (Gbaud)	roll-off factor	Guard band (GHz)
56	0.2	2
60	0.2	0
62	0.2	0
66	0.1	2

Fig. 5.19. BER versus symbol rate with the roll-off factors and the guard bands listed in the table.

We also numerically study the tolerance of this scheme to the relative wavelength shift of the optical filter, which could be caused by the laser drift or the instability of the filter stabilizer. The parameters in the numerical analysis are chosen according to the equipment used in the experimental setup.

Figure 5.20 plots the average signal SNR as a function of the relative frequency shift Δf of the optical filter for a 16-QAM signal with an aggregate baud of 66 GBaud at B2B. As shown in the inset, a trapezoidal filter is employed in the simulation platform with an edge roll-off of 125 dB/nm as the OTF 350 used in the experiment. It is seen in the figure that the curve has a convex shape and the average signal SNR change is within 0.15 dB with Δf varying from -6 GHz to 0 GHz. This result indicates that the signal SNR is resilient against the frequency drift of lasers, which is normally within 1 GHz for ECL.

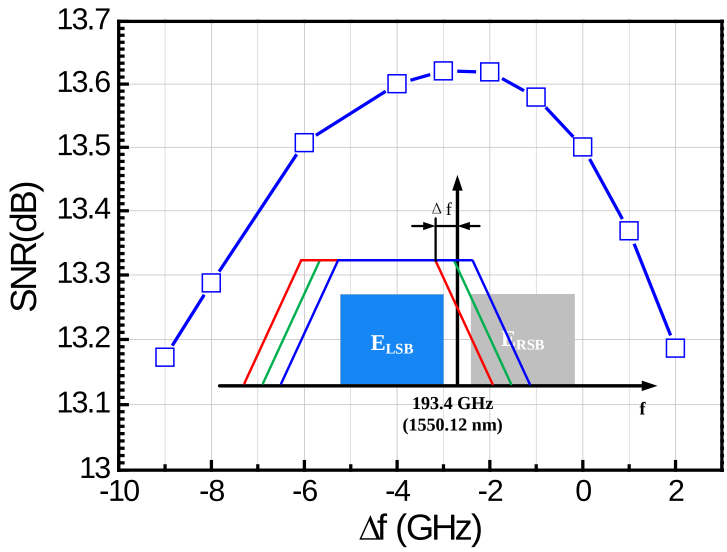

Fig. 5.20. SNR versus Δf. Inset: relative frequency shift of the trapezoidal filter.

5.5. Optimal filter response in ASCDD systems

We have discussed two variations of ASCDD schemes based on either a chromatic dispersion filter or a band-rejection filter. In this section, we analyze the impact of the filter response on the reconstructed signal and derive the optimal filter response that maximizes the signal SNR.

As discussed earlier, the reconstructed signal has a 0 GHz singularity regardless of the form of the filter response. At $\omega \neq 0$, the power spectral density (PSD) of the noise in (5.10) is given as follows

$$F(\omega) = \frac{\left(\left|Q(\omega)\right|^2 + 1\right) N_0}{4T\left|P(\omega)\right|^2} \tag{5.20}$$

where the PSD of N_1 and N_2 are taken as $N_0/2$. To minimize $F(\omega)$ is equivalent to minimizing $\dfrac{\left|Q(\omega)\right|^2 + 1}{4T\left|P(\omega)\right|^2}$, which is denoted as $G(\omega)$. $G(\omega)$ is expanded as follows

$$G(\omega)=\frac{A_E^2(0)\left(A_E^2(\omega)\cos^2(\Phi_E(\omega))+A_O^2(\omega)\sin^2(\Phi_E(\omega))\right)+1}{A_E^2(0)\left(A_E^2(\omega)\sin^2(\Phi_E(\omega))+A_O^2(\omega)\cos^2(\Phi_E(\omega))\right)} \tag{5.21}$$

We can observe that $G(\omega)$ is not affected by the odd part of the phase response, i.e. only the even part of the phase response should be attended to when designing the filter frequency response. In addition, it can be readily shown via a simple partition of (5.21) that $A_E(0)=1$ minimizes $G(\omega)$ for $\omega\neq 0$, which suggests that it is desirable to have an amplitude response of the filter that does not attenuate the CW-tone. We found that $G(\omega)$ has a lower bound of 1 as shown in the appendix. This lower bound is attained if and only if

$$A(\omega)=1 \tag{5.22}$$

$$\Phi(\omega)=\Phi_O(\omega)+\Phi_E(\omega)=\begin{cases}\Phi_O(\omega)+\dfrac{\pi}{2}+k\pi, & \omega\neq 0\\ 0, & \omega=0\end{cases}, \tag{5.23}$$

where *k* takes any integer number. This transfer function indicates that an all-pass filter whose phase response having an even part with a notch near $\omega=0$ is optimal in minimizing the noise in the reconstructed signal. For instance, one of the optimal phase responses is

$$\Phi(\omega)=\begin{cases}\pi, & \omega>0\\ 0, & \omega\leq 0\end{cases} \tag{5.24}$$

which is a step function that inverts the sign of the signal in the positive frequency.

The lower bound of $G(\omega)$ is proven as follows:

Proving that

$$G(\omega)=\frac{\left(A_E^2(\omega)\cos^2(\Phi_E(\omega))+A_O^2(\omega)\sin^2(\Phi_E(\omega))\right)+1}{\left(A_E^2(\omega)\sin^2(\Phi_E(\omega))+A_O^2(\omega)\cos^2(\Phi_E(\omega))\right)}\geq 1 \tag{5.25}$$

is equivalent to proving that

$$\begin{aligned}J(\omega)&=A_E^2(\omega)\left(\cos^2(\Phi_E(\omega))-\sin^2(\Phi_E(\omega))\right)\left(A_E^2(\omega)-A_O^2(\omega)\right)+1\\&=A_E^2(\omega)\cos(2\Phi_E(\omega))\left(A_E^2(\omega)-A_O^2(\omega)\right)+1\geq 0\end{aligned} \tag{5.26}$$

From the definition of the amplitude response, we have the following inequality at $\omega \neq 0$

$$0 \leq A_E(\omega) + A_O(\omega) \leq 1 \tag{5.27}$$

$$0 \leq A_E(-\omega) + A_O(-\omega) \leq 1 \tag{5.28}$$

Due to the property of even and odd functions, (5.28) is equivalent to

$$0 \leq A_E(\omega) - A_O(\omega) \leq 1 \tag{5.29}$$

The addition and multiplication of (5.27) and (5.29) leads to the bounding conditions as follows

$$0 \leq A_E^2(\omega) - A_O^2(\omega) \leq 1 \tag{5.30}$$

$$0 \leq A_E(\omega) \leq 1 \tag{5.31}$$

Thus, $J(\omega) \geq -\left(A_E^2(\omega) - A_O^2(\omega)\right) + 1 \geq 0$ and $G(\omega)$ is lower bounded by 1. The equality is achieved when $\cos\left(2\Phi_E(\omega)\right) = -1$, $A_E^2(\omega) = 1$, and $A_O^2(\omega) = 0$, which leads to the all-pass filter response expressed in (5.22) and (5.23).

5.6. ASCDD systems based on Mach-Zehnder interferometers

In this section, we discuss a different ACSDD scheme based on Mach-Zehnder interferometers (MZI). Similar to the ASCDD schemes discussed earlier, the ACSDD-MZI scheme allows the field reconstruction of SC-DSB signals using a cost-effective DD receiver having two branches. Note that the optical filter is eliminated due to the use of an MZI in the receiver. The incident SC-DSB signal in an ACSDD-MZI scheme is split into two parts, one of which is delayed and beats with the other part when detected at the cross and bar outputs of an MZI. We will show in the sequel that the sum and difference of the two tributaries of photocurrents can be exploited to reconstruct the complex field of complex DSB signals. In addition, we will discusss a modified ACSDD-MZI scheme, referred to as ACSDD-AUX due to an auxiliary DD branch used to improve the SNR of the reconstructed signal.

In order to illustrate the principle of the ACSDD-MZI scheme, we depict in Figure 5.21 a schematic of a symmetric DD receiver with two PDs and an MZI. The PDs detect the cross and bar outputs of the MZI, which is biased at the intensity quadrature. An incoming SC-DSB signal as shown in the figure can be formulated as $E(t)=T+s(t)$, where T is a CW-tone, and $s(t)$ is a complex DSB signal. Based on the symmetry of the receiver structure and the conservation of energy, the sum and difference of the photocurrents are expressed as follows:

$$i_1(t)+i_2(t)=\eta\left|T+s(t)\right|^2=\eta\left(T^2+2T\,\mathrm{Re}\left(s(t)\right)+\left|s(t)\right|^2\right), \tag{5.32}$$

$$i_1(t)-i_2(t)=0, \tag{5.33}$$

where η is the responsivity and set to 1 in the following analysis without loss of generality. Thus, the real part of the signal can be extracted from the Tone-signal beating term $2T\,\mathrm{Re}\left(s(t)\right)$ based on (5.32).

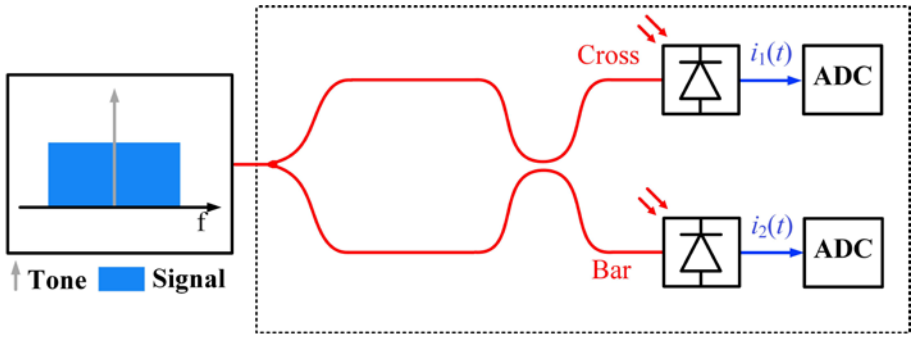

Fig. 5.21. Schematic of a symmetric DD receiver based on an MZI.

In order to extract the imaginary part of the signal, we break the symmetry of this structure by adding a delay element in one of the MZI arms and refer to this new structure as the ACSDD-MZI scheme. Fig. 5.21 shows a schematic of the ACSDD-MZI scheme. Since the PDs detect the beating between a signal and its delayed copy, the photocurrents difference is nonzero, which provides additional information for the retrieval of the imaginary part.

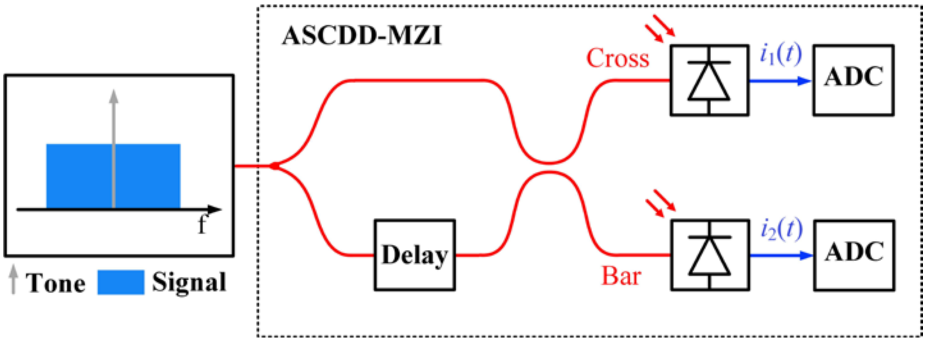

Fig. 5.22. Schematic of an ASCDD receiver based on an MZI.

The photocurrents $i_1(t)$ and $i_2(t)$ can be expressed as follows

$$\begin{aligned} i_1(t) &= \frac{1}{4}\left|\left(T+s(t)\right)+j\left(T+s(t-\tau)\right)\right|^2 \\ &= \frac{1}{4}\begin{pmatrix} T^2+2T\,\mathrm{Re}\left(s(t)\right)+\left|s(t)\right|^2 \\ +T^2+2T\,\mathrm{Re}\left(s(t-\tau)\right)+\left|s(t-\tau)\right|^2 \\ -2\,\mathrm{Re}\left(\left(T+s(t)\right)j\left(T+s^*(t-\tau)\right)\right) \end{pmatrix}, \end{aligned} \tag{5.34}$$

$$\begin{aligned} i_2(t) &= \frac{1}{4}\left|\left(T+s(t)\right)-j\left(T+s(t-\tau)\right)\right|^2 \\ &= \frac{1}{4}\begin{pmatrix} T^2+2T\,\mathrm{Re}\left(s(t)\right)+\left|s(t)\right|^2 \\ +T^2+2T\,\mathrm{Re}\left(s(t-\tau)\right)+\left|s(t-\tau)\right|^2 \\ +2\,\mathrm{Re}\left(\left(T+s(t)\right)j\left(T+s^*(t-\tau)\right)\right) \end{pmatrix}, \end{aligned} \tag{5.35}$$

where τ represents the delay in the ACSDD scheme. Adding $i_1(t)$ and $i_2(t)$ results in the sum

$$\begin{aligned} i_1(t)+i_2(t) &= \frac{1}{2}\begin{pmatrix} 2T^2+2T\,\mathrm{Re}\left(s(t)\right)+2T\,\mathrm{Re}\left(s(t-\tau)\right) \\ +\left(\left|s(t)\right|^2+\left|s(t-\tau)\right|^2\right) \end{pmatrix}, \\ &= T^2+T\left(s_I(t)+s_I(t-\tau)\right)+u_1(t)+u_1(t-\tau) \end{aligned} \tag{5.36}$$

where $u_1(t)$ denotes the signal-signal beating interference (SSBI) term $1/2\left|s(t)\right|^2$. It is found from (5.36) that the sum of the photocurrents can still be exploited to extract the real part of the signal despite a different form compared to (5.32). Due to the introduced delay in the MZI structure, subtracting $i_1(t)$ from $i_2(t)$ leads to a nonzero difference below

$$\begin{aligned} i_1(t)-i_2(t) &= \text{-}\mathrm{Re}\Big(\big(T+s(t)\big)\, j\big(T+s^*(t-\tau)\big)\Big) \\ &= \mathrm{Im}\begin{pmatrix} T^2+T\big(s(t)+s^*(t-\tau)\big) \\ +s(t)s^*(t-\tau) \end{pmatrix} \\ &= T\big(s_Q(t)-s_Q(t-\tau)\big)+u_2(t) \end{aligned}, \tag{5.37}$$

where $u_2(t)$ denotes the SSBI term $\mathrm{Im}\big(s(t)s^*(t-\tau)\big)/T$. Based on (5.36) and (5.37), the real and imaginary parts of the signal can be reconstructed in the frequency domain as follows

$$S_I(\omega)=\frac{I_1(\omega)+I_2(\omega)-2\pi T^2\delta(\omega)}{T\left(1+e^{-j\omega\tau}\right)}-\frac{U_1(\omega)}{T}, \tag{5.38}$$

$$S_Q(\omega)=\frac{I_1(\omega)-I_2(\omega)-U_2(\omega)}{T\left(1-e^{-j\omega\tau}\right)}. \tag{5.39}$$

Thus, the signal $S(\omega)$ can be expressed in the frequency domain as $S_I(\omega)+jS_Q(\omega)$. Note that (5.38) and (5.39) contain the transfer functions $H_I=1\big/\big(1+\exp(\text{-}j\omega\tau)\big)$, and $H_Q=1\big/\big(1-\exp(\text{-}j\omega\tau)\big)$, respectively, which results in a sequence of equally spaced singularities located at $\omega=k\pi/\tau$ in the reconstructed $S(\omega)$, where k takes any integer numbers. In addition, we can observe from (5.38) and (5.39) that the singularities of H_I do not enhance the SSBI term $U_1(\omega)$, whereas the singularities of H_Q enhances the SSBI term $U_2(\omega)$.

In the ACSDD-MZI scheme, the SSBI is mitigated iteratively similar to what is described in section 5.2 except that the SSBI terms take different forms. A schematic of the iterative SSBI cancellation scheme is depicted in Fig. 5.3. The first iteration reconstructs S(ω) without mitigating the SSBI terms. The signal estimate is fed back for the SSBI estimates, which are subtracted from the sum and difference of the signal. Thus after a second iteration, the reconstructed signal has improved SNR due to alleviated SSBI. This algorithm is performed iteratively until the impact of the SSBI is marginal compared to other sources of SNR degradation in the system.

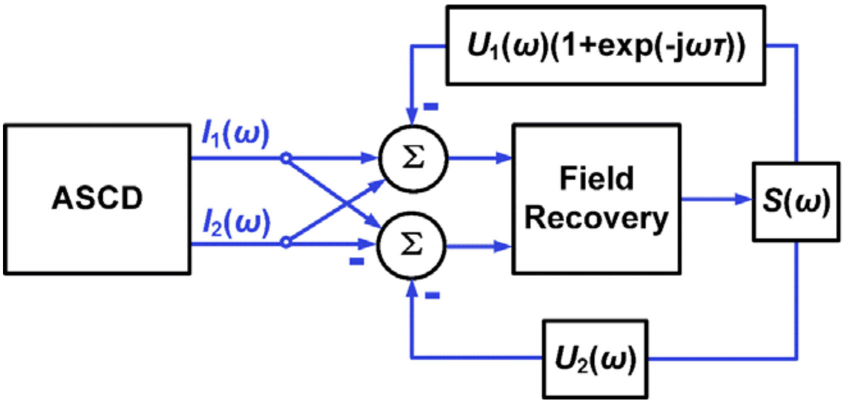

Fig. 5.23. Iterative SSBI cancellation algorithm.

We proceed to assess the transmission performance of the ACSDD-MZI scheme. Fig. 5.24 shows the magnitude response of H_I and H_Q with a 16 ps delay. The singularities are equally spaced in the spectrum such that the signal bands need to be allocated within the spectral intervals partitioned by the singularities. Thus, the delay in the ACSDD-MZI scheme needs to be optimized to suitably accommodate the signal in order to minimize the performance penalty resulting from the singularities.

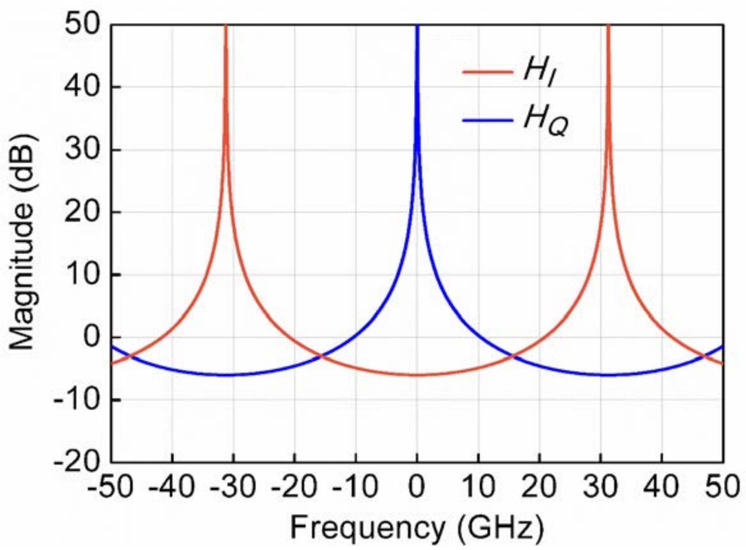

Fig. 5.24. Magnitude response of HI and HQ at a delay of 16 ps.

First, we numerically assess the performance impact of the critical system parameters. We assume a relatively simple signaling scheme where the signal is comprised of two independent sidebands (ISB), each of which carries a 25 Gbaud 16 QAM signal. A CW-tone co-propagates with the signal over 40 km of SSMF, which is assumed lossless and has a dispersion coefficient of 17 ps/nm/km. AWGN is linearly added to the signal to simulate the additive spontaneous noise (ASE) for the performance evaluation. After direct detection, electrical noise from the PD and the ADC is added to the signal quantitatively based on the definition of the electrical signal-to-noise ratio (SNRe) expressed as $\left\langle \left(s(t)\text{-}\left\langle s(t)\right\rangle\right)^2 \right\rangle \Big/ \left\langle n^2(t)\right\rangle$, where $\left\langle x\right\rangle$ represents the time-domain average of x, $s(t)$ is the signal, and n(t) is the electrical noise. SNRe is set to 30 dB by adding AWGN to the photocurrents. In addition, brick-wall filters are used to simulate the electrical bandwidth of the PDs and ADCs in the receiver, which is configured to pass only the tone-signal beating terms in (5.34) and (5.35) while rejecting the out-of-band noise and interferences.

The SSBI enhancement due to the singularities of H_I and H_Q can be visualized from the SSBI spectra in Fig. 5.25 at two different delays after reconstructing the signal based on (5.38) and (5.39), and subsequently removing the signal. It is seen from this figure that at a 16 ps delay, the spectral enhancement at 0 GHz due to H_Q is much stronger compared to the spectral enhancement at 31.25 GHz due to H_I. The explanation is that H_Q enhances the SSBI term at 0 GHz, whereas H_I enhances only the electrical noise at 31.25 GHz. At a shorter delay of 10 ps, the frequency interval between the 0 GHz singularity and the nearest singularities, i.e. k = 1, increases, which allows signal bands with higher bandwidth. However, the enhancement caused by the 0 GHz singularity is more pronounced at a shorter delay in the MZI, which requires a wider guard band in order to alleviate the impact of this singularity.

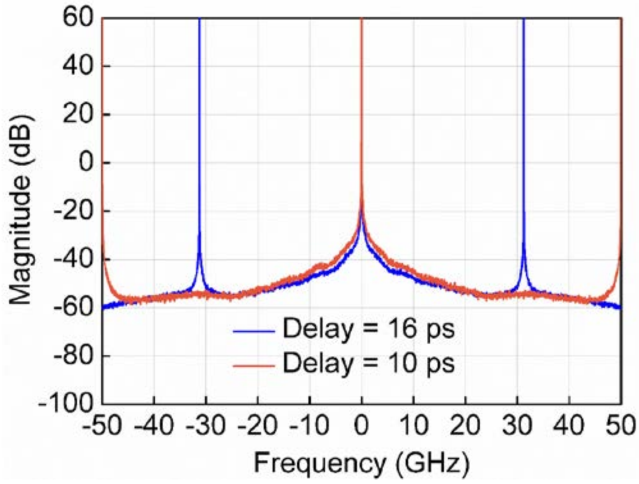

Fig. 5.25. Spectra of the SSBI after reconstructing the signal and removing the signal at delays of 10 ps and 16 ps, respectively.

Due to this, we study the impact of the delay on the system performance. The CSPR is set to 9 dB, and the guard band between the edge of the signal sideband and the CW-tone is set to 2 GHz. Fig. 5.26 shows the BER versus OSNR at different delays. As seen from the figure, 16 ps delay achieves the lowest BER among all delays. A higher delay of 18 ps leads to a substantially higher BER because the singularities corresponding to k=1 move within the signal sidebands. When a delay lower than 16 ps is applied in the ACSDD-MZI scheme, the system performance deteriorates due to a stronger enhancement of the SSBI near 0 GHz as explained earlier.

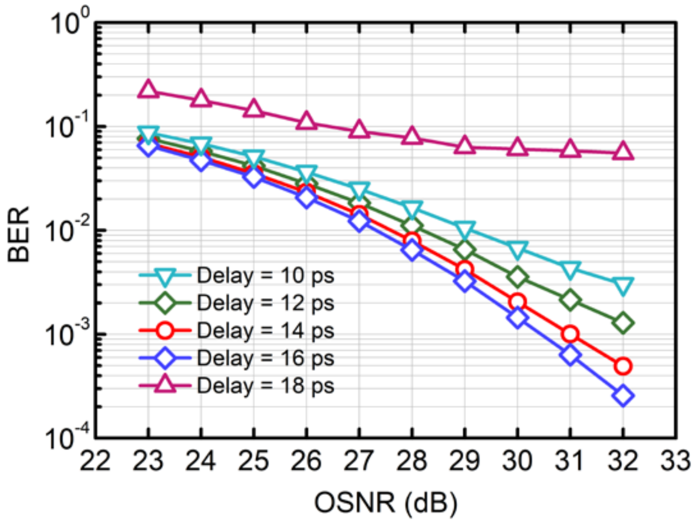

Fig. 5.26. BER vs. OSNR at varied delay of 10, 12, 14, and 16 ps.

Next, we investigate the number of iterations required to mitigate the SSBI terms. Since the algorithms are often implemented using pipelined sequential logic circuits for a high circuit throughput, more iterations incur higher circuit latency and require more registers, which leads to higher power consumption. Thus, it is desirable to determine the least number of iterations required to effectively mitigate the SSBI. Fig. 5.27 plots the BER as a function of the number of iterations at varied OSNRs. It can be seen from the figure that the BER decreases and then levels off as more iterations are performed. Moreover, the number of iterations to attain the BER floor increases as the OSNR increases. At a lower OSNR, a fewer number of iterations are required to render the residual SSBI marginal compared to the noise, whereas at a higher OSNR, more iterations are needed in order to mitigate the residual SSBI more sufficiently. As a suitable trade-off between the BER and the digital processing delay, we use 4 iterations to mitigate the SSBI in the following postprocessing DSP.

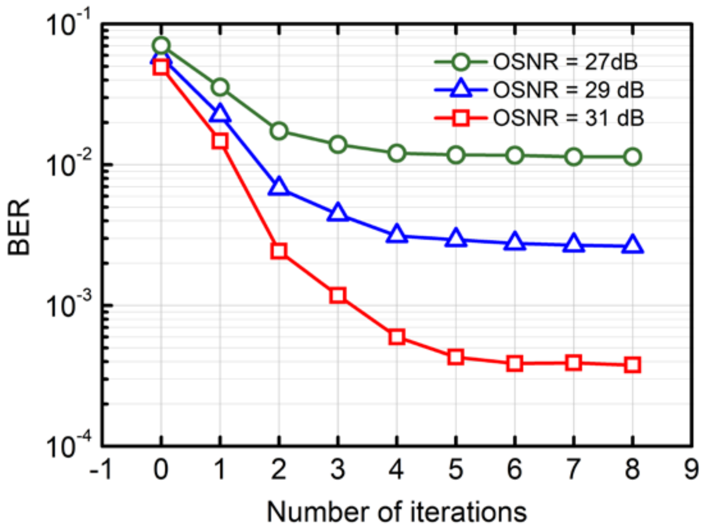

Fig. 5.27. BER vs. number of iterations at varied OSNRs.

At an OSNR of 29 dB, we plot the spectra of the SSBI in Fig. 5.28 after different iterations of SSBI cancellations. The figure shows that as the number of iterations increases, the SSBI is mitigated progressively. This is in agreement with the principle of the iterative SSBI cancellation algorithm discussed above. In particular, the enhanced SSBI near 0 GHz is significantly suppressed after 4 iterations of SSBI removal, which allows for signal sidebands with a narrower guard band and higher ESE.

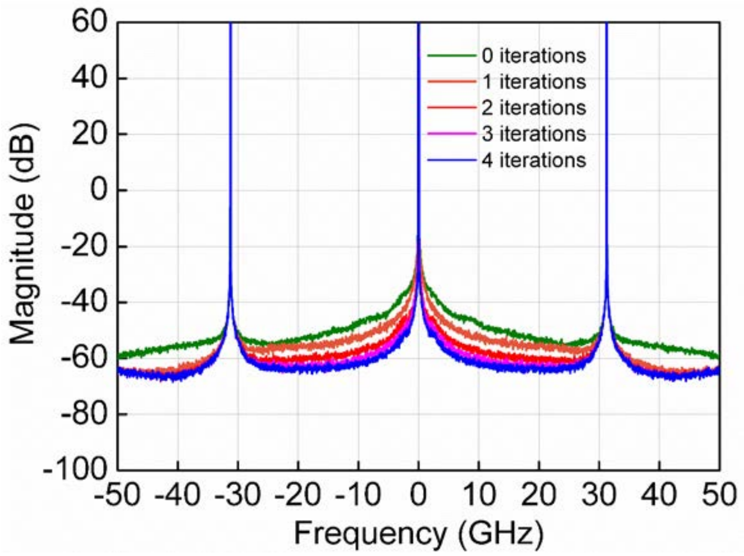

Fig. 5.28. BER vs. number of iterations at varied OSNR values.

Next, we study the impact of the CSPR and the guard band at an OSNR of 29 dB. Figure 5.29 plots the BER as a function of the CSPR at varied guard bands. The figure shows that as the CSPR increases, the BER decreases till reaching a BER minimum and then increases. The inflection points are due to the trade-off between the SSBI mitigation efficacy and the signal SNR. More specifically, at a lower CSPR, the SSBI estimates are less accurate because the reconstructed signal is more degraded by the enhanced SSBI. On the other hand, at a higher CSPR, the signal is noisier at a given OSNR because the CW-tone power is also part of the signal power in the calculation of the OSNR. Thus, the BER minimum is reached when a proper balance is achieved for this trade-off. In addition, we observe from the figure that the size of the guard band affects the optimal CSPR for the BER minimum. A lower CSPR is preferred at a wider guard band, because the signal is less impacted by the enhanced SSBI near 0 GHz and a higher power margin is allowed for the signal. It is also found that a slightly wider guard band can significantly reduce the BER.

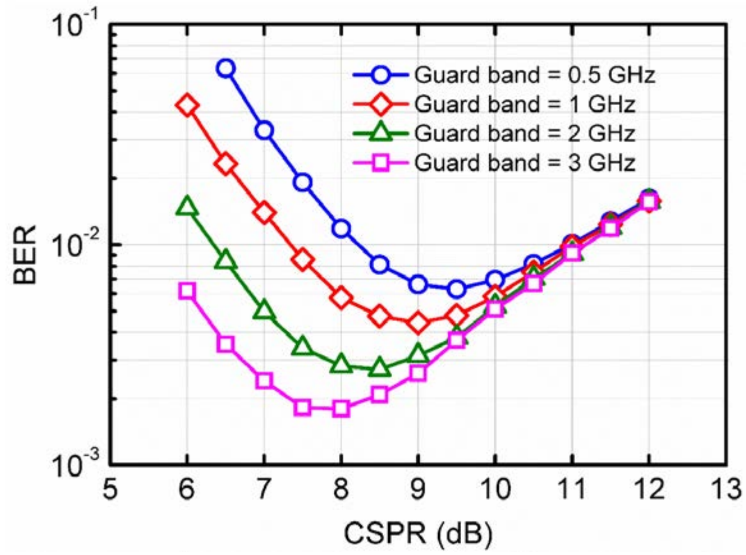

Fig. 5.29. BER vs. number of iterations at varied OSNRs.

Next, we show that the performance of ACSDD-MZI can be improved at the expense of a slightly more complex receiver structure. Fig. 5.30 depicts the modified ACSDD-MZI scheme. An auxiliary DD branch is introduced to recover the real part of the incident signal and we refer to this modified scheme ACSDD-AUX. In addition, the two PDs in the ACSDD-MZI scheme are connected in series for balanced detection and cancel the photocurrents without a need for digital subtraction. Thus, only one more PD is required in terms of the hardware complexity compared to the original ACSDD-MZI scheme.

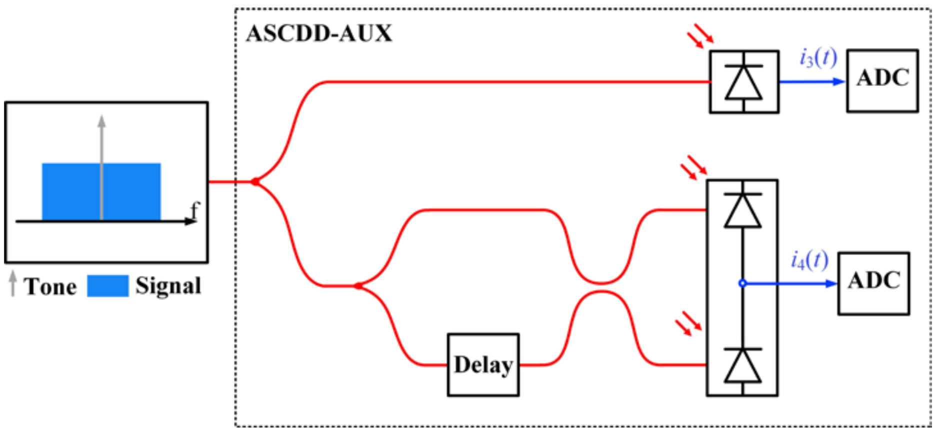

Fig. 5.30. Schematic of the ACSDD scheme with an auxiliary DD branch.

The photocurrents $i_3(t)$ and $i_4(t)$ can be expressed as

$$
\begin{aligned}
i_3(t) &= \frac{1}{2}\left(T^2 + 2Ts_I(t) + \left|s(t)\right|^2\right) \\
&= \frac{1}{2}T^2 + Ts_I(t) + u_1(t)
\end{aligned}
\tag{5.40}
$$

$$
i_4(t) = \frac{1}{2}\left[i_1(t) - i_2(t)\right] \tag{5.41}
$$

Thus, the imaginary and real parts of the signal can be expressed as follows

$$
S_I(\omega) = \frac{I_1(\omega) - U_1(\omega)}{2T} \tag{5.42}
$$

$$
S_Q(\omega) = \frac{I_2(\omega) - U_2(\omega)}{T\left(1 - e^{-j\omega\tau}\right)} \tag{5.43}
$$

Equation (5.42) and (5.43) for the signal reconstruction has a simpler form compared to (5.38) and (5.39) since the transfer function H_I is eliminated, and the allocation of the signal band is determined only by H_Q. Thus, the singularities of the ACSDD-AUX scheme are distributed at $\omega = 2k\pi/\tau$ with a doubled spacing compared to the ACSDD-MZI scheme at a given delay. Fig. 5.31 compares the transfer function H_Q at 16 ps and 32 ps delay, respectively. It follows that stronger SSBI enhancement near 0 GHz should be induced by H_Q at 16 ps of delay compared to H_Q at 32 ps of delay.

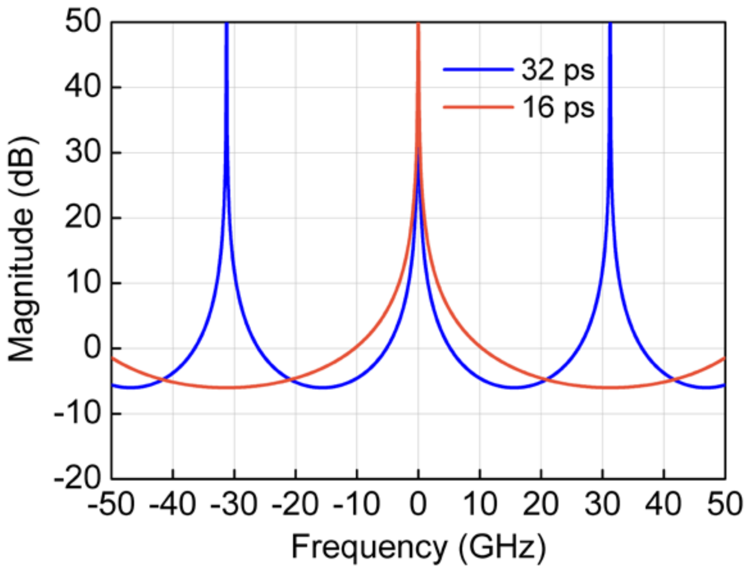

Fig. 5.31. Magnitude response of HQ at delays of 16 ps and 32 ps.

In order to compare the enhanced noise and SSBI between the ACSDD-MZI and the ACSDD-AUX schemes, we plot the SSBI spectra as shown in Fig. 5.32. It is seen from the figure that the SSBI enhancement is less pronounced for the ACSDD-AUX scheme near 0 GHz due to a higher delay of 32 ps. However, the singularities of H_Q induce stronger SSBI enhancement at 31.25 GHz compared to H_I because H_I only enhances the electrical noise from the PD and the ADC.

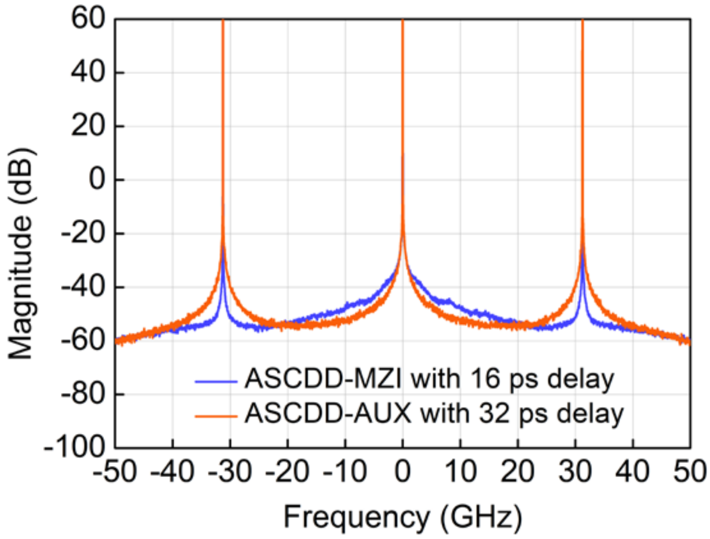

Fig. 5.32. Spectra of the enhanced SSBI after a first signal field reconstruction for the ACSDD-MZI and ACSDD-AUX schemes.

We also compare the spectra of the residual SSBI after 4 iterations of SSBI cancellation in Fig. 5.33. As seen from the figure, ACSDD-MZI has stronger SSBI enhancement near 0 GHz due to H_Q with a lower delay, whereas at the other two singularities, the two schemes achieve close enhancement in the spectrum because H_Q in the ASCDD-AUX scheme has a higher delay, whereas H_I in the ASCDD-MZI scheme does not enhance the SSBI. Thus, the figure indicates that the ACSDD-AUX scheme is less affected by the enhanced SSBI near 0 GHz compared to the ACSDD-MZI scheme due to the auxiliary DD branch.

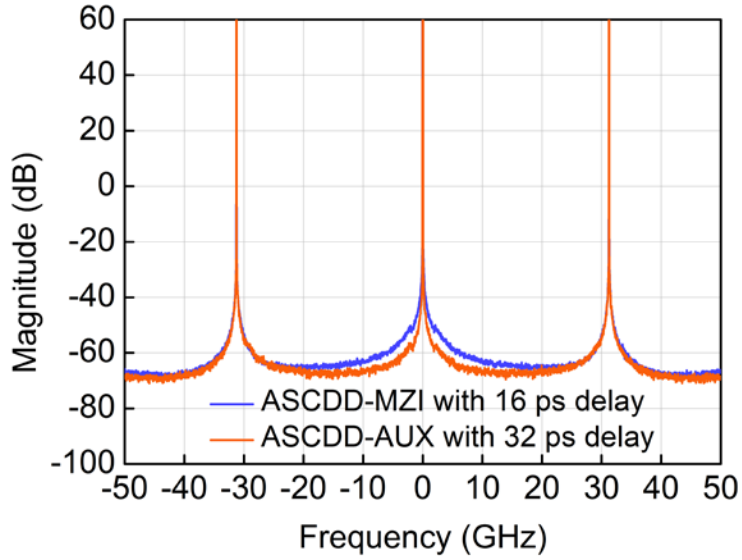

Fig. 5.33. Spectra of the noise and the residual SSBI after 4 iterations of SSBI cancellation.

Next, we compare the OSNR sensitivity of different self-coherent direct-detection schemes in the back-to-back configuration (B2B). Fig. 5.34 plots the BER as a function of the OSNR for the ASCDD-MZI scheme, the ASCDD-AUX scheme, and the CADD scheme at varied guard bands with optimized delays to accommodate the signal. 4 iterations of SSBI mitigation are implemented for these SC-DSB-DD schemes. Note that the SSBI estimates are obtained from the reconstructed signal field as detailed in section II, which is different from the approach adopted in where the SSBI estimates are based on clean symbols determined after equalization at the expense of higher complexity. In addition, we include the OSNR sensitivity of the KK scheme in this figure. For a fair comparison, we transmit a 50 Gbaud single-sideband 16 QAM signal in the KK scheme and an aggregate 50 Gbaud dual-sideband 16 QAM signal in the ASCDD schemes, and the CADD scheme. Due to the spectral expansion induced by nonlinear operations used in the KK scheme, a relatively higher sampling rate of 200 GSa/s is set for the KK scheme, whereas a lower sampling rate of 100 GSa/s is set for the SC-DSB-DD schemes. In addition, brick-wall filters are used to simulate the electrical bandwidth of the PDs and ADCs and are configured to pass only the tone-signal beating term in all schemes considered. Note that no electrical noise is added at the receiver in the OSNR sensitivity analysis. Due to the trade-off between the ASE noise and the SSBI, the CSPR is optimized at each OSNR. In order to relax the requirement for the remote wavelength management and even allow the use of uncooled lasers, no narrow bandpass optical filter is used after demultiplexing in the CWDM system to remove the out-of-band ASE noise of the optical signal.

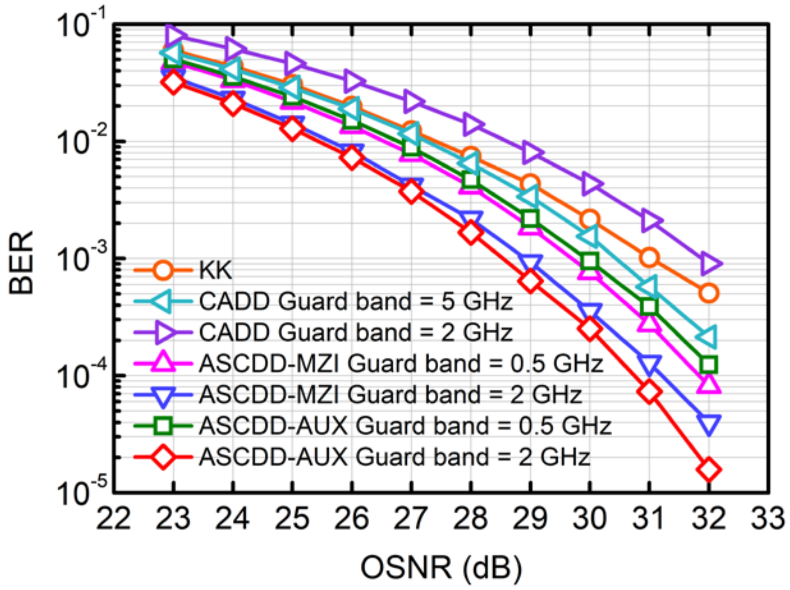

Fig. 5.34. OSNR sensitivity for different self-coherent direct-detection schemes.

The figure shows that the ASCDD schemes and the CADD scheme can achieve lower BER compared to the KK scheme at sufficiently wide guard bands used to effectively mitigate the enhanced SSBI near 0 GHz. The worse OSNR sensitivity of the KK scheme is due to the ASE noise from the image sideband that beats with the CW-tone after detection, thus resulting in degraded SNR of the baseband signal. We also note that the SC-DSB-DD schemes discussed here require approximately half of the electrical bandwidth relative to the KK scheme. At the same guard band of 2 GHz, it is observed that both ASCDD schemes achieve significantly lower BER compared to the CADD scheme. The explanation is that the power of the SSBI term $u_3(t)=s(t)s^*(t-\tau)-|s(t-\tau)|^2$ in the CADD scheme is stronger compared to $u_2(t)=\mathrm{Im}\left(s(t)s^*(t-\tau)\right)$ in the ASCDD schemes, which can be visualized from the spectra of these two SSBI terms in Fig. 5.35. Since $u_2(t)$ and $u_3(t)$

are enhanced by the same transfer function $H_Q(\omega)$ near 0 GHz, the residual SSBI in the CADD scheme is more pronounced after the iterative SSBI cancellation and leads to lower OSNR sensitivity when the same guard band is used. It is also found that the ASCDD-AUX scheme performs slightly better than the ASCDD-MZI scheme, achieving the lowest BER among the three SC-DSB-DD schemes. In terms of the hardware complexity, the ASCDD-AUX scheme eliminates the use of two extra PDs and one ADC compared to the CADD scheme but requires one more PD compared to the ASCDD-MZI scheme.

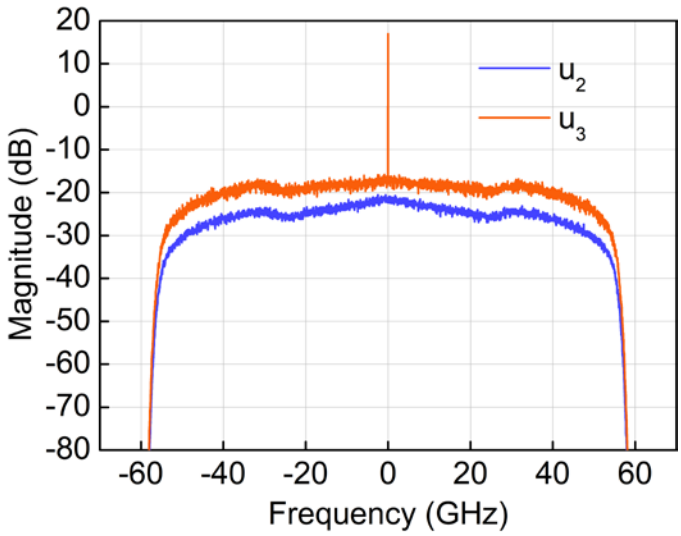

Fig. 5.35. Spectra of the SSBI terms $u_2(t)$ and $u_3(t)$.

5.7. Discussion and conclusions

In this chapter, we discuss various types of ASCDD schemes that increase the ESE by a factor of two compared to SC-SSB-DD schemes. We show both numerically and experimentally that the ASCDD scheme can use either a band-rejection filter or a CD filter in the receiver subsystem to reconstruct 200 Gb/s SC-DSB signals. We find that the optimal filter response is an all-pass filter whose phase response consists of an even part having a notch at 0 GHz. In addition, we show numerically that an MZI-based ASCDD scheme can enable the field reconstruction of SC-DSB signals based on the beating of a signal and its delayed copy. We note that both the ASCDD and the ASCDD-MZI scheme combine a cost-effective and phase-diverse DD receiver with a high ESE approaching that of the homodyne coherent detection in a single-polarization configuration.

In order to evaluate the hardware complexity of different SCDD schemes, we consider the bandwidth of PDs and ADCs, the number of PDs and ADCs, the need for LOs as the major cost metrics. This is due to the following reasons: (a) high-speed PDs and ADCs are costly, (b) using more PDs and ADCs requires a higher received optical power to the receiver and a larger footprint, and (c) the need for a LO requires more stringent remote wavelength stabilization and the implementation of carrier phase recovery DSP, thus increasing the power consumption and system complexity. Table 5.2 compares the hardware complexity of different coherent detection schemes assuming a signal with the same bandwidth B.

Table 5.2. Hardware complexity of different detection schemes in a single-polarization configuration.

Schemes	PD/ADC bandwidth	No. of ADCs	No. of PDs	No. of LOs
KK	B	1	1	0
CADD	~B/2	3	5	0
ASCDD	~B/2	2	2	0
ASCDD-MZI	~B/2	2	2	0
Coherent	B/2	2	4	1

The table shows that the KK receiver requires the highest receiver electrical bandwidth B among all the detection schemes considered due to an unused image band. Though CADD reduces the bandwidth of PDs and ADCs by a factor of 2, the scheme requires an additional optical hybrid, two more ADCs, and 4 more PDs (2 BPDs), which significantly increases the receiver complexity and requires higher received optical power. By comparison, both the ASCDD and the ASCDD-MZI schemes use the least number of PDs and ADCs and require an electrical bandwidth close to half of that required by the KK scheme. Furthermore, the band-rejection filter and CD-filter-based ASCDD schemes can be implemented using mature optical components. Sharp edge band-rejection filter can be realized using cascaded ring-resonators, whereas grating-based devices can serve as CD filters, which can provide the required CD for multiple channels [128-130]. We also note that the ASCDD-MZI scheme is simple to implement by use of a delay line MZI in a two-branch DD receiver such that the beating between an SC-DSB signal and its delayed copy is available for the signal reconstruction. To summarize, the ASCDD schemes discussed in this chapter combine the high ESE and phase-diversity of homodyne coherent detection with the cost-effectiveness of DD systems, which holds potential for high capacity short-reach data center communications up to 40 km.

6 Conclusions and future work

6.1 Summary

The fast development of data-intensive services such as video streaming, cloud computing, and enhanced reality fuel the growth of the IP traffic in the data center network. An explicit trend in the development of high-capacity transceivers for data center communications is the adoption of a compact form factor, i.e. QSFP-DD because of the advantages of backward compatibility and a high port density. Though the compactness of QSFP-DD is favorable for rack switches to achieve high throughput, a tight power consumption limit is imposed in the system design due to the constraints of thermal cooling techniques. DCO systems have high throughput and high spectral efficiency as manifested in metro to long haul optical communications and are migrating to application use cases at increasingly shorter reach. However, the high power consumption that comes along with the superior performance of DCO systems renders it debatable to deploy pluggable DCO transceivers for less than 40 km of distance. On the other hand, DD systems are attractive for short-reach data center connections due to low cost and power consumption. The main deficiency of conventional DD systems is much lower throughput compared to DCO systems and the challenge to fulfill use cases beyond 10 km of reach especially at higher baud, which can be readily reached by DCO transceivers. Despite a trend to simplify DCO systems for shorter reach connections, there is also the motivation to combine the advantages found in DCO systems with the cost-effectiveness of DD systems, forming advanced DD systems discussed in the thesis for the intra- and inter-data center connections up to 40 km of reach. More specifically, we have presented the following content in this thesis.

In chapter 1, we provided background and context for the problem addressed in the thesis. Next, we defined the boundary of the problem and outlined the approaches that we took to design advanced DD systems having high throughput and spectral efficiency for the data center connections up to 40 km. We also described the organization of the thesis and highlight our contributions in each chapter.

In chapter 2, we presented the fundamentals of the thesis, i.e. concepts, techniques, and underlying physics that the subsequent chapters are built upon. We mainly reviewed two DD systems, i.e. the conventional IMDD systems and the SC-SSB-DD systems that recently emerged. We covered most of the important knowledge of these two systems required to understand the following chapters.

In chapter 3, we discussed how probabilistic shaping, a technique widely used in DCO systems could be appropriately integrated into IMDD systems. We detailed the integration of a short-block length distribution matcher CMDM into IMDD systems for power-efficient and low-latency probabilistic shaping. Using CMDM, we reported a first net 800 Gb/s CWDM system over 2 km in the O-band using an EML TOSA. We also presented a neural network-based method to optimize the input distribution of PS symbols in practical IMDD systems for 800 G intra-data center connections.

In chapter 4, we focused on a DD system, i.e. SC-SSB-DD systems having greater throughput-distance than IMDD systems. We described two different approaches to generating wideband SC-SSB signals having a negligible image band for 800 G connections beyond 40 km of reach based on a pair of RF signals with a constant phase difference. A distinct advantage of such signal generation schemes is the potential to remove the optical amplifier for reduced system power consumption. In addition, we detailed an approach to realize polarization multiplexed SC-SSB-DD systems and achieve > 300 G throughput per wavelength beyond 40 km.

In chapter 5, we introduced novel DD systems referred to as ASCDD systems for the reception of SC-DSB signals that increase the electrical spectral efficiency by a factor of 2 compared to SC-SSB-DD systems. We characterized the theoretical performance of the proposed systems and validated its working principle in a test bench having > 200 Gb/s throughputs over 80 km. We also discussed other variants of ASCDD systems having a CD filter or an MZI in the receiver subsystem.

6.2 Future work avenues

Though the objectives of the thesis are fulfilled, we identify some research opportunities extending from the presented work while reflecting on what has been discussed in the thesis.

More specifically, for IMDD systems, we show in chapter 3 that shaped signals can improve the system throughput since an optimized trade-off can be achieved between the system bandwidth and SNR. It is known that in long-haul DCO systems, shaped signals have an ultimate shaping gain of 1.53 dB due to the use of EDFAs such that the system is power-limited. However, it is unclear whether shaped signals can have a certain level of shaping gain in amplifier-less IMDD systems over a short reach for the intra-data center connections. These amplifier-less IMDD systems cannot be oversimplified as peak power-constrained systems since a) the driving signal could be much lower than the V_{π}, e.g. in the case of SiP modulators and b) the driving signal is often clipped before digital-to-analog conversion due to a high CSPR caused by some of the transmitter DSP block including pre-emphasis and near-Nyquist pulse shape. Thus to have a sensible discussion of this issue, assumptions need to be made to define the field of discussion and experiments should be carried out to corroborate an analysis with insightful results. Moreover, it is also unknown what is the optimal input distribution of such systems and what are appropriate distribution matching techniques to realize these optimal distributions. These newly developed techniques should be compared against benchmark tools to assess their performance.

For SC-SSB-DD systems, we show two approaches to generate wideband SC-SSB signals for large capacity systems beyond 40 km. While testing proof-of-concept systems based on the proposed approaches, we found that the modulator nonlinearity is the major performance-limiting issue that needs to be handled. We are interested in finding a nonlinear pre-compensation equalizer that can effectively invert the nonlinear response of the modulator while also being realizable using one DAC channel for cost-effectiveness.

It seems that an analytical form of such an equalizer is difficult to build and it looks more prospective to resolve this problem using numerical tools such as machine learning. We anticipate the nonlinear equalizer to further improve the throughput of amplifier-less SC-SSB-DD systems over 40 km of reach, which have more potential for short reach connections of the kind such as data center interconnects and mobile fronthaul communications. As for the polarization-division multiplexing scheme, it is interesting to think of a different signal generation subsystem apart from what is used in the demonstration and the all-digital generation scheme. Though the latter scheme is simple in terms of the system hardware, the generation of the side carriers degrades the signal SNR and thus reduces the achievable throughput.

In chapter 5, we discuss the ASCDD system in the entire chapter. Despite the high ESE in a single polarization compared to SC-SSB-DD systems, there is a lack of a straightforward approach to realize dual-pol ASCDD systems. We presented in chapter 5 a potential way to achieve polarization-division multiplexing. However, a feedback control circuit is required to keep monitoring the intensity difference between the PDs, which increases the complexity of the system. Another potential method is to use a pair of orthogonal carriers near the zero frequency having a small frequency gap between the carriers such that high ESE is retained. This method comes with the difficulty to generate such carriers. There could be other practical approaches to realize dual-pol ASCDD systems which can double the throughput of the ASCDD system per wavelength in order to meet the ever-growing bandwidth demand. Moreover, the proposed ASCDD scheme could be implemented on an integrated photonic circuit. For instance, the MZI-ASCDD receiver can be realized by concatenating a Y-branch, a spiral waveguide, a multimode coupler, and two photodiodes. When combined with an SSB SiP modulator, the entire system can be built based on the silicon-on-insulator platform, which could be a low-cost solution for short-reach data center connections by harnessing the established CMOS process.

Bibliography

[1] J. Hecht, *City of light: the story of fiber optics*. Oxford University Press on Demand, 2004.

[2] R. Mears, L. Reekie, I. Jauncey, and D. Payne, "Low-noise erbium-doped fibre amplifier at 1.54 pm," *Electronics Letters,* vol. 23, no. 19, pp. 1026-1028, 1987.

[3] B. Jopson and A. Gnauck, "Dispersion compensation for optical fiber systems," *IEEE Communications Magazine,* vol. 33, no. 6, pp. 96-102, 1995.

[4] S. Saito, T. Imai, T. Sugie, N. Ohkawa, Y. Ichihashi, and T. Ito, "An over 2,200 km coherent transmission experiment at 2.5 Gbit/s using erbium-doped-fiber amplifiers," in *Optical Fiber Communication*, San Francisco, California, 1990, p. PD2: Optical Society of America.

[5] H. Taga *et al.*, "10Gbit/s, 9,000km IM-DD Transmission Experiments Using 274 Er-doped Fiber Amplifier Repeaters," in *Conference on Optical Fiber Communication/International Conference on Integrated Optics and Optical Fiber Communication*, San Jose, California, 1993, vol. 4, p. PD1: Optical Society of America.

[6] E. M. Ip and J. M. Kahn, "Fiber impairment compensation using coherent detection and digital signal processing," *Journal of Lightwave Technology,* vol. 28, no. 4, pp. 502-519, 2009.

[7] K. Roberts, D. Beckett, D. Boertjes, J. Berthold, and C. Laperle, "100G and beyond with digital coherent signal processing," *IEEE Communications Magazine,* vol. 48, no. 7, pp. 62-69, 2010.

[8] S. J. Savory, "Coherent Detection - Why is it back?," in *LEOS 2007 - IEEE Lasers and Electro-Optics Society Annual Meeting Conference Proceedings*, 2007, pp. 212-213.

[9] F. Buchali *et al.*, "128 GSa/s SiGe DAC Implementation Enabling 1.52 Tb/s Single Carrier Transmission," *Journal of Lightwave Technology,* vol. 39, no. 3, pp. 763-770, 2021.

[10] H. Sun, K.-T. Wu, and K. Roberts, "Real-time measurements of a 40 Gb/s coherent system," *Optics Express,* vol. 16, no. 2, pp. 873-879, 2008/01/21 2008.

[11] V. Bajaj, F. Buchali, M. Chagnon, S. Wahls, and V. Aref, "Single-channel 1.61 Tb/s Optical Coherent Transmission Enabled by Neural Network-Based Digital Pre-Distortion," in *2020 European Conference on Optical Communications (ECOC)*, 2020, pp. 1-4.

[12] K. Schuh *et al.*, "Single Carrier 1.2 Tbit/s Transmission over 300 km with PM-64 QAM at 100 GBaud," in *Optical Fiber Communication Conference Postdeadline Papers*, Los Angeles, California, 2017, p. Th5B.5: Optical Society of America.

[13] X. Chen *et al.*, "Generation and Intradyne Detection of Single-Wavelength 1.61-Tb/s Using an All-Electronic Digital Band Interleaved Transmitter," in *Optical Fiber Communication Conference Postdeadline Papers*, San Diego, California, 2018, p. Th4C.1: Optical Society of America.

[14] G. Raybon *et al.*, "180-GBaud All-ETDM Single-Carrier Polarization Multiplexed QPSK Transmission over 4480 km," in *Optical Fiber Communication Conference Postdeadline Papers*, San Diego, California, 2018, p. Th4C.3: Optical Society of America.

[15] M. Sabelhaus, "100G Metro transformation," ed: Lightwave, 2014.

[16] "Cisco Global Cloud Index," 2016-2021.

[17] X. Chen *et al.*, "Single-Wavelength and Single-Photodiode 700 Gb/s Entropy-Loaded PS-256-QAM and 200-GBaud PS-PAM-16 Transmission over 10-km SMF," in *2020 European Conference on Optical Communications (ECOC)*, 2020, pp. 1-4.

[18] M. Morsy-Osman *et al.*, "DSP-free ‘coherent-lite’ transceiver for next generation single wavelength optical intra-datacenter interconnects," *Optics Express,* vol. 26, no. 7, pp. 8890-8903, 2018/04/02 2018.

[19] P. Schulte and G. Böcherer, "Constant Composition Distribution Matching," *IEEE Transactions on Information Theory,* vol. 62, no. 1, pp. 430-434, 2016.

[20] S. T. Le and K. Schuh, "465 Gbps Single Side Band Direct Detection Transmission over 40 km of SSMF using a Single-ended Photodiode," in *2021 Optical Fiber Communications Conference and Exhibition (OFC)*, 2021, pp. 1-3: IEEE.

[21] Q. Zhang *et al.*, "Single-lane 180 Gb/s SSB-duobinary-PAM-4 signal transmission over 13 km SSMF," in *Optical Fiber Communication Conference*, 2017, p. Tu2D. 2: Optical Society of America.

[22] J. Lee, S. Kim, Y. Kim, Y. Oh, S. Hwang, and J. Jeong, "Optically Preamplified Receiver Performance Due to VSB Filtering for 40-Gb/s Optical SignalsModulated With Various Formats," *Journal of lightwave technology,* vol. 21, no. 2, p. 521, 2003.

[23] W. Shieh, C. Sun, and H. Ji, "Carrier-assisted differential detection," *Light: Science & Applications,* vol. 9, no. 1, pp. 1-9, 2020.

[24] M. Jacques *et al.*, "200 Gbit/s net rate transmission over 2 km with a silicon photonic segmented MZM," in *45th European Conference on Optical Communication (ECOC 2019)*, 2019, pp. 1-4.

[25] M. S. Alam *et al.*, "Net 220 Gbps/ IM/DD Transmission in O-band and C-band with silicon photonic Traveling-Wave MZM," *Journal of Lightwave Technology,* pp. 1-1, 2021.

[26] Y. Zhu *et al.*, "Toward Single Lane 200G Optical Interconnects With Silicon Photonic Modulator," *Journal of Lightwave Technology,* vol. 38, no. 1, pp. 67-74, 2020.

[27] Y. Zhang *et al.*, "200 Gbit/s Optical PAM4 Modulation Based on Silicon Microring Modulator," in *2020 European Conference on Optical Communications (ECOC)*, 2020, pp. 1-4.

[28] N.-P. Diamantopoulos *et al.*, ">100-GHz Bandwidth Directly-Modulated Lasers and Adaptive Entropy Loading for Energy-Efficient >300-Gbps/ λ IM/DD Systems," *Journal of Lightwave Technology,* vol. 39, no. 3, pp. 771-778, 2021/02/01 2021.

[29] D. Che, Y. Matsui, X. Chen, R. Schatz, and P. Iannone, "400-Gb/s direct modulation using a DFB+R laser," *Optics Letters,* vol. 45, no. 12, pp. 3337-3339, 2020/06/15 2020.

[30] D. Che *et al.*, "200-Gb/s Direct Modulation of a 50-GHz Class Laser With Advanced Digital Modulations," *Journal of Lightwave Technology,* vol. 39, no. 3, pp. 845-852, 2021/02/01 2021.

[31] Y. Matsui, R. Schatz, D. Che, F. Khan, M. Kwakernaak, and T. Sudo, "Low-chirp isolator-free 65-GHz-bandwidth directly modulated lasers," *Nature Photonics,* vol. 15, no. 1, pp. 59-63, 2021/01/01 2021.

[32] J. Wang and K. Petermann, "Small signal analysis for dispersive optical fiber communication systems," *Journal of Lightwave Technology,* vol. 10, no. 1, pp. 96-100, 1992.

[33] R. Srinivasan and J. Cartledge, "On using fiber transfer functions to characterize laser chirp and fiber dispersion," *IEEE Photonics Technology Letters,* vol. 7, no. 11, pp. 1327-1329, 1995.

[34] L. Bjerkan, A. Royset, L. Hafskjaer, and D. Myhre, "Measurement of laser parameters for simulation of high-speed fiberoptic systems," *Journal of Lightwave Technology,* vol. 14, no. 5, pp. 839-850, 1996.

[35] C. Laperle and M. O’Sullivan, "Advances in High-Speed DACs, ADCs, and DSP for Optical Coherent Transceivers," *Journal of Lightwave Technology,* vol. 32, no. 4, pp. 629-643, 2014/02/15 2014.

[36] X. Chen, S. Chandrasekhar, S. Randel, W. Gu, and P. Winzer, "Experimental quantification of implementation penalties from limited ADC resolution for Nyquist shaped higher-order QAM," in *Optical Fiber Communication Conference*, 2016, p. W4A. 3: Optical Society of America.

[37] D. Rafique, A. Napoli, S. Calabro, and B. Spinnler, "Digital preemphasis in optical communication systems: On the DAC requirements for terabit transmission applications," *Journal of Lightwave Technology,* vol. 32, no. 19, pp. 3247-3256, 2014.

[38] S. L. I. Olsson, J. Cho, S. Chandrasekhar, X. Chen, P. J. Winzer, and S. Makovejs, "Probabilistically shaped PDM 4096-QAM transmission over up to 200 km of fiber using standard intradyne detection," *Optics Express,* vol. 26, no. 4, pp. 4522-4530, 2018/02/19 2018.

[39] S. Okamoto, M. Terayama, M. Yoshida, K. Kasai, T. Hirooka, and M. Nakazawa, "Experimental and Numerical Comparison of Probabilistically-Shaped 4096 QAM and Uniformly-Shaped 1024 QAM in All-Raman Amplified 160 km Transmission," in *Optical Fiber Communication Conference*, San Diego, California, 2018, p. M3C.5: Optical Society of America.

[40] P. Schulte and G. Böcherer, "Constant composition distribution matching," *IEEE Transactions on Information Theory,* vol. 62, no. 1, pp. 430-434, 2015.

[41] J. Cho and P. J. Winzer, "Probabilistic constellation shaping for optical fiber communications," *Journal of Lightwave Technology,* vol. 37, no. 6, pp. 1590-1607, 2019.

[42] K. Zhong *et al.*, "Experimental demonstration of 500Gbit/s short reach transmission employing PAM4 signal and direct detection with 25Gbps device," in *Optical Fiber Communication Conference*, 2015, p. Th3A. 3: Optical Society of America.

[43] T. M. Hoang *et al.*, "Single wavelength 480 Gb/s direct detection over 80km SSMF enabled by Stokes vector Kramers Kronig transceiver," *Optics Express,* vol. 25, no. 26, pp. 33534-33542, 2017.

[44] S. T. Le, K. Schuh, R. Dischler, F. Buchali, L. Schmalen, and H. Buelow, "5× 510 Gbps single-polarization direct-detection WDM transmission over 80 km of SSMF," in *Optical Fiber Communication Conference*, 2019, p. Tu2B. 1: Optical Society of America.

[45] A. Mecozzi, C. Antonelli, and M. Shtaif, "Kramers – Kronig coherent receiver," *Optica,* vol. 3, no. 11, pp. 1220-1227, 2016.

[46] X. Chen *et al.*, "Kramers – Kronig receivers for 100-km datacenter interconnects," *Journal of Lightwave Technology,* vol. 36, no. 1, pp. 79-89, 2018.

[47] C. Füllner *et al.*, "Complexity analysis of the Kramers – Kronig receiver," *Journal of Lightwave Technology,* vol. 37, no. 17, pp. 4295-4307, 2019.

[48] T. Bo and H. Kim, "Toward practical Kramers-Kronig receiver: resampling, performance, and implementation," *Journal of Lightwave Technology,* vol. 37, no. 2, pp. 461-469, 2018.

[49] "<DuobinaryModulationForOpticalSystems.pdf>."

[50] Charlene, "800G Is Coming: Set Pace to More Higher Speed Applications," ed, 2020.

[51] X. Zhou, R. Urata, and H. Liu, "Beyond 1 Tb/s Intra-Data Center Interconnect Technology: IM-DD OR Coherent?," *Journal of Lightwave Technology,* vol. 38, no. 2, pp. 475-484, 2020/01/15 2020.

[52] H. Mardoyan *et al.*, "84-, 100-, and 107-GBd PAM-4 Intensity-Modulation Direct-Detection Transceiver for Datacenter Interconnects," *Journal of Lightwave Technology,* vol. 35, no. 6, pp. 1253-1259, 2017.

[53] T. Wiegart, F. Da Ros, M. P. Yankov, F. Steiner, S. Gaiarin, and R. D. Wesel, "Probabilistically Shaped 4-PAM for Short-Reach IM/DD Links With a Peak Power Constraint," *Journal of Lightwave Technology,* vol. 39, no. 2, pp. 400-405, 2021/01/15 2021.

[54] D. Che, "Does Probabilistic Constellation Shaping Benefit IM-DD Systems without Optical Amplifiers?," 2021.

[55] T. A. Eriksson, M. Chagnon, F. Buchali, K. Schuh, S. ten Brink, and L. Schmalen, "56 Gbaud probabilistically shaped PAM8 for data center interconnects," in *2017 European Conference on Optical Communication (ECOC)*, 2017, pp. 1-3: IEEE.

[56] Z. He, T. Bo, and H. Kim, "Probabilistically shaped coded modulation for IM/DD system," *Optics Express,* vol. 27, no. 9, pp. 12126-12136, 2019/04/29 2019.

[57] X. Chen, S. Chandrasekhar, J. Cho, and P. Winzer, "Single-Wavelength and Single-Photodiode Entropy-Loaded 554-Gb/s Transmission over 22-km SMF," in *Optical*

Fiber Communication Conference Postdeadline Papers 2019, San Diego, California, 2019, p. Th4B.5: Optical Society of America.
[58] G. Böcherer, F. Steiner, and P. Schulte, "Bandwidth Efficient and Rate-Matched Low-Density Parity-Check Coded Modulation," *IEEE Transactions on Communications,* vol. 63, no. 12, pp. 4651-4665, 2015.
[59] X. Li, Z. Xing, M. S. Alam, M. Jacques, P.-C. Koh, and D. V. Plant, "Cost-minimizing distribution matching supporting net 800 Gbit/s PS-PAM transmission over 2 km using a 4- λ EML TOSA," *Optics Letters,* vol. 45, no. 17, pp. 4718-4721, 2020/09/01 2020.
[60] G. D. Forney, L. Brown, M. V. Eyuboglu, and J. L. Moran, "The V.34 high speed modem standard," *IEEE Communications Magazine,* vol. 34, no. 12, pp. 28-33, 1996.
[61] P. Schulte and F. Steiner, "Divergence-Optimal Fixed-to-Fixed Length Distribution Matching With Shell Mapping," *IEEE Wireless Communications Letters,* vol. 8, no. 2, pp. 620-623, 2019.
[62] F. Steiner *et al.*, "Experimental Verification of Rate Flexibility and Probabilistic Shaping by 4D Signaling," in *Optical Fiber Communication Conference*, San Diego, California, 2018, p. M4E.3: Optical Society of America.
[63] L. M. Zhang and F. R. Kschischang, "Staircase Codes With 6% to 33% Overhead," *Journal of Lightwave Technology,* vol. 32, no. 10, pp. 1999-2002, 2014/05/15 2014.
[64] T. Cover, "Enumerative source encoding," *IEEE Transactions on Information Theory,* vol. 19, no. 1, pp. 73-77, 1973.
[65] C. Pan and F. R. Kschischang, "Probabilistic 16-QAM Shaping in WDM Systems," *Journal of Lightwave Technology,* vol. 34, no. 18, pp. 4285-4292, 2016.
[66] M. P. Yankov, D. Zibar, K. J. Larsen, L. P. B. Christensen, and S. Forchhammer, "Constellation Shaping for Fiber-Optic Channels With QAM and High Spectral Efficiency," *IEEE Photonics Technology Letters,* vol. 26, no. 23, pp. 2407-2410, 2014.
[67] E. Sillekens *et al.*, "A Simple Nonlinearity-Tailored Probabilistic Shaping Distribution for Square QAM," in *2018 Optical Fiber Communications Conference and Exposition (OFC)*, 2018, pp. 1-3.
[68] X. Li, Z. Xing, M. S. Alam, M. Jacques, S. Lessard, and D. V. Plant, "NN-based PCS distribution optimization for practical channels," in *2020 European Conference on Optical Communications (ECOC)*, 2020, pp. 1-4.
[69] A. Alvarado, E. Agrell, D. Lavery, R. Maher, and P. Bayvel, "Replacing the Soft-Decision FEC Limit Paradigm in the Design of Optical Communication Systems," *Journal of Lightwave Technology,* vol. 33, no. 20, pp. 4338-4352, 2015.
[70] G. Forecast, "Cisco visual networking index: global mobile data traffic forecast update, 2017 – 2022," *Update,* vol. 2017, p. 2022, 2019.
[71] L. Zhang *et al.*, "Beyond 100-Gb/s Transmission Over 80-km SMF Using Direct-Detection SSB-DMT at C-Band," *Journal of Lightwave Technology,* vol. 34, no. 2, pp. 723-729, 2016.

[72] S. T. Le, V. Aref, K. Schuh, and H. N. Tan, "30 Gbaud 128 QAM SSB direct detection transmission over 80 km with clipped iterative SSBI cancellation," in *2020 Optical Fiber Communications Conference and Exhibition (OFC)*, 2020, pp. 1-3: IEEE.

[73] H.-Y. Chen, N. Kaneda, J. Lee, J. Chen, and Y.-K. Chen, "Optical filter requirements in an EML-based single-sideband PAM4 intensity-modulation and direct-detection transmission system," *Optics Express,* vol. 25, no. 6, pp. 5852-5860, 2017/03/20 2017.

[74] A. Mecozzi, C. Antonelli, and M. Shtaif, "Kramers–Kronig receivers," *Advances in Optics and Photonics,* vol. 11, no. 3, pp. 480-517, 2019/09/30 2019.

[75] X. Li, M. Zhu, Z. Xing, M. O’Sullivan, and D. V. Plant, "Asymmetric direct detection of twin-SSB signals," *Optics letters,* vol. 45, no. 4, pp. 844-847, 2020.

[76] M. Sieben, J. Conradi, and D. E. Dodds, "Optical single sideband transmission at 10 Gb/s using only electrical dispersion compensation," *Journal of Lightwave Technology,* vol. 17, no. 10, pp. 1742-1749, 1999.

[77] B. Davies and J. Conradi, "Hybrid modulator structures for subcarrier and harmonic subcarrier optical single sideband," *IEEE Photonics Technology Letters,* vol. 10, no. 4, pp. 600-602, 1998.

[78] X. Li, Z. Xing, M. S. Alam, M. E. Mousa-Pasandi, M. O'Sullivan, and D. V. Plant, "Demonstration of C-Band Amplifier-Free 100 Gb/s/λ Direct-Detection Links Beyond 40-km SMF Using a High-Power SSB Transmitter," *Journal of Lightwave Technology,* vol. 38, no. 22, pp. 6170-6177, 2020.

[79] D. Che and W. Shieh, "Approaching the Capacity of Colored-SNR Optical Channels by Multicarrier Entropy Loading," *Journal of Lightwave Technology,* vol. 36, no. 1, pp. 68-78, 2018.

[80] A. Lorences-Riesgo *et al.*, "200 G Outdoor Free-Space-Optics Link Using a Single-Photodiode Receiver," *Journal of Lightwave Technology,* vol. 38, no. 2, pp. 394-400, 2020.

[81] T. Bo and H. Kim, "Recovery of DC Component in Kramers-Kronig Receiver Utilizing AC-Coupled Photo-Detector," in *Optical Fiber Communication Conference (OFC) 2020*, San Diego, California, 2020, p. M3J.1: Optical Society of America.

[82] X. Chen, S. Chandrasekhar, S. Olsson, A. Adamiecki, and P. Winzer, "Impact of O/E Front-End Frequency Response on Kramers-Kronig Receivers and its Compensation," in *2018 European Conference on Optical Communication (ECOC)*, 2018, pp. 1-3.

[83] Y. Zhu, L. Li, X. Miao, and W. Hu, "Time Skew-based Filter-free VSB Nyquist PAM-4/6 Generation and 80km SSMF Transmission with Direct Detection," in *2020 European Conference on Optical Communications (ECOC)*, 2020, pp. 1-5: IEEE.

[84] M. S. Alam, X. Li, Z. Xing, M. E. Mousa-Pasandi, M. O’Sullivan, and D. V. Plant, "C-band 4×200 Gbit/s transmission over 40 km of SSMF with an RF delay-assisted WDM-SSB transmitter," in *Optical Fiber Communication Conference (OFC) 2021*, Washington, DC, 2021, p. W6A.50: Optical Society of America.

[85] Q. Zhang, N. Stojanovic, C. Xie, C. Prodaniuc, and P. Laskowski, "Transmission of single lane 128 Gbit/s PAM-4 signals over an 80 km SSMF link, enabled by DDMZM aided dispersion pre-compensation," *Optics express,* vol. 24, no. 21, pp. 24580-24591, 2016.

[86] Z. Xing *et al.*, "100 Gb/s PAM4 transmission system for datacenter interconnects using a SiP ME-MZM based DAC-less transmitter and a VSB self-coherent receiver," *Optics Express,* vol. 26, no. 18, p. 23969, 2018.

[87] Z. Li *et al.*, "SSBI Mitigation and the Kramers – Kronig Scheme in Single-Sideband Direct-Detection Transmission With Receiver-Based Electronic Dispersion Compensation," *Journal of Lightwave Technology,* vol. 35, no. 10, pp. 1887-1893, 2017.

[88] Z. Xing *et al.*, "100 Gb/s PAM4 transmission system for datacenter interconnects using a SiP ME-MZM based DAC-less transmitter and a VSB self-coherent receiver," *Optics express,* vol. 26, no. 18, pp. 23969-23979, 2018.

[89] C. Antonelli, A. Mecozzi, M. Shtaif, X. Chen, S. Chandrasekhar, and P. J. Winzer, "Polarization multiplexing with the Kramers-Kronig receiver," *Journal of Lightwave Technology,* vol. 35, no. 24, pp. 5418-5424, 2017.

[90] D. Che, C. Sun, and W. Shieh, "Single-Channel 480-Gb/s Direct Detection of POL-MUX IQ Signal Using Single-Sideband Stokes Vector Receiver," in *Optical Fiber Communication Conference (OFC)*, San Diego, California, 2018, p. Tu2C.7: Optical Society of America.

[91] T. M. Hoang *et al.*, "Single wavelength 480 Gb/s direct detection over 80km SSMF enabled by Stokes vector Kramers Kronig transceiver," *Optics Express,* vol. 25, no. 26, p. 33534, 2017.

[92] D. Che, C. Sun, and W. Shieh, "Maximizing the spectral efficiency of Stokes vector receiver with optical field recovery," *Optics Express,* vol. 26, no. 22, p. 28976, 2018.

[93] T. M. Hoang *et al.*, "Single wavelength 480 Gb/s direct detection over 80km SSMF enabled by Stokes vector Kramers Kronig transceiver," *Optics Express,* vol. 25, no. 26, pp. 33534-33542, 2017/12/25 2017.

[94] D. Che, C. Sun, and W. Shieh, "Maximizing the spectral efficiency of Stokes vector receiver with optical field recovery," *Optics Express,* vol. 26, no. 22, pp. 28976-28981, 2018/10/29 2018.

[95] Y. Zhu, M. Jiang, and F. Zhang, "Direct detection of polarization multiplexed single sideband signals with orthogonal offset carriers," *Optics Express,* vol. 26, no. 12, pp. 15887-15898, 2018/06/11 2018.

[96] X. Li *et al.*, "Asymmetric direct detection of orthogonal offset carriers assisted polarization multiplexed single-sideband signals," *Optics Express,* vol. 28, no. 3, pp. 3226-3236, 2020/02/03 2020.

[97] D. Dai, J. Bauters, and J. E. Bowers, "Passive technologies for future large-scale photonic integrated circuits on silicon: polarization handling, light non-reciprocity and loss reduction," vol. 1, no. 3, p. e1, 2012.

[98] H. Fukuda, K. Yamada, T. Tsuchizawa, T. Watanabe, H. Shinojima, and S.-i. Itabashi, "Silicon photonic circuit with polarization diversity," *Optics express,* vol. 16, no. 7, pp. 4872-4880, 2008.

[99] F. Y. Gardes, D. J. Thomson, N. G. Emerson, and G. T. Reed, "40 Gb/s silicon photonics modulator for TE and TM polarisations," *Optics Express,* vol. 19, no. 12, pp. 11804-11814, 2011/06/06 2011.

[100] D. Dai, J. Bauters, and J. E. Bowers, "Passive technologies for future large-scale photonic integrated circuits on silicon: polarization handling, light non-reciprocity and loss reduction," *Light: Science & Applications,* vol. 1, no. 3, pp. e1-e1, 2012/03/01 2012.

[101] S. T. Le, K. Schuh, M. Chagnon, F. Buchali, and H. Buelow, "1.6Tbps WDM Direct Detection Transmission with Virtual-Carrier over 1200km," in *Optical Fiber Communication Conference*, San Diego, California, 2018, p. Tu2D.5: Optical Society of America.

[102] S. T. Le *et al.*, "1.72-Tb/s virtual-carrier-assisted direct-detection transmission over 200 km," *Journal of Lightwave Technology,* vol. 36, no. 6, pp. 1347-1353, 2018.

[103] M. Selmi, Y. Jaouen, and P. Ciblat, "Accurate digital frequency offset estimator for coherent PolMux QAM transmission systems," in *2009 35th European Conference on Optical Communication*, 2009, pp. 1-2.

[104] C. Laperle, B. Villeneuve, Z. Zhang, D. McGhan, H. Sun, and M. O. Sullivan, "WDM Performance and PMD Tolerance of a Coherent 40-Gbit/s Dual-Polarization QPSK Transceiver," *Journal of Lightwave Technology,* vol. 26, no. 1, pp. 168-175, 2008.

[105] K. Zhong, X. Zhou, J. Huo, C. Yu, C. Lu, and A. P. T. Lau, "Digital signal processing for short-reach optical communications: A review of current technologies and future trends," *Journal of Lightwave Technology,* vol. 36, no. 2, pp. 377-400, 2018.

[106] F. Buchali *et al.*, "1.52 Tb/s single carrier transmission supported by a 128 GSa/s SiGe DAC," in *Optical Fiber Communication Conference*, 2020, p. Th4C. 2: Optical Society of America.

[107] S. J. Savory, G. Gavioli, R. I. Killey, and P. Bayvel, "Electronic compensation of chromatic dispersion using a digital coherent receiver," *Optics express,* vol. 15, no. 5, pp. 2120-2126, 2007.

[108] M. Schuster *et al.*, "Spectrally efficient compatible single-sideband modulation for OFDM transmission with direct detection," *IEEE Photonics Technology Letters,* vol. 20, no. 9, pp. 670-672, 2008.

[109] P. J. Winzer and R.-J. Essiambre, "Advanced optical modulation formats," *Optical Fiber Telecommunications VB,* pp. 23-93, 2008.

[110] W.-R. Peng, B. Zhang, K.-M. Feng, X. Wu, A. E. Willner, and S. Chi, "Spectrally efficient direct-detected OFDM transmission incorporating a tunable frequency gap and an iterative detection techniques," *Journal of Lightwave Technology,* vol. 27, no. 24, pp. 5723-5735, 2009.

[111] B. J. Schmidt, A. J. Lowery, and J. Armstrong, "Experimental demonstrations of electronic dispersion compensation for long-haul transmission using direct-

detection optical OFDM," *Journal of Lightwave Technology,* vol. 26, no. 1, pp. 196-203, 2008.

[112] X. Chen *et al.*, "218-Gb/s single-wavelength, single-polarization, single-photodiode transmission over 125-km of standard singlemode fiber using Kramers-Kronig detection," in *Optical Fiber Communication Conference*, 2017, p. Th5B. 6: Optical Society of America.

[113] D. Che, C. Sun, and W. Shieh, "Optical field recovery in Stokes space," *Journal of Lightwave Technology,* vol. 37, no. 2, pp. 451-460, 2018.

[114] D. Che, Q. Hu, and W. Shieh, "Linearization of direct detection optical channels using self-coherent subsystems," *Journal of Lightwave Technology,* vol. 34, no. 2, pp. 516-524, 2016.

[115] X. Liu, S. Chandrasekhar, and A. Leven, "Digital self-coherent detection," *Optics Express,* vol. 16, no. 2, pp. 792-803, 2008.

[116] S. Randel, D. Pilori, S. Chandrasekhar, G. Raybon, and P. Winzer, "100-Gb/s discrete-multitone transmission over 80-km SSMF using single-sideband modulation with novel interference-cancellation scheme," in *2015 European Conference on Optical Communication (ECOC)*, 2015, pp. 1-3: IEEE.

[117] A. Mecozzi, C. Antonelli, and M. Shtaif, "Kramers – kronig receivers," *Advances in Optics and Photonics,* vol. 11, no. 3, pp. 480-517, 2019.

[118] T. Bo and H. Kim, "Kramers-Kronig receiver operable without digital upsampling," *Optics express,* vol. 26, no. 11, pp. 13810-13818, 2018.

[119] L. Zhang, T. Zuo, Q. Zhang, J. Zhou, E. Zhou, and G. N. Liu, "150-Gb/s DMT over 80-km SMF transmission based on spectrally efficient SSBI cancellation using guard-band twin-SSB technique," in *ECOC 2016; 42nd European Conference on Optical Communication*, 2016, pp. 1-3: VDE.

[120] C. Sun, T. Ji, H. Ji, Z. Xu, and W. Shieh, "Experimental demonstration of complex-valued DSB signal field recovery via direct detection," *IEEE Photonics Technology Letters,* vol. 32, no. 10, pp. 585-588, 2020.

[121] X. Chen, D. Che, A. Li, J. He, and W. Shieh, "Signal-carrier interleaved optical OFDM for direct detection optical communication," *Optics express,* vol. 21, no. 26, pp. 32501-32507, 2013.

[122] X. Li, M. O'Sullivan, Z. Xing, M. S. Alam, M. E. Mousa-Pasandi, and D. V. Plant, "Asymmetric self-coherent detection," *Optics Express,* vol. 29, no. 16, pp. 25412-25427, 2021/08/02 2021.

[123] A. Nespola *et al.*, "Proof of concept of polarization-multiplexed PAM using a compact si-ph device," *IEEE Photonics Technology Letters,* vol. 31, no. 1, pp. 62-65, 2018.

[124] T. Gui, X. Wang, M. Tang, Y. Yu, Y. Lu, and L. Li, "Real-Time Demonstration of Homodyne Coherent Bidirectional Transmission for Next-Generation Data Center Interconnects," *Journal of Lightwave Technology,* vol. 39, no. 4, pp. 1231-1238, 2021.

[125] H. Chen, N. K. Fontaine, J. M. Gene, R. Ryf, D. T. Neilson, and G. Raybon, "Dual polarization full-field signal waveform reconstruction using intensity only measurements for coherent communications," *Journal of Lightwave Technology,* vol. 38, no. 9, pp. 2587-2597, 2020.

[126] M. Matsumoto, "Optical Signal Phase Reconstruction Based on Temporal Transport-of-Intensity Equation," *Journal of Lightwave Technology,* vol. 38, no. 17, pp. 4722-4729, 2020.

[127] Y. Zhang, M. O' Sullivan, and R. Hui, "Theoretical and experimental investigation of compatible SSB modulation for single channel long-distance optical OFDM transmission," *Optics express,* vol. 18, no. 16, pp. 16751-16764, 2010.

[128] D. Tan, K. Ikeda, R. Saperstein, B. Slutsky, and Y. Fainman, "Chip-scale dispersion engineering using chirped vertical gratings," *Optics letters,* vol. 33, no. 24, pp. 3013-3015, 2008.

[129] Y. Painchaud, M. Lapointe, F. Trépanier, R. L. Lachance, C. Paquet, and M. Guy, "Recent progress on FBG-based tunable dispersion compensators for 40 Gb/s applications," in *Optical Fiber Communication Conference*, 2007, p. OThP3: Optical Society of America.

[130] Y. Painchaud, A. Mailloux, H. Chotard, É. Pelletier, and M. Guy, "Multi-channel fiber Bragg gratings for dispersion and slope compensation," in *Optical Fiber Communication Conference and Exhibit*, 2002, pp. 581-582: IEEE.